Response of the landscape in the Swiss Alps to the late glacial to Holocene climate transition

Von der Naturwissenschaftlichen Fakultät der
Gottfried Wilhelm Leibniz Universität Hannover
zur Erlangung des Grades eines
DOKTORS DER NATURWISSENSCHAFTEN
Dr. rer. nat.

genehmigte Dissertation
von
M. Sc. Kevin Patrick Norton
geboren am 13.03.1974 in Springfield, Ohio
2008

Referent: Prof. Dr. Friedhelm von Blanckenburg
               (Leibniz Universität Hannover)

Korreferent: Prof. Dr. Fritz Schlunegger
               (Universität Bern)

Tag der Promotion: 14.08.08

Erklärung zur Dissertation

Hierdurch erkläre ich, dass die Dissertation selbständig verfasst und alle benutzten Hilfsmittel sowie evtl. zur Hilfeleistung herangezogene Institutionen vollständig angegeben habe. Die Dissertation wurde nicht schon als Diplomarbeit oder ähnliche Prüfungsarbeit verwendet.

Hannover, den 12.06.2008

Kevin Patrick Norton

"Climb the mountains and get their good tidings"

-John Muir

CONTENTS

ABSTRACT

Mountains grow and they wear away. How these two processes, rock uplift and denudation, interact has been a major topic in Earth Science research for decades. Rock uplift, through lowering of fluvial baselevel and increasing relief, should enhance surface denudation, while denudation in turn through isostatic compensation from mass loss, should lead to rock uplift. The concept of topographic steady-state, where rock uplift is matched by denudation raises some fundamental questions: does rock uplift drive erosion or vice versa? Over which temporal or spatial scales are these relationships valid? Through which mechanisms does a system in steady-state react to perturbations and over what timescales will these transient responses take place?

These questions can be answered using basin and hillslope scale analyses of chemical and physical process rates in transient landscapes. New geochemical rate meters (cosmogenic ^{10}Be-derived basin-averaged and amalgamated soil denudation rates, soil chemical depletion fractions) and high resolution digital elevation data are used to address questions of the rate and nature of transient response in the Swiss Alps.

The dissertation can be divided into 4 major themes. First, I quantify the large errors that can be introduced by using coarse resolution elevation data for calculations of production of cosmogenic nuclides in minerals at the Earth's surface by interaction with cosmic radiation. Knowledge of the fraction of cosmic rays which are obstructed by topography, and hence do not contribute to production of in situ cosmogenic nuclides in the basin, is critical for calculating denudation rates from ^{10}Be in quartz in river sediment. These calculations are usually made using digital elevation models, DEM, despite the well-known bias that occurs when measuring a topographic metric at varying DEM resolutions. I calculated basin-averaged topographic shielding factors of a wide array of landscapes in order to show that the basin shielding factor scales with increasing surface roughness and increasing grid size, pointing to the need for either high-resolution elevation data or a correction factor when calculating shielding for in situ-produced cosmogenic nuclide-derived denudation rate studies.

Next, I present [10]Be-derived denudation rate data to show that topographic transience is widespread in the Alps, and that response times from tectonic or climatic perturbations vary considerably, to the degree that some drainage basins in the Swiss Mittelland have completely returned to a quasi-equilibrium state, while hillslopes in the upper Rhone valley have not yet responded to post-glacial perturbations. In the Swiss Mittelland, high resolution LiDAR elevation data and in situ-produced cosmogenic [10]Be-derived basin-averaged denudation rates record late Pleistocene and Holocene landscape evolution. Response times in this setting are dependant on the magnitude of the post-Last Glacial Maximum, LGM, perturbation. A new quasi-equilibrium state has already been achieved in the Trub catchment after a small baselevel drop, while in the adjacent Fontanne, where base level fall was 4x larger, only 10% of the landscape has responded. Transient response in the Swiss Mittelland is also variable in time. The paleo-denudation rates during the early post-LGM, calculated from gravel terraces, are 4-5x faster than modern rates of $0.3 - 0.6$ mm y^{-1} and demonstrate transient knickzone migration and rapid stream incision.

The Rhone River is one of the largest fluvial systems in Europe. The uppermost valley, known as Goms, was under more than 1500 m of ice during the LGM, producing an overdeepened glacial valley with a bedrock knickpoint at the downstream end of the valley. The area is subject to some of the highest rates of rock uplift in the Swiss Alps, $0.7 - 1.3$ mm y^{-1}, but the knickpoint isolates the lateral valleys of the Goms from the baselevel lowering effects of rock uplift. Despite the lack of a baselevel link, the rate-weighted mean denudation rate for the Goms is similar to modern rock uplift rates, ~1.3 mm y^{-1}. Cosmogenic [10]Be-derived denudation rates from individual basins, ~0.6-2.1 mm y^{-1}, show that the relative contribution of slow hillslope creep, and fast stochastic mass wasting (debris flows and rock falls) determines the rate of basin erosion and that soil mantling is capable of slowing basin response to tectonic or climatic perturbations. In the same valleys, chemical weathering intensities decrease from ridge tops to hillslopes and with decreasing temperature, pointing to thermal-kinetic control of chemical weathering which amounts to ~10 to 50% of the total denudation. This control is in contrast to

the growing picture that chemical weathering is tightly correlated with physical erosion rates.

Finally, I show that the relatively large magnitude of post-LGM glacial advance can not be explained by temperature drops recorded by Alpine paleoclimate proxies alone, and show that glacio-isostatic rebound from the melting LGM ice cover can promote glacial readvance, independent of climate change.

The small-spatial scale approach to cosmogenic nuclide-derived denudation rates and mass loss-derived chemical weathering intensities presented here are capable of addressing heretofore unanswerable questions. Transience is common occurrence in the European Alps. Basins in the Central Alps are responding to perturbations through changes in the relative contribution of rapid and slow processes. Response times in a mountain range are extremely variable.

The methods presented here are well-suited to studying other mountain systems. The next questions are: how do the controls on erosion rates differ between isostatic and convergent orogens? And, are the mechanisms and rates of basin response the same in active orogens, where driving forces are tectonic as opposed to climatic?

Keywords: Cosmogenic Nuclides, European Alps, Surface Processes

Abstract

iv

ZUSAMMENFASSUNG

Gebirge wachsen und erodieren. Das Zusammenspiel der zwei Prozesse Gesteinshebung und Denudation ist seit Jahrzehnten ein Forschungsschwerpunkt der Geowissenschaften. Durch die Tieferlegung von Wasserläufen und der damit verbundenen Vergrößerung des Reliefs verursacht die Gesteinshebung eine Oberflächenabtragung. Diese Abtragung führt zu einem Massenverlust in fester und gelöster Form, welcher durch isostatische Kompensation erneut Gesteinshebung hervorruft. Das Konzept des topographischen Gleichgewichts, in dem Gesteinshebung mit Denudation einhergeht, wirft einige fundamentale Fragen auf: Führt die Hebung zur Erosion oder die Erosion zur Hebung? Welchen zeitlichen und räumlichen Dimensionen unterliegt dieser Zusammenhang? Welche Mechanismen stören ein stabiles Gleichgewicht und wie lang dauert es, bis sich ein erneutes Gleichgewicht einstellt?

Diese Fragen lassen sich beantworten, indem chemische und physikalische Prozessraten von Flusseinzugsgebieten und Hängen in gestörten Landschaften analysiert werden. Neue geochemische Methoden (Denudationsraten aus kosmogenem ^{10}Be aus einzugsgebietsweiten Flusssanden und Bodenproben sowie chemische Abreicherungsfaktoren aus Böden) und hoch aufgelöste digitale Höhendaten erlauben, die Geschwindigkeit und Form der Veränderungen der Schweizer Alpen zu entschlüsseln.

Diese Dissertation gliedert sich in vier Hauptthemen. Zuerst zeige ich, dass ungenaue Höhendaten bei der Berechnung von Produktionsraten der kosmogenen Nuklide in Mineralen der Erdoberfläche durch kosmische Strahlung zu erheblichen, eher quantifizierbaren Fehlern führen. Die topographische Abschirmung führt zur Verringerung der Produktionsraten der in situ gebildeten kosmogenen Nuklide. Für eine exakte Berechnung der Denudationsraten mittels ^{10}Be ist eine Kenntnis des Anteiles der abgeschirmten Strahlung ist unbedingt erforderlich. Üblicherweise werden hierfür digitale Höhenmodelle verwendet, die jedoch teilweise eine unzureichende Auflösung bieten. Ich berechne die topographischen Abschirmfaktoren aus unterschiedlichen Einzugsgebieten, um zu beweisen, dass sich die Abschirmfaktoren mit steigender Oberflächenrauhigkeit und gröberer Zellengröße des Höhenmodells zunehmen. Für Denudationsraten, die mit in-situ produzierten kosmogenen Nukliden berechnet wurden, werden demnach entweder gute, hoch aufgelöste Höhendaten benötigt, oder ein Korrekturfaktor muss angewendet werden.

Anschließend präsentiere ich ^{10}Be-basierte Denudationsdaten, um zu zeigen, dass topographische Ungleichgewichte in den Alpen weit verbreitet sind und dass die

Reaktionszeit auf tektonische und klimatische Störungen stark variiert. Bei einigen Einzugsgebieten des Schweizer Mittellandes wurde ein erneuter Gleichgewichtszustand erreicht, während Hänge im oberen Rhônetal auf postglaziale Störungen noch nicht reagiert haben. Hochauflösende LiDAR Höhendaten und Denudationsraten, die aus Konzentrationen des in-situ produzierten kosmogenen ^{10}Be-Nuklids berechnet wurden, bilden im Schweizer Mittelland die Spät-Pleistozäne und Holozäne Landschaftsentwicklung ab. Die Reaktionszeiten auf eine Störung des Gleichgewichts hängen von der Größe der Störung ab und variieren in den verschiedenen Zeiträumen. Dies zeigt sich im Trubtal, wo der Gleichgewichtszustand bereits nach einer kleinen Störung erreicht wurde, wohingegen sich im benachbarten Fontannetal nach einer viermal größeren Störung, auf die bisher nur 10% der Landschaft reagiert hat, noch kein Gleichgewicht eingestellt hat. Die Paläo-Denudationsraten nach der letzten Eiszeit, die an Kiesterrassen gemessen wurden, sind vier bis fünffach größer als rezente Denudationsraten (0.3 – 0.6 mm yr^{-1}) und zeigen, dass sich übersteilte Abschnitte in Flussprofilen (Knickpunkte) verlagern und sich dadurch Flüsse schnell einschneiden.

Das obere Rhônetal, auch Goms genannt, war während des Letzte Eiszeit (LGM) mit einer mehr als 1500 m mächtigen Eisdecke überlagert, was zu einer Übertiefung des Rhônetals und zur Ausbildung einer Festgesteinsstufe flussabwärts geführt hat. Obwohl dieses Gebiet die höchsten Hebungsraten in den Schweizer Alpen aufweist (0.7 – 1.3 mm yr^{-1}), verringert die Stufe die Auswirkungen der Hebung, da sie die Seitentäler des Goms von der Erosionsbasis der Rhône unterhalb der Stufe isoliert. Die gemittelten Denudationsraten im Goms (~1.3 mm yr^{-1}) ähnelt trotz der fehlenden Verbindung zwischen den Seitentälern und der Erosionsbasis unterhalb der Stufe den rezenten Hebungsraten. Die aus in-situ produziertem ^{10}Be berechneten Denudationsraten (0.6 – 2.1 mm yr^{-1}) zeigen, dass die Beiträge von langsamen Prozessen, wie Bodenkriechen, und schnellen Prozessen, wie Schuttströmen und Bergstürzen, die Erosionsraten der Täler bestimmen und dass Bodenbedeckung zu einer Verringerung dieser Erosionsraten führt. In denselben Tälern nimmt der Anteil der chemischen Verwitterung von den Rücken bis zu den Talflanken ab. Ebenso verringern sich die Erosionsraten mit abnehmender Temperatur, was auf eine kinetisch kontrollierte chemische Verwitterung mit Anteilen zwischen 10 und 50% an der gesamten Denudation hinweist. Dieses steht im Gegensatz zur heutigen Meinung, dass die chemische Verwitterung eng mit der physikalischen Erosion in Verbindung steht.

Zum Schluss zeige ich, dass die relativ großen Eisvorschübe der Gletscher nach dem LGM nicht allein mit Schwankungen der Temperatur, wie sie von Paläoklima-Proxies in den Alpen angezeigt werden, erklärt werden können, sondern dass die von schmelzenden Gletschern des LGM verursachte isostatische Hebung neue Gletschervorschübe begünstigt hat, was nicht unbedingt weitere klimatische Schwankungen erfordert.

Die hier vorgestellten kleinräumigen Vorgehensweisen zur Berechnung der Denudationsraten mit kosmogenen Nukliden und zur Berechnung des Anteils der chemischen Verwitterung an der gesamten Denudation durch chemische Abreicherung in Böden liefern Antworten auf bisher ungelöste Fragen. In Orogenen wie den Europäischen Alpen sind Ungleichgewichte nicht unüblich. Die Einzugsgebiete in den Zentralalpen reagieren auf Störungen durch Änderungen der relativen Anteile von langsamen und schnellen Denudationsprozessen. Die Reaktionszeiten der einzelnen Einzugsgebiete innerhalb eines Gebirges können sehr unterschiedlich sein.

Die hier vorgestellten Methoden können auch auf andere Gebirgstypen angewendet werden. Die nächsten Fragen sind: Wie unterscheiden sich die Denudationsprozesse zwischen Gebirgen, deren Hebung allein durch isostatischen Ausgleich und solchen, die durch aktive Konvergenz hervorgerufen werden? Und sind die Mechanismen und Prozessraten (Hebung, chemische Verwitterung und physikalische Erosion), mit denen ein Einzugsgebiet auf Störungen reagiert, in Gebirgen im Gleichgewicht in beiden Gebirgstypen gleich, wobei Störungen in letzterem Fall eher tektonischen als klimatischen Ursprungs sind?

Schlagwörter: Kosmogene Nuklide, Europäische Alpen, Erdoberfläche Prozessen

1. Introduction

1.1. Motivation

Weathering systems in mountainous regions have the potential to not only drive climate change, but also provide us with an understanding of the feedback loops between climate and surface processes (Raymo and Ruddiman, 1992). Weathering of the silicate rocks that make up most mountain ranges is the largest reservoir for long-term CO_2 drawdown, acting to reverse trends of global warming and to stabilize the climate (Walker et al., 1981; Berner et al., 1983). Before we can estimate the temporal and spatial scales of these processes, we first need to know the rates and conditions under which these rocks weather. Knowing these rates will help climate modeling studies to better constrain the contributions of surface processes on long-term climate change. The reverse view also holds true. By determining how surface processes have reacted to previous changes, we can better understand what impact modern climate change will have on Earth's surface systems.

In-situ produced cosmogenic nuclides in stream sediments (Brown et al., 1996; Granger et al., 1997) provide one of the few methods for determining rates of denudation at the basin scale for time spans of interest to paleoclimate scientists and surface process researchers. In this method, basin-averaged denudation rates are calculated from the concentration of a cosmogenic nuclide, normally ^{10}Be or ^{26}Al, in stream sediments as determined from isotope ratio measurements on an accelerator mass spectrometer (Synal et al., 1997). This requires that the sediment is representative of the drainage basin as a whole, and that the surface has been eroding at the same rate for a sufficient period of time so that steady state with respect to the cosmogenic nuclide inventory has been achieved (Bierman and Steig, 1996; von Blanckenburg, 2005). Denudation rates can also be determined from in situ-produced cosmogenic nuclide concentrations in soils and saprolite, yielding insights into rates of regolith production and removal (Heimsath et al., 1999; Riebe et al., 2004a). Combining these soil based denudation rates with chemical weathering fractions, CDF, derived from immobile element enrichment in soils provides a direct measure of coupling between chemical weathering and physical erosion (Riebe et al. 2001a, 2001b).

The end of the Pleistocene was a time of rapid climate change resulting in world-wide retreat of ice sheets and glaciers (Rasmussen et al., 2006; Shakun et al., 2007). The removal of ice from these surfaces has had a profound impact on Holocene landscape development and surface processes. Glacio-isostatic rebound is still an active agent of uplift in many

formerly glaciated regions (Farrand, 1962; Gudmundsson, 1994; Lambeck et al., 1998; Persaud and Pfiffner, 2004; Champagnac et al., 2007). Large quantities of unweathered material were left behind as the ice melted back, possibly leading to rapid chemical weathering rates (Taylor and Blum, 1995; Anderson et al., 2000) and global CO_2 drawdown.

It is through the integration of geochemical rate determinations and geomorphic analyses that the response of surface processes to external forcing such as climate change, orogenesis, or glaciation may be studied. The following document attempts just such an analysis. The goal of this work is to identify and quantify the dominant processes by which mountain systems respond to climate change or tectonics in the form of changes in temperature and precipitation, glaciation, baselevel lowering, and faulting.

1.2. A brief introduction to the Geology and Geomorphology of the European Alps

The introduction to the European Alps is presented in two parts. First the formation of the Alps is considered, with particular focus on the Swiss Molasse and External massifs, in which units the majority of this work was conducted. This is followed by a review of Alpine glacial history.

Late in the Paleozoic, Alpine basement rocks were folded and metamorphosed during the Variscan orogeny, which ended with the break up of Pangaea. In the Jurassic Period (around 150 million years ago) the future Atlantic and Tethys oceans opened. In the area that is now the Alps, there were shallow seas interrupted by the occasional small island groups. Along with the production of oceanic crust, sediment accumulated on the continental shelves and ocean basins which become the rocks (carbonates, ophiolites, various sediments such as the Bündnerschiefer) of the Helvetic, Penninic, and Austroalpine belts (Schmid et al., 1996). In the Cretaceous Period (~100 million years ago), the basin between Africa and Europe began to close. This caused subsidence and deformation of these belts, as well as more sediment accumulation in the intervening basin. By the end of the Mesozoic Era (~65 million years ago) there was a large exposed landmass with some shallow basins that were slowly filling up with sediment. The majority of the crustal shortening in the Alps began in the Oligocene and continued into the Miocene (approximately 40-15 million years ago) (Pfiffner et al., 1990). At this point, the external Aar and Gotthard massifs were uplifted. The Helvetic and Penninic belts were thrust up on top of one another to form nappes to the north and south of the high Central Alps (Frisch et al., 1998; Schmid et al., 2004). At the same time, large basins were formed on the margins of the mountains, and began to fill up with the

material that was being shed off the rising peaks and sediment. To the north of the Alps, these sediments became the Molasse, ranging from muddy marine rocks, delta deposits, and lagoon sediments to floodplains and gravel alluvial fans (Schlunegger et al., 1997). Also during the main phase of Alpine mountain building, or possibly a bit after, the Jura Mountains to the north were detached from the European basement rocks and folded into the arc that we see today (Laubscher, 1992).

Repeated glaciations during the Pleistocene ended with the Last Glacial Maximum, LGM, during which the Central Alps were home to numerous ice domes with surface elevations above 2500 m (Florineth and Schlüchter, 1998; Kelly et al., 2004) which sent ice flowing as far as the Swiss Mittelland. In the Mittelland, regions of higher elevations such as the Napf between Bern and Luzern and the Hörnli near Zurich remained ice free throughout the LGM. Throughout the Pleistocene glaciations, thick ice in the Rhone and Rhine valleys helped to carve deep U-shaped valleys and depressed the crust by their enormous mass. Ice retreat from the LGM in the Mittelland began around 21 ka (Ivy Ochs et al., 2004), ending in ice free passes by about 15 ka (Kelly et al., 2006). This period, roughly correlative with the Older Dryas was marked by repeated advances of the small valley glaciers during the Gschnitz, Clavadel, and Daun Stadials (Ivy Ochs et al., 2006). The Bølling-Allerod interstadial followed, with near modern temperatures and mostly ice free mountains. Climate deteriorated again during the Younger Dryas cold period, leading again to advance of glaciers, termed the Egessen Stadial. The Preboreal interval brought an end to the Egessen glaciers and the Pleistocene. The Holocene has been marked by numerous, albeit smaller, glacier fluctuations in the Alps (Hormes et al., 2001; Joerin et al., 2006), with notable advances during the Boreal interval, ~8.8 kyr B.P., and the Little Ice Age. Important for cosmogenic nuclide studies is most large Alpine valleys have not been glaciated since the LGM.

1.3. Organization

The work is separated into 6 chapters and 3 appendices. First, an introduction to the Alps and the motivation for and organization of this work are presented. This is followed by five case studies focusing on individual aspects of geomorphic response. Finally, in the 3 appendices the theoretical background of cosmogenic nuclide, geochemical mass balance and GIS methods and procedures are described in detail.

In Chapter 2, a part of the basin averaged denudation rate method, topographic shielding calculations from digital elevation data, is approached from a geographic data point of view. Specifically, the effect of varying grid resolutions on calculated topographic shielding factors is determined. This chapter is in press in *Earth Surface Processes and Landforms* (Norton, K.P. and Vanacker, V., 2008, Effects of terrain smoothing on topographic shielding correction factors for cosmogenic nuclide-derived estimates of basin-averaged denudation rates. *Earth Surface Processes and Landforms*. DOI: 10.1002/esp.1700).

This is followed by an analysis of surface response to climate change in the Swiss Mittelland in Chapter 3, where the rates and timing of valley fill and incision in the Napf suggest accelerated denudation rates in the early post-glacial, rapid sediment production, and high rates of denudation in modern incising valleys. This chapter was published in *Geomorphology* (Norton, K.P, von Blanckenburg, F., Schlunegger, F., Schwab, M., and Kubik, P.K., 2008, Cosmogenic nuclide-based investigation of spatial erosion and hillslope channel coupling in the transient foreland of the Swiss Alps. *Geomorphology* 95, 474-486).

Chapters 4 and 5 are based on small scale studies in the Upper Rhone Valley. First, hillslope response to Quaternary glacial conditioning and neo-tectonic faulting in the lateral valleys of the Goms are presented. The interaction between slow diffusive creep and rapid stochastic processes determines the basin-averaged denudation rates. This is followed by Chapter 4 in which the elemental mass loss of individual geomorphic landforms is used to examine the controls on chemical weathering rates in high altitude landscapes.

Chapter 6 is an analysis of geomorphic response to glacio-isostatic rebound in which a new theory concerning the driving forces of Late Quaternary glacial advance are tested using a combination of climate proxies and finite-element modeling.

CHAPTER 2. EFFECTS OF TERRAIN SMOOTHING ON TOPOGRAPHIC SHIELDING CORRECTION FACTORS FOR COSMOGENIC NUCLIDE-DERIVED ESTIMATES OF BASIN-AVERAGED DENUDATION

ABSTRACT

Estimation of spatially averaged denudation rates from cosmogenic nuclide concentrations in sediments depends on the surface production rates, the scaling methods of cosmic ray intensities, and the correction algorithms for skyline, snow and vegetation shielding used to calculate terrestrial cosmogenic nuclide production. While the calculation of surface nuclide production and application of latitude-altitude and paleo-intensity scaling algorithms are subjects of active research, the importance of additional correction for shielding by topographic obstructions, snow or vegetation is the subject of ongoing debate. The derivation of an additional correction factor for skyline shielding for large areas is still problematic. One important issue that has yet to be addressed is the effect of the accuracy and resolution of terrain representation by a digital elevation model (DEM) on topographic shielding correction factors. Topographic metrics scale with the resolution of the elevation data, and terrain smoothing has a potentially large effect on the correction of terrestrial cosmogenic nuclide production rates for skyline shielding. For rough, high relief landscapes, the effect of terrain smoothing can easily exceed analytical errors, and should be taken into account. Here we demonstrate the effect of terrain smoothing on topographic shielding correction factors for various topographic settings, and introduce an empirical model for the estimation of topographic shielding factors based on landscape metrics.

2.1. INTRODUCTION

2.1.1. Applications of in-situ produced cosmogenic nuclides

In-situ produced cosmogenic nuclides are increasingly used to quantify geomorphic process rates. This method has been applied to diverse landscapes (Brown et al., 1995; Matmon et al., 2003b; Vanacker et al., 2007; Norton et al., 2008) and processes, such as the long-held relationship between hillslope gradient and erosion rate (Ahnert, 1970; Granger et al., 1996; Matmon et al., 2003a; von Blanckenburg, 2005). Cosmogenic methods have been combined with topographic and chemical analyses in order to relate the production of sediment on hillslopes to the controlling sediment production and transport processes (Heimsath et al., 2001), and to better understand the relationship between physical erosion and chemical weathering (Riebe et al., 2003), and climate and denudation (Riebe et al., 2001; von Blanckenburg, 2005),.

The laboratory and computational techniques required for cosmogenic nuclide studies are becoming increasingly available to the earth science community. International projects such as CRONUS and CRONUS-EU (Schaefer, 2005; Dunai, 2005) are working towards increased precision in cosmogenic nuclide methods and analysis techniques. The goal of these initiatives is to reduce errors associated with production rates, scaling, and analytics to 5%. Currently, these errors are between 10 and 20%. As analytical and theoretical errors continue to be reduced the relative importance of the common correction factors, such as topographic and snow shielding, increases. Therefore, any method for calculating these factors should aim to be more accurate than the 5% goal of these studies.

2.1.2. Cosmogenic nuclide production and shielding

In-situ cosmogenic nuclides are produced in bedrock and regolith by the interaction of cosmic rays, primarily nucleons and muons (Lal, 1991; Granger and Muzikar, 2001), with target elements, such as oxygen. The depth to which the rays penetrate in rock or sediment is dependant on their energy, typically in the MeV range at the surface (Gosse and Phillips, 2001), and angle of incidence, $0 - 90°$. At the surface, the first variable, energy, tends to decrease with distance from the equator due to interactions with Earth's magnetic field, and is well modelled with a series of scaling laws (Lal, 1991; Dunai, 2000; Granger and Muzikar, 2001). The second factor, angle of incidence, has a large influence on the resulting production rate (Dunne et al., 1999), but is less easily quantified due to skyline shielding.

Part of the difficulty is due to the dependence of the energy spectrum on the angle of incidence. Cosmic rays with trajectories normal to a horizontal surface have higher energies than those that approach at more acute angles. If this was not the case, and all cosmic rays had the same energy, then skyline shielding would simply be the ratio of obstructed skyline to total unobstructed sky. However, because of the variation in energy with angle of incidence, not only the amount of shielding provided by an obstruction, but also the angle to that obstruction must be determined. In exposure dating, the angle to the horizon from the sampling location in all directions is measured, and the degree of skyline shielding calculated. The situation becomes more complex when landscape scale denudation information is required.

Basin-averaged denudation rates are estimated from the concentration of in situ-produced cosmogenic nuclide concentrations in sediments, collected from an active stream channel, or from recent deposits (floodplains, point bars, etc.). This sediment is assumed to be an amalgam of grains that are released from all parts of the landscape in proportion to their long-term denudation rate (Brown et al., 1995; Granger et al., 1996). The nuclide concentration measured is then a mass balance weighed mean of the contributed concentrations from all points in the watershed. The nuclide concentration at any given point in the basin will depend on the production rate and denudation rate at that location. Topographic shielding, in which cosmic rays are blocked from reaching a surface by surrounding obstructions, becomes an important issue in locations where the land surface is rough (i.e. high relief). Therefore, an accurate assessment of topographic shielding would include measurement of the angle to the horizon in all directions from every point in the basin. While this poses a prohibitive field problem, it can be solved in a geographic information system, GIS, by determining the inclination to the horizon in all directions from every pixel in a watershed using digital elevation models, DEMs (Codilean, 2006). In this way, a representative topographic shielding factor can be calculated, and the production rate scaled accordingly.

2.1.3. Topographic scaling in geomorphology

DEMs are now widely used for geomorphic analyses. Most topographic metrics such as slope and roughness scale with the resolution of the input elevation data (Wolock and
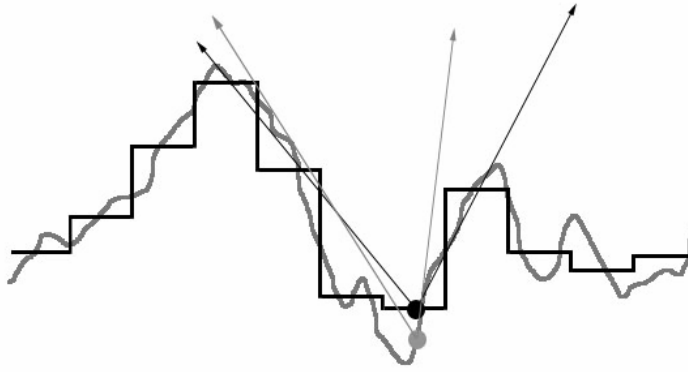
Figure 1. Conceptual model of the effects of terrain smoothing on calculated shielding factors. At high resolution (grey line), the incident angle of shielding (grey arrows) is larger than when a coarser resolution (black line) terrain model is used (black arrows). Note that DEM based methods will use the center point of a cell as the x,y coordinate.

McCabe, 2000; Zhang et al., 1999; Zhang and Montgomery, 1994). Wolock and McCabe (2000) also noted that the type of terrain, i.e. rolling hills, mountains, etc., affects the degree of scaling caused by terrain discretization and terrain smoothing, with terrain smoothing being especially important in mountainous terrains. The result is a skewing of the calculated topographic metrics. In the case of slope and roughness, values decrease with increasing grid size.

If slope and relief measured in a drainage basin depend on the pixel size, then it is likely that the DEM-based estimates of topographic shielding factors will as well. Terrain smoothing through increasing grid size causes a reduction in the relief (local and global) across an area. In other words, the highest peaks are brought down, and the deepest valleys are raised. This leads to a decrease in the angle of inclination to the horizon for any given point on a surface (Figure 1). Because terrain smoothing changes the relief of a landscape but not the overall shape, there will be little to no effect on the subtended angle of shielding (i.e. the width of the obstruction). The angle of inclination will increase as relief increases (if the horizontal scale is held constant), and will decrease as grid size increases. The subtended azimuthal angle will vary depending on terrain complexity, but should remain relatively constant with changing grid sizes.

Here we undertake a systematic study of the effect of scaling caused by terrain smoothing on the estimates of topographic shielding. A wide range of natural terrains with different topographies (i.e. plains, canyons, mountains, etc.) are analysed to capture maximum variability of surface roughness. We propose an empirical model for estimating topographic shielding factors based on topographic roughness, which allows a determination

of the errors associated with terrain smoothing for various topographic settings. We limit our study to the range of resolutions of input elevation data grid sizes that are commonly used for geomorphic applications. The lower limit of raster resolution used in this study is 5 m. The smaller that an obstruction becomes, the more likely it is that cosmic rays will pass through it without interaction in which case shielding no longer takes place. In the case of an infinitely small grid size, i.e. a 1:1 scale map (Eco, 1994), the calculated shielding values would be too high as much of the surface variability would be at scales smaller than the attenuation path length, , i.e. the path length required to attenuate the cosmic ray intensity by a factor of e^{-1}. Our choice of 5 meters represents a conservative estimate that should not introduce a bias into the calculated shielding factors. Datasets at even these resolutions are beyond the operating budgets of most cosmogenic nuclide projects.

2.2. MATERIALS AND METHODS

2.2.1. Topographic shielding

According to Dunne et al. (1999), the total flux of cosmic rays at any point can be calculated using;

$$F = \int_{\varphi=0}^{2\pi} \int_{\theta=0}^{\pi/2} I(\theta, \varphi) \cos\theta \; d\theta d\varphi \qquad\qquad 1$$

where I_0 is the maximum intensity of cosmic irradiation, θ is the angle of elevation measured up from the horizontal (inclination angle), φ is the subtended angle of incoming radiation, and m is an experimentally determined constant, commonly assumed to equal 2.3 (Nishiizumi et al., 1989). The maximum cosmic flux, the zero shielding end member, can be calculated as;

$$F_{max} = \frac{2\pi I_0}{m+1} \qquad\qquad 2$$

The topographic shielding factor, S_f, the ratio of the remaining cosmogenic flux to the maximum (unshielded) cosmogenic flux, is then given by Dunne et al. (1999) as;

$$S_f = 1 - \frac{1}{360°} \sum_{i=1}^{n} \Delta\varphi_i \sin_{m+1}\theta_i \qquad\qquad 3$$

In terms of equation 3, terrain smoothing through increasing grid size causes a reduction in the DEM-based estimate of the elevation angle of obstruction and an underestimation of the effect of skyline shielding. For example, if the elevation angle changes from 45° to 30°, the calculated topographic shielding factor, assuming a 180° obstruction, would increase from approximately 0.84 to 0.96 (Dunne et al., 1999), where a value of 0 represents complete shielding, and a value of 1 no shielding (note that this nomenclature is based on precedence and is used for ease of comparison with previous cosmogenic nuclide publications). The subtended angle will not tend to change, as the overall shape of the landscape remains the same. This in contrast to the alternative method of using relief shadow modelling to account for topographic shielding. Codilean (2006) found that both methods produce similar results.

An algorithm was developed, which calculates the elevation angle for each grid cell within the drainage basin to every other cell of the digital elevation model for each 5° azimuth bin. The maximum elevation angle within each 5° bin is then used as an approximation of the elevation angle for that bin. The magnitude of topographic shielding within the entire drainage basin was then estimated by the basin-averaged topographic shielding factor, S_{basin}, calculated as the average value of the shielding factors, S_f, of all pixels within the basin. The basin-averaged shielding factor, S_{basin}, is an overall estimate of the ratio of the remaining surface flux, $F_{max} - F_{shield}$, to the maximum flux, F_{max}, (Dunne et al., 1999). As such, it is a quantitative measure of the importance of topographic shielding.

2.2.2. Topographic metrics

Relief measurements are inherently scale dependent. Many methods have been proposed for the measurement of surface roughness and relief (Zhang et al., 1999; Wolock and McCabe, 2000; Shepard et al., 2001). Of all of these methods, those involving variograms describing the scale dependence of a spatial variable are the most useful for this application. Experimental variograms estimate the variance of a spatial variable at changing measurement scales or lag distances, and can be used to estimate the potential effects of changing grid sizes of spatial data on topographic metrics. The change in any topographic metric (such as the topographic shielding factor) with grid size can then be estimated from the slope of the variogram. This type of scaling method for the estimation of topographic

metrics at various grid sizes is only valid if the topographic surface is self-affine. The fractal nature of a surface can be tested by plotting the semi-variance of a surface against the length interval of measurement (Shepard et al., 2001). Surfaces which produce linear regressions when plotted in semi-log space are self-affine, and therefore scaleable. Shepard et al. (2001) also describe surfaces with linked linear and polynomial regressions, which represent deviations from the fractal assumption. This provides a means to measure the scales over which surfaces are self-affine, and at which scales that relationship breaks down.

We use the observed sample variance of the elevation data calculated at varying measurement scales or lag sizes to characterize the roughness of a surface (e.g. Figure 6). For a given landscape, the variance increases as the relief increases while holding the horizontal measurement scale the same. In order to compare landscapes, the variance at equivalent lag sizes must be analyzed. We arbitrarily chose a lag distance of 1000m, corresponding to a 1km length scale as the test size. At this measurement scale, the variograms are mostly linear, suggesting self-affine behaviour, and the sample variances are sufficiently different to provide meaningful correlations.

2.2.3. Data sources and terrain smoothing

The analysis involved the investigation of a wide range of natural terrains in order to capture maximum variability of surface roughness. A variety of data sources at varying scales were analyzed. Ten drainage basins of about 3 to 30 km² selected at five different locations represent a wide range of topographic expressions (Figures 2 and 3): (1) extremely

Table 1. Geomorphic parameters for the studied drainage basins.

| | Area (km) | Elevation (m) | | | Slope (deg) |
		Minimum	Maximum	Average	Average
Andes 1	25	3443	3811	3062	32
Andes 2	25	2818	3933	3402	31
Andes 2	30	2356	3227	2700	24
Flanders1	12	64	115	91	3
Flanders2	12.1	58	122	85	3
Flanders3	70.6	30	82	49	1
Jackson1	5.8	2291	3613	3018	30
Jackson2	3.4	2387	4200	3224	37
Canyon	7.7	937	1772	1518	19
Appalachians	10.3	931	1577	1174	28

flat terrain, Flanders, Belgium; (2) mature fluvial valleys, Appalachians, USA; (3) incised canyons, Arizona, USA; (4) steep mountain valleys, Andes, Ecuador; (5) glacial mountain valleys, Wyoming, USA.

For all drainage basins, high resolution DEMs (grid size < 10m) were available from LIDAR surveys (Flanders), stereo aerial photography (Andes), or digitized topographic maps (USA) and medium resolution data (grid size = 90m) from the SRTM dataset (Rabus et al., 2003). In order to study the effect of grid size on estimates of topographic shielding, the high resolution elevation data were resampled at increasing grid sizes. All datasets were reprocessed to about 10, 30, 90, 250, 500 and 1000m resolution. Resampling utilized zonal mean aggregation from the original high resolution raster.

Figure 2. Locations of test terrains.
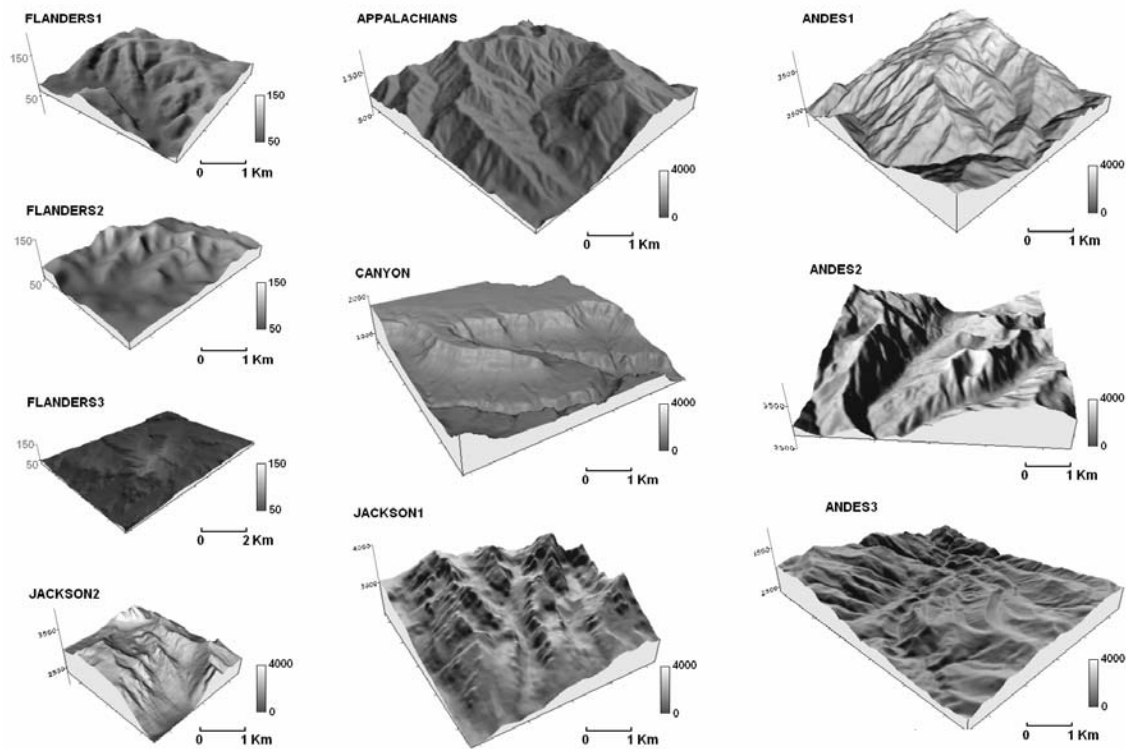
Figure 3. Three-dimensional shaded relief images of the test basins (10× vertical exaggeration for Flanders, 1× vertical exaggeration for Jackson, Appalachians, Canyon and Andean test terrains

2.3. RESULTS AND DISCUSSION

2.3.1. Shielding at the basin scale

The role of shielding with respect to single bedrock samples for exposure dating has been extensively studied and is fairly well constrained (Lal, 1991; Gosse and Phillips, 2001; Dunne et al., 1999). As cosmogenic nuclides began to be used for basin-averaged denudation rates, the methods already in place from exposure dating were expanded to encompass the entire watershed, as described above. The strongest argument against this type of analysis is that the cosmogenic flux is independent of topography, and thus strongly shielded areas such as valleys must be offset by an equal increase in other parts of the basin, presumably ridges. If this is true, then the shielding factor calculated over an entire basin must be 1 (representing no shielding). While this is an attractive theory, we believe that it is too simplistic, and that the calculation of basin-averaged shielding factors is necessary.

Basin-averaged shielding factors are calculated from digital elevation data, DEMs (Codilean, 2006), digital representations of ground surface topography or terrain. The most

13
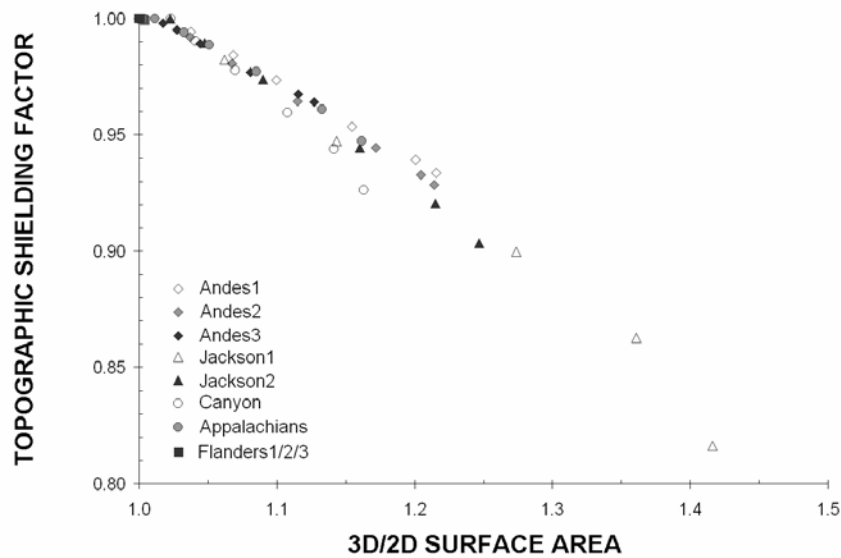
Figure 4. Plot of the ratio of the 3D to 2D surface area against basin-averaged shielding factor, S_{basin}.

common structure for a DEM is a regular array of squares of equal size, and hence equal area. Because of this, surface areas and all metrics calculated from them, are 2D surfaces. Earth however has a 3D surface. The 3D area is the true area of the surface, while the 2D area is simply the same form projected onto a horizontal plane. In topographic terms, the higher the surface roughness and relief, the larger the 3D surface area, but the 2D area will remain constant. If the flux of cosmogenic rays entering a drainage basin remains constant (Lal, 1991), then the maximum flux density occurs in the case of a planar surface, $Area_{2D} = Area_{3D}$. As the surface becomes rougher, the 3D area will increase as the 2D area remains constant. In this case, the same flux is spread over a larger ground surface. Topographic shielding is a redistribution of this cosmic ray flux over the entire surface area. If this is true, then calculated shielding factors should correlate very strongly with 3D surface area, which proves to be the case (Figure 4).

2.3.2. Shielding estimates depend on grid size

Grid size has a marked effect on the topographic shielding factor calculated for a surface. At high resolution, the largest S_{basin} values, as much as 0.80, are measured for steep mountainous terrains and narrow canyons. The lowest shielding values, measured for flat terrain in Flanders, are indistinguishable from 1. Increasing grid size in all cases results in topographic shielding factors that approach 1 (Figure 5). Regardless of surface roughness, no significant shielding is apparent in the studied watersheds when the grid size exceeds ~500m. When the

basin-averaged topographic shielding factor, S_{basin}, is plotted against grid size (Figure 5), a log-linear relation is observed between the two variables. For most terrains, the goodness of fit of the regression, as measured by the R^2 coefficient is greater than 0.90, indicating very good fits. The exceptions are the flat terrains of Flanders in which the low relief results in
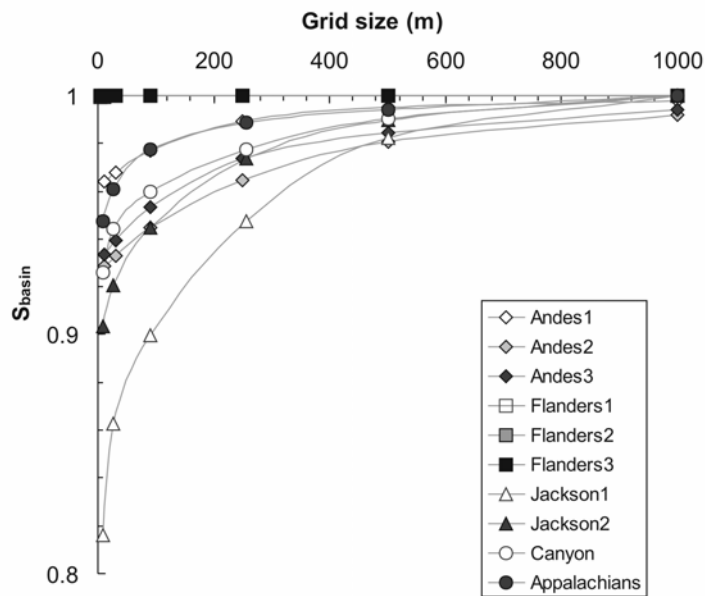
Figure 5. Plot of basin-averaged shielding factor, S_{basin}, against grid size for each test terrain.
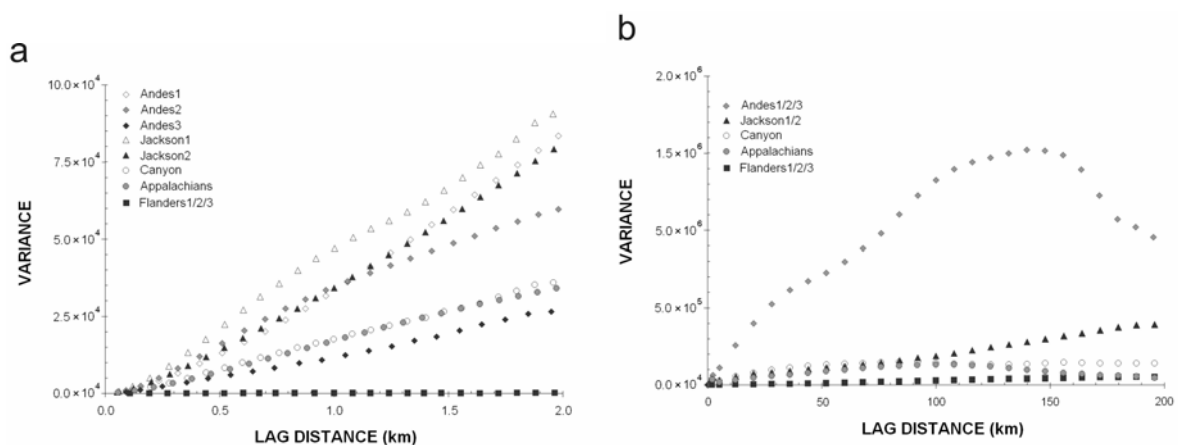
Figure 6. Variograms, sample variance of elevation against lag size, of the test terrains. Higher variance implies rougher terrain. a) Lag size up to 2km. Note that the linear relationship for this interval suggests self-similar, i.e. scaleable, landscapes. b) Lag size up to 200km.

very low shielding factors at all grid resolutions. The significance and robustness of the regressions suggests that a correction coefficient may be calculated for the topographic shielding factor. Wolock and McCabe (2000) also identified simple correction factors for slope and catchment area from 100m and 1000m DEMs from a larger dataset, consisting of 50 locations from a variety of terrains in the US.

2.3.3. Decrease of shielding estimates with grid size depends on terrain roughness

The magnitude of the effect of grid size on topographic shielding factors varies depending on the roughness of the terrain, defined as the relief of a surface over a given distance. Rougher surfaces provide higher shielding factors, and the rate of change with increasing cell size is larger for highly variable terrains than for flatter terrains. The variograms for each DEM (Figure 6) provide quantitative measure of the surface roughness. At a lag size of 1000 m, the lowest sample variances, approximately 100, are found in Flanders, and the highest, nearly 50,000 in the glacial landscapes in Wyoming. When S_{basin} is plotted against the sample variances calculated for a lag distance of 1000m (Figure 7a), a linear relationship with an R^2 value of 0.94 is obtained.

The relationship between the topographic shielding factor and grid size is a log-linear function of the form

$$S_{ba\sin} = a \ln(G) + S_0 \qquad\qquad 4$$

where S_{basin} is the basin-averaged topographic shielding factor, G is the grid size (m), a is a coefficient related to the local variability in surface elevation, and S_0 is the theoretical maximum shielding factor (Figure 5).

The rate of decrease of the topographic shielding factor with increasing grid size, the coefficient a in equation 4, is a function of the topographic roughness. All measurements of topographic roughness are dependent to some degree on the distance, or scale over which roughness is measured. This dependence can be minimized by using the entire analysis area (i.e. the drainage basin) as the measurement scale (Zhang et al., 1999) . We used the sample variance of the elevation data, calculated by averaging the difference squared of the elevation values over all pairs of observations over an arbitrarily chosen lag interval from a 90m SRTM elevation grid, to characterize the local variability in elevation of each surface (Zhang et al., 1999). The SRTM data were chosen because of the practicality of this dataset. Not only

Table 2. Calculated basin-averaged shielding factors, S_{basin}, for each raster from the SRTM 90m dataset, sample variance at 1000m lag distance from the same elevation models. The roughness coefficient, a, and theoretical maximum shielding value, S_0, are reported with the corresponding R^2 values.

	S_{basin}	Sample variance	a	S_0	R^2
Andes 1	0.95	33500	0.0140	0.8958	0.9736
Andes 2	0.94	34500	0.0145	0.8874	0.9471
Andes 2	0.98	11500	0.0081	0.9427	0.9736
Flanders1	1.00	95	0.0001	0.9996	0.7655
Flanders2	1.00	110	0.0001	0.9993	0.7469
Flanders3	1.00	40	0.0000	0.9999	0.4416
Jackson1	0.90	48000	0.0402	0.7269	0.9952
Jackson2	0.94	33500	0.0218	0.8515	0.9886
Canyon	0.96	18000	0.0157	0.8914	0.9965
Appalachians	0.98	16800	0.0114	0.9236	0.9909

does it have near global coverage at a moderate resolution, but it is also freely available to all researchers. Figure 7b clearly indicates that the rate of decrease of the topographic shielding factor with increasing grid size is a function of the sample variance of the surface. The resulting regression line, with an R^2 value of 0.83, validates the use of the experimental variograms as an approximation for surface roughness.

The predictability of the effect of grid size on S_{basin} means that the shielding factors that would be calculated from a high resolution grid may be estimated using coarser elevation data. So for any grid size, G, a theoretical maximum topographic shielding factor, S_0, can be estimated. In figure 7c, we plotted the maximum topographic shielding factor, S_0 of each data set against the sample variance calculated for a lag interval of 1000m using 90m SRTM data. A robust correlation, $R^2 = 0.87$, relates these two variables. Therefore, a corrected shielding factor can be estimated for any input surface by calculating the surface roughness in the form of the variogram.

a)

$y = -2E\text{-}06x + 1.0011$
$R^2 = 0.9383$

b)

$y = 7E\text{-}07x - 0.0003$
$R^2 = 0.8374$

c)

$y = -5E\text{-}06x + 1.0016$
$R^2 = 0.8732$
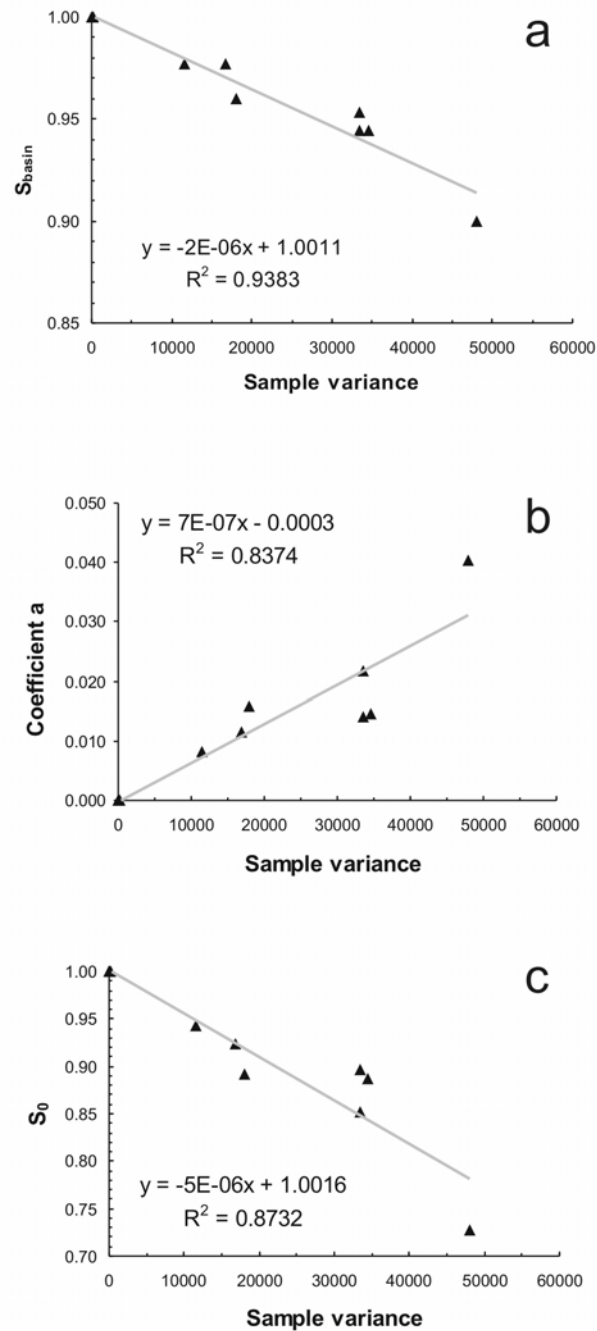
Figure 7. a) Plot of basin-averaged shielding factor, S_{basin}, against sample variance at 1000m calculated from the 90m SRTM data. b) Roughness coefficient, a, against the sample variance. c) Theoretical maximum shielding factor, S_0, against the sample variance for each test terrain.

2.3.4. Is there an ideal grid size for measuring topographic shielding?

The ideal grid size for measuring topographic shielding will depend on the roughness of the surface (height and width of obstructions). As obstructions get smaller, the distance that a cosmic ray travels through the obstruction gets close to the particle attenuation length (Gosse and Phillips, 2001). As a consequence, part of the cosmic radiation will pass through

the obstruction and the obstruction itself will not provide complete shielding. Therefore, calculating topographic shielding at an indefinitely small grid size is not relevant, as much of the surface variability would be at scales smaller than the particle attenuation length.

For any obstruction of height, H, and width, W, the distance that cosmic rays travel through the obstruction depends on the inclination angle of the incoming radiation, θ, measured up from the horizontal (Figure 8); and can be calculated as

$$X = \frac{W}{\cos\theta} \qquad \text{for } \theta \leq \arctan(H/W) \text{ and}$$

$$X = \frac{H}{\sin\theta} \qquad \text{for } \theta > \arctan(H/W)$$

5

The longest distance that can be made through an obstruction of a given dimension (height and width) equals

$$X = \sqrt{H^2 + W^2}$$

6

We made a first estimate of the ideal grid size by calculating the minimum 'relevant' grid size at which an obstruction of a given dimension (height and width) provides topographic shielding. The smallest obstruction that has any measurable effect on the calculation of the topographic shielding factor has a width that equals the grid size, G, of the digital elevation model (i.e. one pixel by one pixel). We assume that topographic shielding becomes negligible once the longest distance travelled through an obstruction of one-pixel width, X, drops below
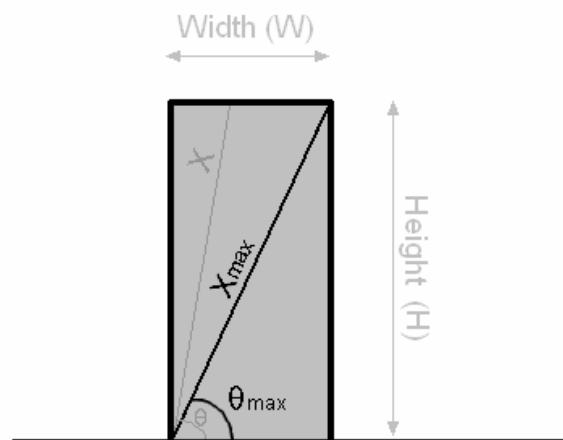
Figure 8. Schematic 2D model of the effect of any obstruction of height, H, and width, W, on topographic shielding.
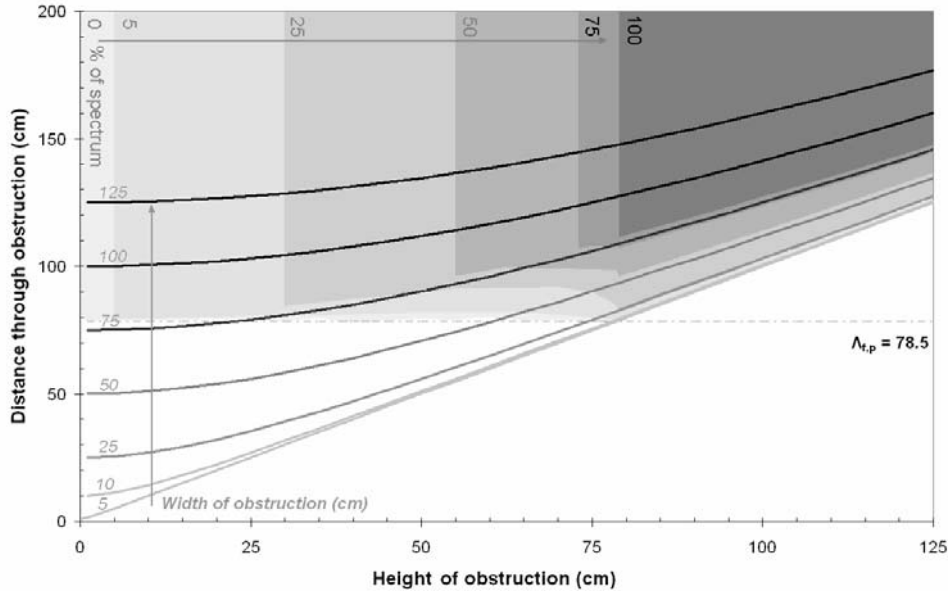
Figure 9. Plot of the distance that a cosmic ray will travel through an obstruction of a given height and width. This figure allows the estimation of the importance of an obstruction of a given height (from 0 to 125 cm) and width (from 0 to 125 cm) on topographic shielding, as it shows the longest distance that cosmic rays can travel through the obstruction (cm, Y-axis), and the percentage of cosmic rays (%) that travel more than one particle attenuation length through the obstruction.

one true particle attenuation length, $\Lambda_{f,p}$. For our estimates, we take $\Lambda_{f,p}$ constant and about 208 g cm^{-2} following (Gosse and Phillips, 2001). For rocks with a density of 2.65 g cm^{-3}, the e-folding length, or depth at which ~63% of the cosmic ray particles have been stopped, is about 78.5 cm.

Figure 9 gives for obstructions of various dimensions (height and width), the longest distance travelled through a one-pixel width obstruction. The results of this 2D model indicate that topographic shielding becomes measurable once the height or width of the obstruction gets close to the particle attenuation length. The importance of an obstruction of a given dimension for topographic shielding depends on its morphology (height/width ratio), which determines the fraction of the incoming cosmic radiation that travels more than one particle attenuation length through the obstruction. The results from the 2D model (Figure 9) show that the smallest obstructions that can provide significant topographic shielding are blocks of one by one particle attenuation length that surround the pixel of interest. Any obstruction that is smaller than one by one particle attenuation length will not be able to absorb e^{-1} of the cosmic ray particles for a large part of the cosmic ray spectrum. Therefore, measuring topographic shielding at length scales (grid sizes) shorter than one particle attenuation length is not relevant.

2.3.5. When does grid size matter?

For many applications, the approach outlined above could introduce more error into the results than if the uncorrected shielding factors from coarser grids were used. This is especially true in areas with low topographic roughness. A sound approach to determining the applicability of the correction is to compare the error induced by estimating shielding factors from coarse grids to the remaining errors, usually 5-10%. In this case, when the difference between S_{basin} and S_0 is in excess of 0.05 to 0.1, correction of the shielding factor for grid size is necessary. While only one studied area, Jackson1, differs by more than 0.1, all of the regions with moderate relief (i.e. all studied areas excluding Andes2 and the Flanders grids) exhibit greater than 5% difference. Corrections could be accomplished either through the acquisition of a high resolution elevation dataset, or using equation 4 and Figure 7 to calculate the adjusted shielding factor from the 90m SRTM dataset.

2.4. CONCLUSION

Topography reduces in-situ production of cosmogenic nuclides as it (i) shields a certain proportion of the incoming cosmic radiation and (ii) affects the effective path attenuation length by changing the average angle of incidence on sloping surfaces. We used high-resolution digital elevation models to assess the importance of topographic shielding for a wide range of topographic settings. Measured basin-average topographic shielding factors, S_{basin}, decrease as grid size increase. This effect is accentuated in high relief mountain basins, which rough landscapes are exactly those which are most often studied with cosmogenic nuclide derived basin-averaged denudation rates. Because these surfaces appear to be self-affine over the measurement scales used here, a scaling law for the correction of the basin-average topographic shielding factors can be calculated. As rougher terrains are analyzed, the corrections become more important as they become comparable with the magnitude of error introduced through analytical measurements and scaling laws. The goal of any study should be to reduce the associated errors to a minimum. To this end, it is important to use high resolution DEMs or a correction factor for calculated topographic shielding factors.

CHAPTER 3. COSMOGENIC NUCLIDE-BASED INVESTIGATION OF SPATIAL EROSION AND HILLSLOPE CHANNEL COUPLING IN THE TRANSIENT FORELAND OF THE SWISS ALPS

ABSTRACT

Transient landscape disequilibrium is a common response to climatic fluctuations between glacial and interglacial conditions. Such landscapes are best suited to the investigation of catchment-wide response to changes in incision. The geomorphology of the Trub and Grosse Fontanne, adjacent stream systems in the Napf region of the Swiss Molasse, was analyzed using a 2-m LIDAR DEM. The two catchments were impacted by the Last Glacial Maximum, LGM, even though the glaciers never overrode this region. They did, however, cause base levels to drop by as much as 80 m. Despite their similar tectonic, lithologic and climatic settings, these two basins show very different responses to the changing boundary conditions. Stream profiles in the Trub tend to be smooth, while in the Fontanne, numerous knickzones are visible. Similarly, cut-and-fill terraces are abundant in the Trub watershed, but absent in the Fontanne, where valleys are incised as much as 80 m. The Trub appears to be a coupled hillslope-channel system because the morphometrics throughout the basin are equivalent. The morphology of hillslopes upstream of the knickzones in the Fontanne is identical to that of the Trub basin, but different downstream of the knickzones, suggesting that the lower reaches of the Fontanne have been decoupled from the hillslopes. However, the rapid incision of the Fontanne is having little effect on the adjacent upper hillslopes.

We tested this interpretation using cosmogenic ^{10}Be-derived basin-averaged denudation rates and terrace dating. The coupled nature of the Trub basin is supported by the similarity of denudation rates, 350 ±50 mm ky^{-1}, at a variety of spatial scales. Upstream of the knickzones, rates in the Fontanne, 380 ±50 mm ky^{-1}, match those of the Trub. Downstream of the knickzones, denudation rates increase to 540 ±100 mm ky^{-1}. The elevated rates in the downstream areas of the Fontanne are due to rapid incision causing a decoupling of the hillslope from the channel. Basin response time and the magnitude of base level drop exert the principal control over the difference in geomorphic response between the two

basins. The timing of the filling of the Trub valley, 17 ±2 ka, and the initial incision of the Fontanne, 16 ±3 ka, were calculated, verifying that these are responses to LGM perturbations. Unique lithologic controls allow for one of the fastest regolith production rates yet to be reported, ~ 380 mm ky^{-1}.

3.1. INTRODUCTION

The development and decay of transient landscape conditions depend on the magnitude of perturbations, such as base level changes, and the response time of a drainage basin to such changes. In landscapes where channel incision outpaces hillslope response, the hillslope-channel system becomes decoupled, leading to the formation of oversteepend hillslopes and knickpoints in the channels (Dorsey and Roering, 2006; Kirby et al., 2007). On the scale of the entire watershed, knickzone migration leading to steepening hillslopes is the primary means by which changes in the base level of streams are transmitted to the upper basins (Mudd and Furbish, 2005). Locally, hillslope channel coupling controls the degree to
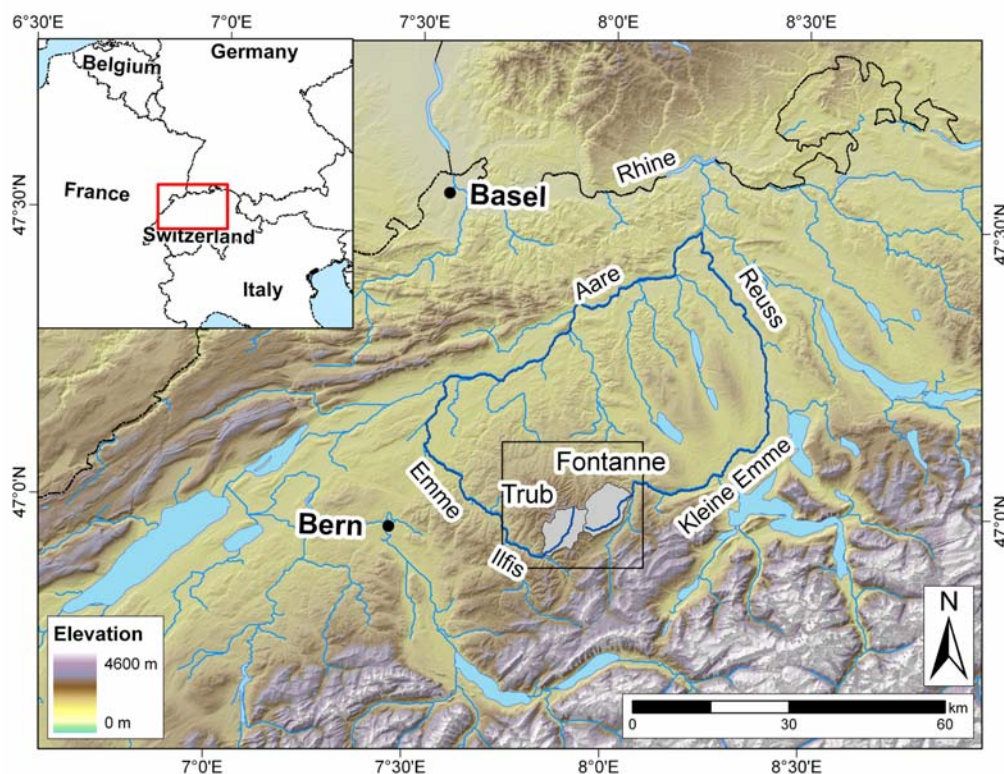
Figure 10. Overview of the study area. The Napf region, indicated by the black box, is drained to the SW by the Trub River into the Emme and eventually into the Aare River. To the NE, the Fontanne River flows into the Kleine Emme and then the Reuss River.

which upper basin hillslopes react to these changes. Streams and hillslopes respond to a drop in base level by increasing sediment flux, steepening slope angles, and increasing slope convexity. Decoupling occurs because hillslopes are unable to respond sufficiently rapidly to the elevation change of the stream. Streams then incise narrow steep gorges, and the upper hillslopes remain graded to the previous landscape. These transient landscapes can provide us with information about magnitudes of perturbations, quantification of thresholds, and time scales for basin response (Pazzaglia and Brandon, 2001).

The Napf area in the Swiss Mittelland (Figure 10) is a classical region that has experienced multiple phases (Müller and Schlüchter, 1997) of base level change of as much as 80 m in relation to glacial-interglacial cycles. Although it is located just outside the LGM margin (Figure 11; Jäckli, 1970; Florineth and Schlüchter, 1998), the advancing ice did cause damming and rerouting of the downstream fluvial systems. Therefore, the Napf provides a unique environment within the Alpine foreland basin in which to quantify the effects of glacial-interglacial fluctuations on a transient landscape. The rerouting of the Kleine Emme near Wolhusen and Emme at Burgdorf resulted in base level drops of ~ 80 m for the Fontanne and 20 m in the Trub system, respectively. While previous studies have identified the
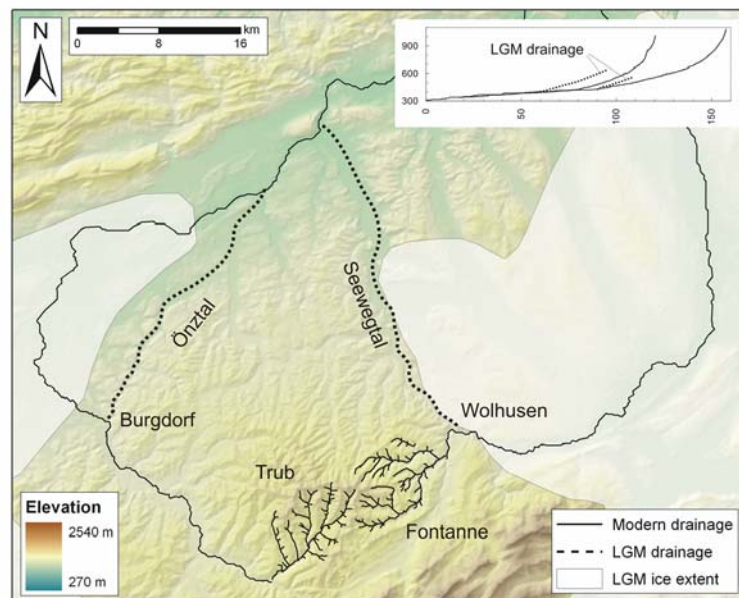
Figure 11. Area map showing approximate LGM ice extent (shaded area, adapted from Florineth and Schlüchter (1998)) and hydrological features. Drainage pathways during LGM are shown as bold, dashed lines. Modern streams are shown as thin black lines. The long profiles of the modern and LGM drainages of the Trub-Emme (longer) and Fontanne-Kleine Emme (shorter) are included in the inset.

responses resulting from these changing boundary conditions (Müller and Schlüchter, 1997; Schlunegger and Schneider, 2005), the associated process rates are still unknown. This is the first study to use cosmogenic nuclides to quantify landscape response to the changing boundary conditions in ice proximal environments. Cosmogenic nuclides, specifically [10]Be, allow us to quantify landscape response rates (Bierman and Nichols, 2004; von Blanckenburg, 2005). Previous studies (e.g., Riebe et al., 2001; Clapp et al., 2002; Morel et al., 2003) have used cosmogenic nuclides in river-borne quartz to correlate denudation rates in transient landscapes. This method is particularly effective for studying response to the last glacial-interglacial transition in the foreland basin of the Alps. The averaging timescales for cosmogenic nuclides in the Mittelland, 2-8 kyr (Wittmann et al., 2007), are short enough that the system is able to reach cosmogenic steady-state within time since the LGM. Because climate, tectonic forcing, and lithology, are equivalent in the two adjacent Napf basins, the calculated denudation rates may be used to determine transient basin response to one variable, i.e., base level change.

3.2. GEOLOGIC AND GEOMORPHOLOGIC SETTING

The Napf is a hilly region in the foreland basin of the Swiss Mittelland. The entire study area is underlain by Middle Miocene Molasse conglomerates. The cobble conglomerates and sandstone layers dip gently to the NW at 5 to 15° (Matter, 1964). This is reflected in shallower NW-facing slopes that are more prone to mass movement than the SE-facing slopes (Schlunegger and Schneider, 2005). The two basins that are studied, the Trub to the SW, and the Fontanne to the NE, are of equivalent size, 57 and 63 km², respectively. Total basin relief, 600-750 m, and mean local hillslope angles as measured from the 2-m LIDAR DEM, 23 to 24°, are also similar. The upper hillslopes in both basins are characterized by variable regolith thickness, typically < 1 m. Downslope movement of sediment in these basins occurs mainly by creep and shallow landsliding. Schlunegger and Schneider (2005) determined the transition from colluvial hillslopes to fluvial channels to typically occur when catchment area reaches 0.1 to 0.2 km². At this point, the dominant form of sediment transport changes from mass wasting to fluvial processes. The presence of bedrock patches on hillslopes and a lack of sediment in the headwater reaches of the stream channels further suggest a weathering-limited sediment flux out of the upper basins
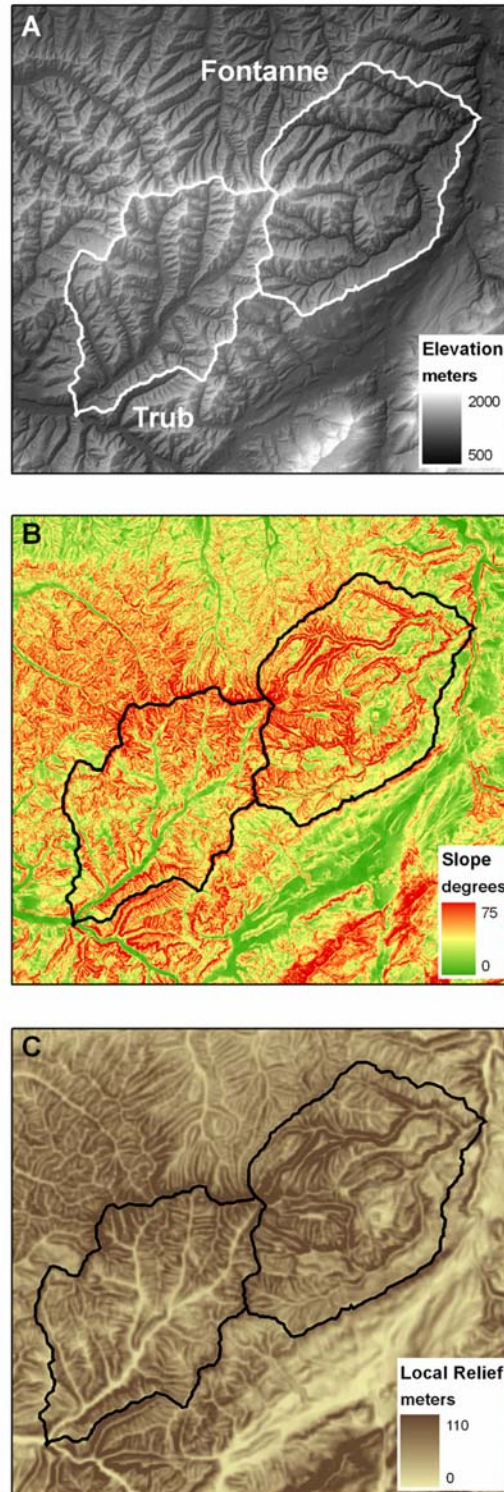
Figure 12. Morphology of the Trub and Fontanne basins based on 2-m LIDAR data. Elevations (A) range from around 600 m in the Fontanne catchment to more than 1400 m in the Trub basin. The average hillslope angle (B) is similar in each basin, but the distribution of slopes is different. Steepest slopes in the Trub are found near the headwaters, while in the Fontanne they are located next to the channels. The highest local relief (C), defined over a length scale of 250 m, is found near the channels in the Fontanne and away from the channels in the Trub. The choice of 250 m is based on the width of the channels in the Napf.
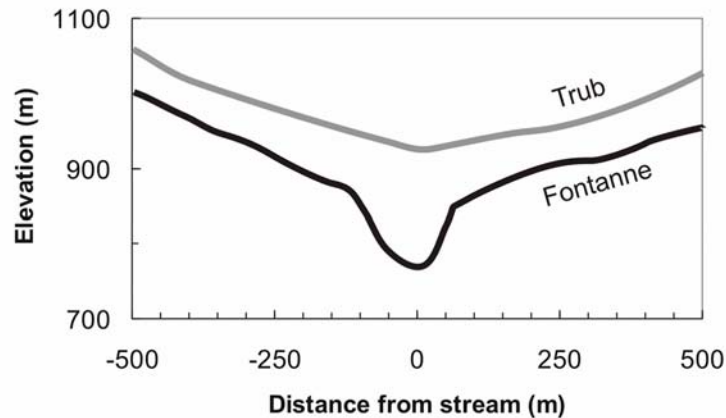
Figure 13. Typical valley cross profiles for the Trub and Fontanne. The Trub valleys (grey), which are buffered by thick valley fill, have smooth channel-to-hillslope transitions. The Fontanne system (black) is dominated by low relief surfaces and recent rejuvenation in the form of incised gorges.

(Schlunegger and Schneider, 2005). In this case, the total denudation rate in the Napf should be controlled by the rate at which sediment is produced on the hillslopes and not by the transport efficiency of the streams.

The Trub and Fontanne differ, however, in their morphometric expression (Figure 12). The Trub is an alluvial stream system with numerous terraces that reach as much as 20 m above the modern stream level. Maximum slopes within the Trub catchment are located in the headwaters, near the main divide (Figure 12B). Local relief is extremely low next to the channels, marking the presence of alluvium (Figure 12C).

Terraces are absent in the Fontanne catchment where fluvial bedrock incision has carved gorges as deep as 80 m. Bedrock-floored sections of the stream occur where prominent knickpoints disrupt the stream system, while the rest of the stream contains patchy alluvial cover. The stream valleys are narrow and deeply incised. In contrast to the Trub, the steepest slopes in the Fontanne basin are located next to the incising streams (Figure 12B), as is maximum local relief (Figure 12C). The same trends can be seen in valley cross profiles (Figure 13). The Fontanne streams, below the knickzones, have pronounced slope breaks where the incision cuts into the upper hillslopes. Throughout the Fontanne catchment, low relief surfaces are present above narrow gorges (Schlunegger and Schneider, 2005).

3.3. METHODS

3.3.1. Site selection

We collected 13 stream sediment samples from the active channels of the trunk streams and tributaries, as well as three samples in a depth profile on one of the Trub terraces (Figure 14). The sediments, consisting of the weathered remains of the Molasse conglomerates, were sieved to < 1 cm in the field. Five samples, Trub1, Trub2, and Trub5 and Fon5 and Fon6, were taken in small (area < 2 km^2) basins below the transition between colluvium and fluvial channels. These samples are believed to be representative of the background, steady-state, denudation rate in the Napf because of their locations in a nonincising basin and above the knickzones, respectively. If erosional steady state is reached for these upper basins, then the rate of denudation is equal to the rate at which bedrock is converted to regolith on the

colluvial hillslopes. In this case, these samples represent the soil production rate. To quantify the effect of the knickzones and subsequent rejuvenation of the Fontanne system, six
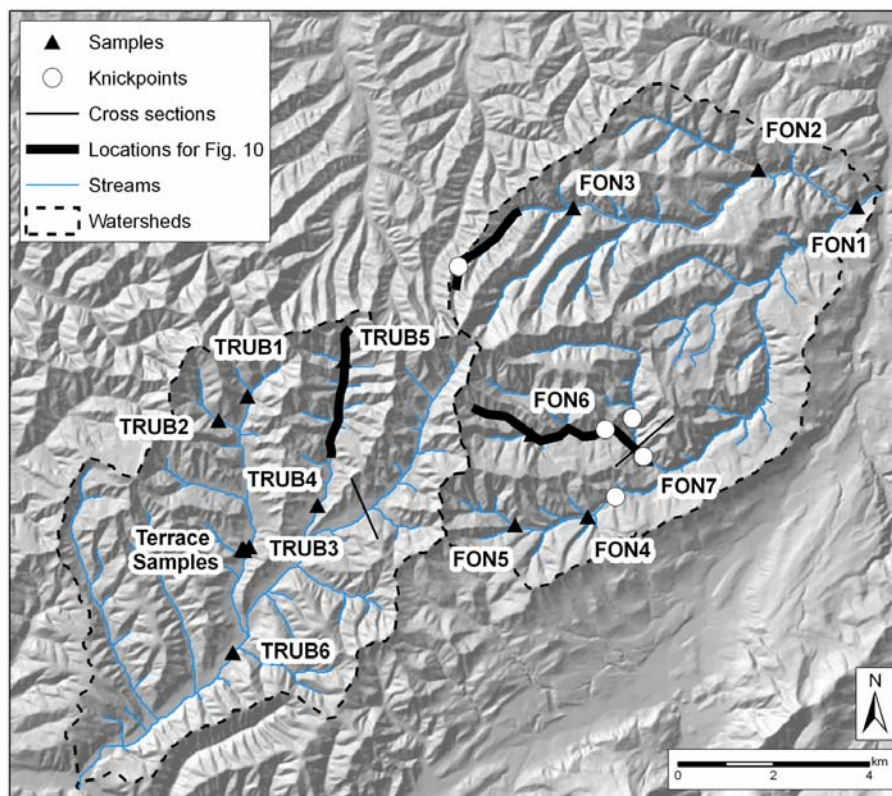
Figure 14. Shaded relief map showing the locations and denudation rates of samples. The locations of the major knickpoints in the Fontanne basin are indicated by a white circle. Valley cross section locations (Figure 13) are shown as thin black lines, and stream reaches used for curvature and slope diagrams (Figure 17) as thick black lines.

sample locations in medium-sized basins were chosen. Fon2, Fon3, and Fon7 were collected below the modern knickpoints, while Fon4 was collected above the knickpoint. Two samples, Trub3 and Trub4, were also collected that were comparable in size to Fon2, Fon3, Fon4, and Fon7. These samples can be used to determine the rate of incision in the Fontanne basin by using a simple mass balance equation relating the nuclide contribution from the nonincised and incised regions. Three terrace samples, TrubT1, TrubT2, and TrubT3, were taken at depths ranging from 1.5 to 8.5 m in a gravel pit exposure. These samples provide information on the age of the terrace-forming event, rates of basin-wide denudation during the fill event, and the concentration of material that might be mixed in the trunk stream. Finally, basin-wide denudation rates were determined from trunk stream samples, Trub6 and Fon1, collected in the downstream portions of each catchment.

3.**3.2. Morphometrics**

Basin morphometrics were extracted using a 2-m LiDAR DEM (provided by the Cantons Bern and Luzern). Local hillslopes, calculated over 3x3 pixels, and relief, based on a 250 m moving window, were used to help determine sampling locations, and the spatial extent of terraces and incision in the Trub and Fontanne basins, respectively. Identification of knickpoints in the Fontanne utilized the visual inspection of channel-long profiles and slope area plots for changes in gradient (Tarboton et al., 1991; Montgomery and Foufoula-Georgiou, 1993; Whipple and Tucker, 1999; Hayakawa and Oguchi, 2006), and stream proximal curvature and slope for evidence of rejuvenation.

Slope area plots and stream-long profiles have been used for identification of knickzones. These data must be augmented with other geomorphic information, as knickpoints in streams can be generated by other mechanisms such as landsliding (Korup, 2006). In regions where the incision event is recent, or response time is long, these methods work well. They can not be used to identify watersheds through which the knickpoints have already passed. The abrupt jumps in slope area plots or inflections in the stream-long profile that normally mark knickpoints (i.e., Clark et al. (2005)) no longer appear after the knickpoint has migrated to the headwaters. The knickzones in the Fontanne basin have already migrated through many of the subcatchments. We therefore created an index capable of identifying modern and previous rejuvenation. The procedure is as follows.

Stream proximal curvatures, and stream proximal slopes, were extracted from the DEMs to identify regions of rejuvenation and hillslope detachment (Figure 15). Curvature

and slope are measured at the resolution of the DEM perpendicular to the stream, and averaged over the entire length of the stream segment. In this case, no alterations were made to the data set (i.e., removal of anomalous low slopes from tributary junctions). The local hillslope curvature and slope angles are plotted against the distance from the stream, normal to stream flow. These parameters can be used as a proxy for the degree of rejuvenation in a catchment. Schlunegger et al. (2002) used hillslope curvature in the Swiss Mittelland to identify rejuvenated landscapes and the dominant sediment transport processes acting on them. In recently incised valleys, hillslopes are convex, the curvature will be ≥ 0, and slope will be high (Figure 15A). This is because the incised gorge tends to have steep, rectilinear
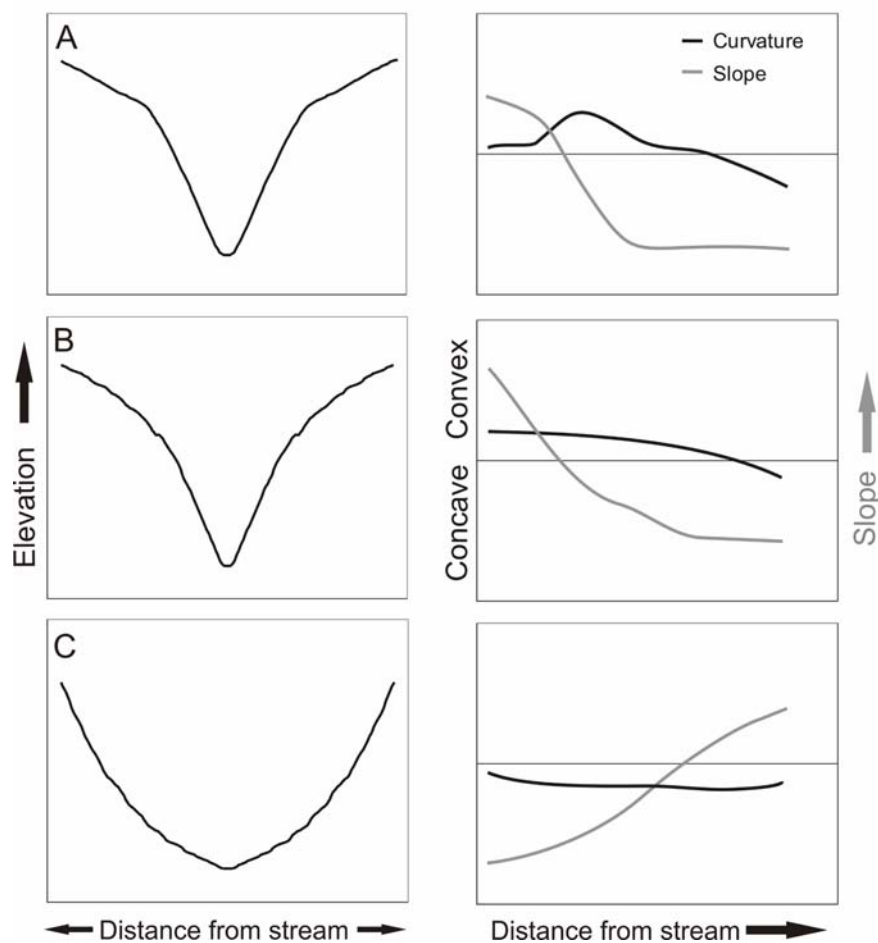
Figure 15. Schematic representation of the stream proximal curvature and slope methods. The left column contains the idealized valley cross profiles used in the right column. The slopes and curvatures are measured perpendicular to the stream and averaged over a given stream length (i.e., a mean cross profile of slope and curvature instead of the normal elevation). For rejuvenated terrains, whether the incision is current (A), or recently past (B), slope angles near the stream will be high, decreasing with distance away from the stream; and the curvature of the hillslope will be 0 or positive. For nonrejuvenating valleys (C), the stream proximal slope angle will be low and will increase away from the stream. Curvature in this case will be 0 or negative.

walls that end in distinct breaks in slope at the relict terrain (Schlunegger and Schneider, 2005). The resulting slope plot will have the highest slope values adjacent to the stream, which will then decrease as the lower gradient, relict landsurface is approached. Curvature in this case will be near 0, or slightly positive, as both the inner gorges and the relict surface are rectilinear. In recovering terrains (Figure 15B), the break in slope between the incised gorge and the relict terrain is less pronounced because of masswasting of the inner gorges and adjacent hillslopes. This may result in more positive curvature, because of the more continual change in slope, but overall, the curvature and slope will not differ significantly from the case of recent rejuvenation because the steepest slopes in the incised region and the shallowest slopes of the relict landscape remain, and the response is mostly to smooth the transition between the two regions. Finally, in the case of a nonrejuvenating, or steady state landscape (Figure 15C), no evidence exists for oversteepening of stream proximal slopes, or knickzones. Slope will be lowest next to the stream and increase to the inflection point of the hillslope. The corresponding curvature will be negative, representing a concave hillslope in the vicinity of the stream that will then become positive when the convex portion of the hillslope is reached.

3.3.3. Cosmogenic nuclides

Sample preparation followed standard procedures (e.g., von Blanckenburg et al., 1996, 2004). Samples, consisting of fine sand to pebbles, were first sieved to 0.5-1 mm size fraction, and magnetic grains were separated using an isodynamic magnetic separator. Treatment in hydrochloric acid, followed by weak hydrofluoric acid, was used to remove oxides, carbonates, and feldspars. We then leached ~ 50 g of the remaining clean quartz for 1 h at 120° C in 7M hydrofluoric acid to remove any remaining meteoric ^{10}Be. Following dissolution in concentrated hydrofluoric acid, 150 to 300 µg of ^{9}Be carrier was added. Beryllium was extracted using column chemistry following von Blanckenburg et al. (2004). The purified beryllium was then mixed with silver, oxidized, and pressed into copper targets. The ^{10}Be/^{9}Be ratio was measured on the AMS at ETH Zurich (Synal et al., 1997).

The measured ^{10}Be/^{9}Be ratios were used to calculate catchment-wide, basin-averaged erosion rates. We used a modification of Dunai's (2000) scaling factors to calculate the production rates for nucleonic and fast and slow muon interactions (Schaller et al., 2002), and a sea-level high latitude production rate of 5.53 atoms g$_{qtz}^{-1}$ yr^{-1} (Kubik and Ivy-Ochs, 2004). Corrections for skyline shielding and snow shielding were also made (Table 1). Modern

average monthly snow depths for Switzerland (Auer, 2003) were compiled and recalculated as average snow depth per year. An average compacted snow density of 0.3 g cm^{-3} was assumed. The resulting reduction in production rate was then determined. If annual snow cover was higher in the early postglacial time, then the resulting reduction in production rates could be much larger (i.e. Schildgen et al., 2005). If this were the case, then our denudation rates may be slightly overestimated. This will have little effect on the geomorphologic interpretation, as the bias will be nearly the same for all samples as they are all in the same geographic region. Skyline shielding was measured using the same LiDAR elevation data as were used for production rates. The inclination to the horizon over 360°, at 5° intervals, is determined for every cell in a drainage basin in order to calculate the degree of cosmic ray shielding provided by surrounding obstructions (Dunne et al., 1999). The resulting snow and topographic shielding factors were applied to the production rate at each cell. A basin-averaged corrected production rate was then calculated. Production rates and absorption laws for erosion rates can be found in Schaller et al. (2002). The post-depositional irradiation age of the terraces, as well as the inherited ^{10}Be concentration of the sediments was calculated using the depth-dependent nuclide production equations of Schaller et al. (2002).

We determined the time of initiation of incision in the Fontanne with a series of mass balance equations. First, the apparent denudation rate for the incised region was calculated from the average nuclide concentrations of the weathering-limited hillslopes and the basins below the knickzones using the equation

$$\varepsilon_{inc} = (A_{tot}*\varepsilon_{tot} - A_{ninc}*\varepsilon_{ninc}) / A_{inc} \qquad 7$$

where ε is the denudation rate, A is surface area available for erosion, *inc* is the incised region, *ninc* is the nonincised region, and *tot* is the total basin. While the rate of incision has surely varied over time, an estimate of the length of time required to incise the canyons can be obtained from the denudation rate in the gorges, ε_{inc}, and volume of material removed;

$$t = V / (A*\varepsilon) \qquad 8$$

where t is the time since the initiation of incision, V is the volume of material removed by downcutting, A is the area over which the incision has occurred, and ε is the denudation rate in the incised region.

3.4. RESULTS

3.4.1. Morphometrics

Although the basins display similar overall relief, the distribution of this relief is quite different. Low elevation valley bottoms are predominant in the Trub, and high elevation surfaces are more common in parts of the Fontanne basin. This difference becomes more pronounced when the hypsometry is considered. All subcatchments in the Trub watershed have similar hypsometries, between 0.43 and 0.48 (Figure 16), where higher hypsometric integrals indicate a larger proportion of high elevations in a basin. The Fontanne subcatchments exhibit much more variability in landscape expression, with hypsometric integrals ranging from 0.36 to 0.56 (Figure 16).

Stream-long profiles and slope area plots (see Figure 14 for locations) vary between catchments (Figure 17). Streams in the Trub basin tend to have smooth concave profiles. Neither the slope-area plots, nor stream profiles indicate knickpoints in the Trub streams (Figure 17C). Some, but not all profiles in the Fontanne catchment display convexities and knickpoints. Stream profiles and slope area plots in the longer southern drainages of the Fontanne display pronounced knickpoints (Figure 17A), while in the shorter northern
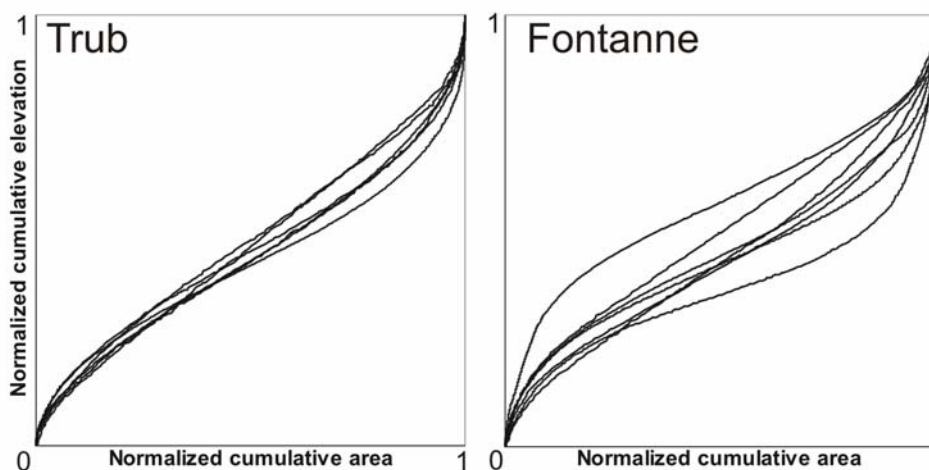
Figure 16. Hypsometric curves, normalized elevation plotted against normalized area, for the streams above sampling points in the Napf. The hypsometry of the major streams in the Trub basin (left) is much more homogeneous than those of the Fontanne (right). Variations in the distance of knickpoint migration are responsible for the increased variability of the hypsometry in the Fontanne.
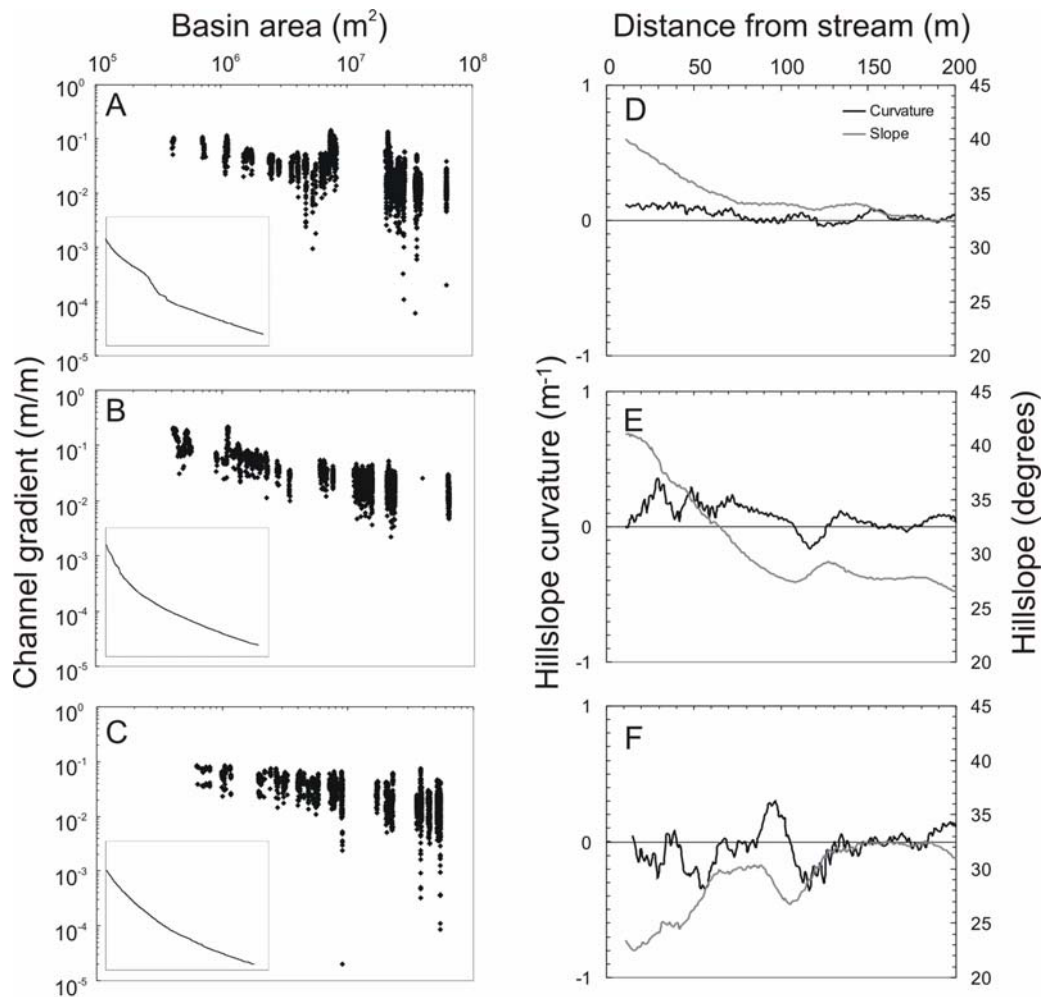
Figure 17. Representative slope area plots, longitudinal stream profiles (inset plots), and curvature plots for three differing valley types in the study area. The knickzone is easily identifiable on the longitudinal profile and slope area plot for Fon7 (A and D), a currently incising valley. The knickpoint is no longer visible in Fon2 (B and E) because it has already migrated into the headwater basins. The disturbance, however, is still identifiable in the slope area and curvature plots. Morphometrics of Trub5 (C and F), represent nonrejuvenated basins. The basins of the Trub, as well as the basins above the knickzones in the Fontanne, have smooth long profiles and overall negative curvatures. (Note: The first 10 m of the slope and curvature plots are not included, as boundary effects caused spurious results.)

tributaries the knickpoints have already passed (Figure 17B). Knickpoints are easily recognizable in the southern subcatchments, while the northern subcatchments have no prominent knickpoints, but are occasionally oversteepened.

The curvature and slope diagrams further show the degree to which these adjacent basins differ. Stream proximal curvature for the Trub streams is mainly negative (Figure 17F), while the upper basins of both watersheds exhibit ~ 0 m^{-1} curvature. In the Fontanne, stream segments above the knickpoints show the same pattern as streams in the Trub, with concave hillslopes. Below the knickzones, the curvature depends on the upstream distance of
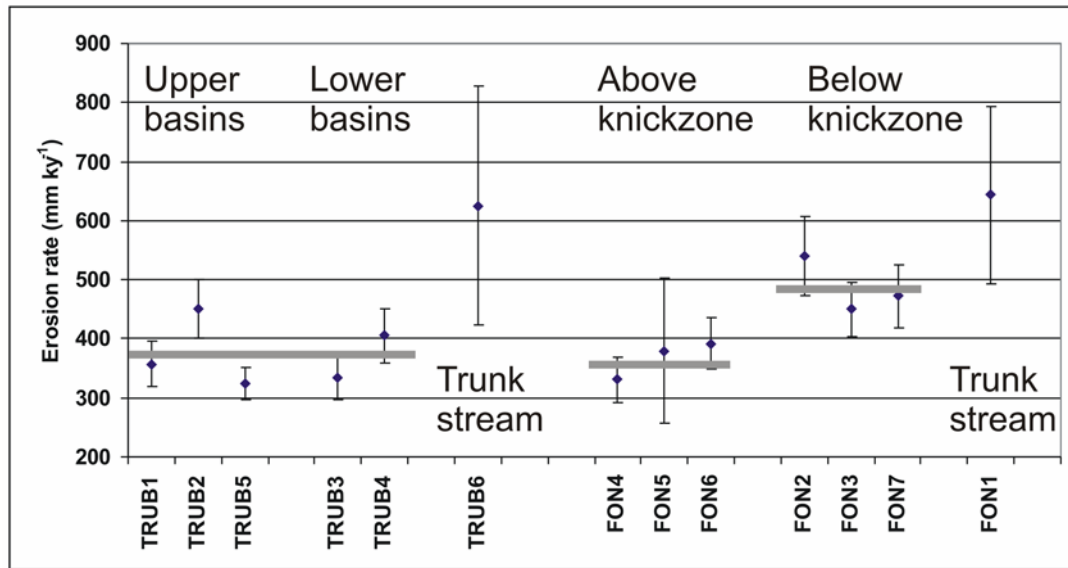
Figure 18. Denudation rates in the Napf. A measurable difference exists for the erosion rates calculated from samples above the knickpoint (Fon4, Fon5, and Fon6) and those below the knickpoint (Fon2, Fon3, and Fon7). Denudation rates are equivalent between upper basins (Trub1, Trub2, and Trub5) and the larger catchments (Trub3 and Trub4) in the Trub watershed. Elevated denudation rates of the trunk stream samples (Fon1 and Trub6) appear to be due to incorporation of low-concentration material in the form of the incised inner gorges and deep terrace material, respectively.

the knickzone. For subcatchments that are currently being incised, i.e., the knickzone is in the catchment, the curvature is near 0 m^{-1} and the slope is high (Figure 17D). If the knickzone has already migrated through the basin though, the curvature is larger and positive while slope remains high (Figure 17E).

3.4.2. Cosmogenic nuclides

The denudation rates calculated for the three upper basins in the Trub are equivalent to those for the two measured in the Fontanne, $380 \pm 50 \text{ mm ky}^{-1}$ (Figure 14; Figure 18; Table 3). Within the Trub, upper basins and two downstream samples also have similar denudation rates, $350 \pm 50 \text{ mm ky}^{-1}$. The same is true for the Fontanne, where the two upper basins average $390 \pm 10 \text{ mm ky}^{-1}$ and sample Fon4, which is located upstream of the knickzone, erodes at $410 \pm 50 \text{ mm ky}^{-1}$. In the Fontanne, however, a small but measurable difference exists between three samples that were taken upstream and three downstream of the knickpoints. Upstream denudation rates are $370 \pm 30 \text{ mm ky}^{-1}$, while downstream rates are $490 \pm 71 \text{ mm ky}^{-1}$. Trunk stream samples in both the Trub and the Fontanne yield rates that are higher than the other samples, $630 \pm 200 \text{ mm ky}^{-1}$ and $640 \pm 150 \text{ mm ky}^{-1}$, respectively. The terrace depth samples in the Trub catchment decrease in nuclide concentration with
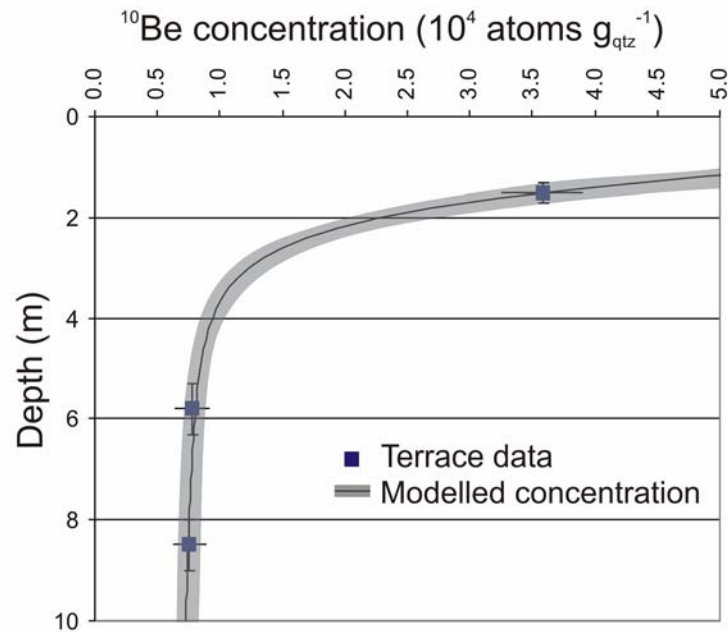
Figure 19. Plot of the ^{10}Be concentration vs. depth for the Trub terraces. The solid black line is the best fit model based on the depth correction equations of Schaller et al. (2002), using an age of 17 ka and 6000 atoms g_{qtz}^{-1} inheritance (i.e., the concentration of ^{10}Be in the terrace sediment at the time of deposition). The 1-sigma error of the of the terrace samples can also be fit using ages ranging from 14 ka to 21 ka and inheritance values from 5000 to 7000 atoms g_{qtz}^{-1} (grey area).

depth (Figure 19). Modeling of the depth profile yields ages ranging from 14 ka to 21ka for the age of the terraces, and inheritance of between 5000 and 7000 atoms g_{qtz}^{-1}. The data are best fit with an age of 17 ka and 6000 atoms g_{qtz}^{-1} inheritance, which equates to a paleodenudation rate of $\sim$ 1700 $\pm$300mm ky^{-1}. It is worth noting that while there is considerable spread in the possible age of the terraces, all modeled ages postdate the retreat of the LGM glaciers from the foreland. Furthermore, the inheritance is better constrained than the terrace age, allowing a high degree of confidence in the paleodenudation rate.

Mass balance calculations (equation 7) for the Fontanne watershed yield incision rates in the inner gorges as high as 1800 mm ky^{-1}. The initial age of incision, assuming that the inner gorges have been eroding at 1800 mm ky^{-1}, is 16 $\pm$3 ka (equation 8).

3.5. DISCUSSION

3.5.1. Landscape evolution

The present terrace fill and subsequent cutting in the Trub occurred at 17 $\pm$3ka and could be related to the retreat of LGM glaciers to the central Alps after 21 ka (Ivy-Ochs et al., 2004). Müller and Schlüchter (1997) suggested that terrace fill is due to the formation of a

proglacial lake to the north, based on the interfingering of reworked terrace gravels with glaciolacustrine clays downstream of the study area. Ice advance into the foreland caused glacial damming and a rerouting of stream courses (Figure 11). To the NW, the damming caused the formation of a proglacial lake (Müller and Schlüchter, 1997) that would have resulted in a rise in the base level of the Trub and the deposition of gravel valley fill. Upon glacial retreat, the dam removal would lead to a return of the Trub to preglacial base level, and cutting into the terrace fill. An alternative hypothesis is needed if the terrace age is post-LGM. If this is the case, the valley fill could be the result of periglacial weathering and that created large quantities of sediment on the hillslopes of the Napf. Paleodenudation rates, based on buried terrace sediments, following the LGM were ~4x higher than those found in the region today (i.e., 1300 mm ky^{-1} vs. 400 mm ky^{-1}). These increased process rates would have delivered more sediment to the Trub than the stream could transport, leading to the filling of the valley. After the hillslopes were cleared of sediment, the rate of delivery of sediment to the steam would decrease, causing contraction and incision by the stream.

The current increase in erosion rates in the Fontanne are caused by incision of the stream in response to a base level lowering at 16 ±3ka. The morphology of the Kleine Emme in this region (see Figure 10) indicates that stream piracy has affected this basin. The lower Kleine Emme outlet was blocked by ice during the LGM, causing a rerouting of the water of the Fontanne into the Seewegtal. This may have resulted in the deposition of terrace fill in the Fontanne as well, but no record of this has been located. The resulting drop in base level following deglaciation, caused by a switch to the Kleine Emme drainage network, initiated a wave of incision in the Fontanne. Incised valleys are prevalent throughout the Fontanne catchment.

3.5.2. Soil production

The background denudation rate for the Napf, taken as the average of the upper basin denudation rates (380±50 mm ky^{-1}), agrees well with potential rates of modern base level lowering in the Swiss Foreland, 300 mm ky^{-1} as assumed from geodetic uplift rates relative to the Aarburg benchmark (Schlatter et al., 2005). These rates are also within the range, 110 to 480 mm ky^{-1}, of a coarse-spatial resolution denudation survey of catchments in the Mittelland (Wittmann et al., in press). The rates in the Trub are equivalent at various scales, as are the denudation rates in the headwater basins of the Trub and the Fontanne. Because of this, the average denudation rate, 380±50 mm ky^{-1}, can be assumed to be the hillslope sediment

production rate, where the sediment production rate is the rate at which bedrock can be converted into regolith. This rate is higher than the estimates for the rate of regolith production in a variety of climates (Rosenbloom and Anderson, 1994; Small et al., 1999; Heimsath et al., 2001). This is because the cobble conglomerates of the Napf allow for faster regolith production. In granitic terrains (e.g., Heimsath et al., 2001), sediment production typically requires the weathering of a noticeable fraction of the bedrock before regolith is released to the hillslope. For the Napf conglomerates, only the moderately cemented, carbonate rich intergranular matrix must be weathered before cobbles are freed. Therefore, regolith production rates on this particular lithology may be higher than previous estimates.

3.5.3. Incision and disequilibrium

The differing responses in the Trub and the Fontanne are due to the magnitude of the base level fluctuation. In the Trub, spillover of the proglacial lake into the Önztal (Figure 11) controlled the elevation of the lake and reduced the difference in base level to ~ 20 m. This base level change could be rapidly accommodated by eroding the valley fill (Pratt-Sitaula et al., 2004). The low physical resistance of this material also means that knickpoints were most likely not sustainable, and downcutting occurred along the stream as a coupled hillslope-channel system. The formation of terraces also created a buffer for the Trub. The low variability of hypsometry in the Trub catchments supports this interpretation. Bedrock incision by the stream, then, did not occur because the system is buffered by the gravel fill.

Following the base level drop, decoupling of the hillslope-channel system (Furbish and Fagherazzi, 2001) allowed the creation of a transient state in the Fontanne basin in which the overall sediment flux is higher than the rate of sediment production on the hillslope (Braun et al., 2001) from channel incision. Because the hillslopes in this area are weathering-limited, the increased stream power could not be balanced by an increase in sediment load, leading to bedrock incision. In such a system, increased erosion rates should lead to a change in the style of denudation in the basin from one dominated by sediment movement to one in which larger scale mass wasting occurs. Where increased erosion rates do occur (i.e., beneath the knickzone), hillslopes above the incised gorges have become destabilized due to oversteepening, and patches of bedrock can be seen (Schlunegger and Schneider, 2005). Base level drop in the Fontanne catchment was controlled by the 80-m difference in elevation between the Kleine Emme and Seewegtal levels. This magnitude of base level fall was not able to be buffered as occurred in the Trub basin, as little to no fill was present in the system.

Rapid decoupling then occurred, as low relief surfaces were incised by the knickzones. Their propagation rate can be calculated to be more than 0.6 m yr^{-1}, based on a distance of ~ 10 km of knickpoint migration over a period of 16 kyr. The knickpoints have migrated different distances up the different tributaries of the Fontanne, with the result that this watershed has extremely variable hypsometry compared to that of the neighboring Trub basin. The rate, despite being quite rapid, is significantly slower than knickzone migration of as much as 3 m yr^{-1} in similar environments in the western Alps (Brocard et al., 2003). Decoupling further suggests that the channel response time for the Fontanne is significantly longer than for the Trub, at least > 16 kyr. These estimates are in good accordance with the Brocard et al. (2003) estimate of ~ 20 kyr response times for basins in the western Alps.

The high trunk stream denudation rates in both basins are related to the incorporation of low-concentration sediment. Undercutting of the terrace fill in the lower reaches of the Trub watershed causes occasional mass wasting events which then mix the deeply buried terrace material with that from the upper basins. Likewise, incision below the knickzones in the Fontanne catchments brings low concentration sediment into the stream system, causing higher apparent denudation rates.

3.6. CONCLUSIONS

Climate change during the transition from the last glacial to interglacial period, acting on older gravels stripped from the Alpine core have produced an environment in the Swiss Mittelland in which transient basin response to climate and base level change can be quantified. Two adjacent watersheds, the Trub and the Fontanne, exhibit differing geomorphic response to the perturbations. In the Trub basin, the 20-m drop in base level was buffered by the fill, and the system quickly returned to a quasi-equilibrium state. Hillslope-channel decoupling occurred in the Fontanne basin from a greater magnitude change in base level, 80 m, which, based on a mass balance model, occurred at the end of the LGM. The slower response time of this catchment has resulted in the presence of knickzones that are migrating upstream at about 3 m yr^{-1}. Sediment production rates of 0.38 m ky^{-1} in this region, because of the easily disaggregated Miocene conglomerate bedrock that underlies both basins, are among the highest yet to be reported.

Table 3. ^{10}Be Cosmogenic-nuclide derived denudation rates. Samples Trub6s, Trub6m, and Trub6l are grain-size fractions of 0.25-0.5 mm, 0.5-1 mm, and 1-2 mm, respectively, taken from the same sample. In the Napf, grain size effects do not seem to be important.

Catchment	Sample	Area (km²)	Depth (cm)	Mean Altitude (m)	Latitude (dd)	Longitude (dd)	Shielding Factor	Snow Correction	Production Rate (atoms g qtz-1) *104	^{10}Be Conc. (atoms g qtz-1) *10⁴	Denudation rate (mm ky-1)	App. Age (y)
Trub	Trub1	1.7	-	998	46.9958	7.8926	0.951	0.986	13.59	2.94±0.31	357±38	2160
	Trub2	1.6	-	997	46.9913	7.8846	0.945	0.987	13.51	2.32±0.26	451±50	1720
	Trub3	9.9	-	872	46.9675	7.8930	0.961	0.987	12.88	3.01±0.33	334±37	2340
	Trub4	4.9	-	954	46.9752	7.9118	0.956	0.984	13.29	2.54±0.29	405±46	1920
	Trub5	1.4	-	1021	47.0025	7.9192	0.955	0.985	13.62	3.25±0.27	324±27	2390
	Trub6	38.1	-	809	46.9475	7.8882	0.966	0.986	12.61	1.59±0.51	630±200	1300
	TrubT1	-	150	884	46.9671	7.8914	-	-	12.88*	3.58±0.33	280±25	2780
	TrubT2	-	580	880	46.9669	7.8908	-	-	12.88*	0.78±0.14	1299±230	600
	TrubT3	-	850	878	46.9667	7.8916	-	-	12.88*	0.76±0.13	1330±230	590
Fontanne	Fon1	62.1	-	605	47.0308	8.0608	0.961	0.990	11.10	1.38±0.32	643±149	1200
	Fon2	4.8	-	657	47.0379	8.0337	0.968	0.992	11.05	1.64±0.20	540±67	1490
	Fon3	3.4	-	778	47.0310	7.9827	0.961	0.988	11.82	2.08±0.22	450±46	1760
	Fon4	4.8	-	859	46.9727	7.9861	0.967	0.984	12.35	2.93±0.33	331±38	2370
	Fon5	2.4	-	913	46.9712	7.9660	0.958	0.984	12.59	2.59±0.85	380±120	2100
	Fon6§	2.2	-	896	46.9883	7.9708	0.961	0.983	12.79	-	390±40	2000
	Fon7	11.9	-	779	46.9836	8.0022	0.952	0.985	12.17	2.03±0.23	472±53	1670
	Fon6s	2.2	-	896	46.9883	7.9708	0.961	0.983	12.79	2.85±0.31	351±37	2230
	Fon6m	2.2	-	896	46.9883	7.9708	0.961	0.983	12.79	2.32±0.26	430±48	1820
	Fon6l	2.2	-	896	46.9883	7.9708	0.961	0.983	12.79	2.53±0.28	395±44	1980

[a] Shielding factor is a catchment wide skyline shielding correction factor.
[b] Snow factor is a correction employed for snow shielding.
[c] ^{10}Be concentration with 1σ analytical error, using a 15 ky initial age.
[d] Denudation rates calculated using the production rates and absorption coefficients of Schaller et al. (2002) and the scaling laws of Dunai (2000).
[e] Apparent age corresponds to the length of time required to erode ~70 cm of material.

CHAPTER 4. COMPETITION BETWEEN DIFFUSIVE AND STOCHASTIC GEOMORPHIC PROCESSES IN THE GLACIALLY SCULPTED UPPER RHONE VALLEY, SWITZERLAND

ABSTRACT

We have found that the competition between slow soil creep background erosion and rapid mass wasting by debris flows and rock falls exerts the primary control on denudation rates in the upper Rhone Valley. Within a very small distance (10's of km) denudation rates of small tributary valleys vary by more than an order of magnitude. Basins which have been previously minimally glacially modified have lower denudation rates, 61-560 mm kyr^{-1} than those steep valleys in which glacial erosion up to the Younger Dryas was high and scarps were either removed or minimal, 760-2100 mm kyr^{-1}. Background denudation rates calculated from amalgamated soil samples average 60 mm kyr^{-1}. Sediment storage and regrading of hillslopes proximal to valley-longitudinal scarps, typical for this region, has lead to reduced sediment transport rates, and created contrasting denudation rates between the valleys. Transport in glacially scoured valleys is characterized by rapid debris flow processes, while creep on soil-mantled slopes dominates in the fault influenced basins. The resulting implication is that in this region, it is not glaciers themselves that result in high erosion rates in the Holocene, but the delayed impact of Pleistocene glacial landscape change on sediment transport processes.

4.1. INTRODUCTION

Ahnert (1970) put forward a seminal model relating hillslope gradient to sediment transport rate (e.g. erosion) using a linear equation. Roering et al. (1999) recognized that while this linear relationship holds for low gradients, at higher slopes erosion rates become unrelated to hillslope gradients. A threshold hillslope gradient is defined, analogous to the angle of repose for unconsolidated material, above which failure will occur. In such a case, soil-mantled slopes above the hillslope threshold are not possible. This concept was modified

by Montgomery and Brandon (2001) who suggested this threshold to be the point at which hillslope creep processes give way to landsliding and debris flows. In this case, the erosion rate is governed by rock uplift rates, regardless of hillslope gradient. Many mountain belts feature steep slopes in the Holocene for an entirely different reason. Glaciers, over multiple glaciations, have sculpted over-steepened valleys and left shallow ridge tops. Even if glacial erosion was not necessarily high in the last cold cycle, previous glaciations created a landscape that is so out of equilibrium that Holocene fluvial processes incise to a degree that steep slopes emerge. A landscape with a multitude of erosional processes results and the lower limit of basin-averaged denudation rates is equal to the rate resulting from diffusive hillslope creep, while the maximum theoretical rate is equal to the rate produced by landslides and debris flows. The large difference in transport rates between these geomorphic processes should translate into different denudation rates for basins in which the relative importance of creep versus landsliding varies. The Alps are a perfect example for such a transient landscape. Here we use a combination of basin-averaged and amalgamated soil denudation rates in the context of hillslope morphology and sediment transport rates to quantify these process rates in the Central Swiss Alps over various spatial scales. We show that denudation rates vary by an order of magnitude, and that stochastic processes of mass wasting outweigh hillslope diffusion where glaciers have shaped particularly steep valleys.

4.2. SETTING

The Upper Rhone Valley, Goms (Figure 1), located in the Central Swiss Alps between Furka Pass and the town of Fiesch, is subject to some of the highest rates of rock uplift in the Swiss Alps relative to a benchmark in the Swiss foreland (Kahle et al., 1997; Schlatter et al., 2005). Wittmann et al. (2007) showed that denudation rates for the Alps are strongly correlated with rock uplift rates, suggesting that in the Goms, where uplift rates range between 0.7 and 1.3 mm ky^{-1}, denudation rates on the order of 0.8-1.4 mm yr^{-1} would be expected. However, the upper Rhone valley lacks any evidence for active processes of base level lowering. Hence the process that is relating rock uplift and denudation must be one of long-term stability, where erosion is being driven by processes other than base level lowering. During the LGM, the upper Rhone Valley was filled with at least 1500 meters of
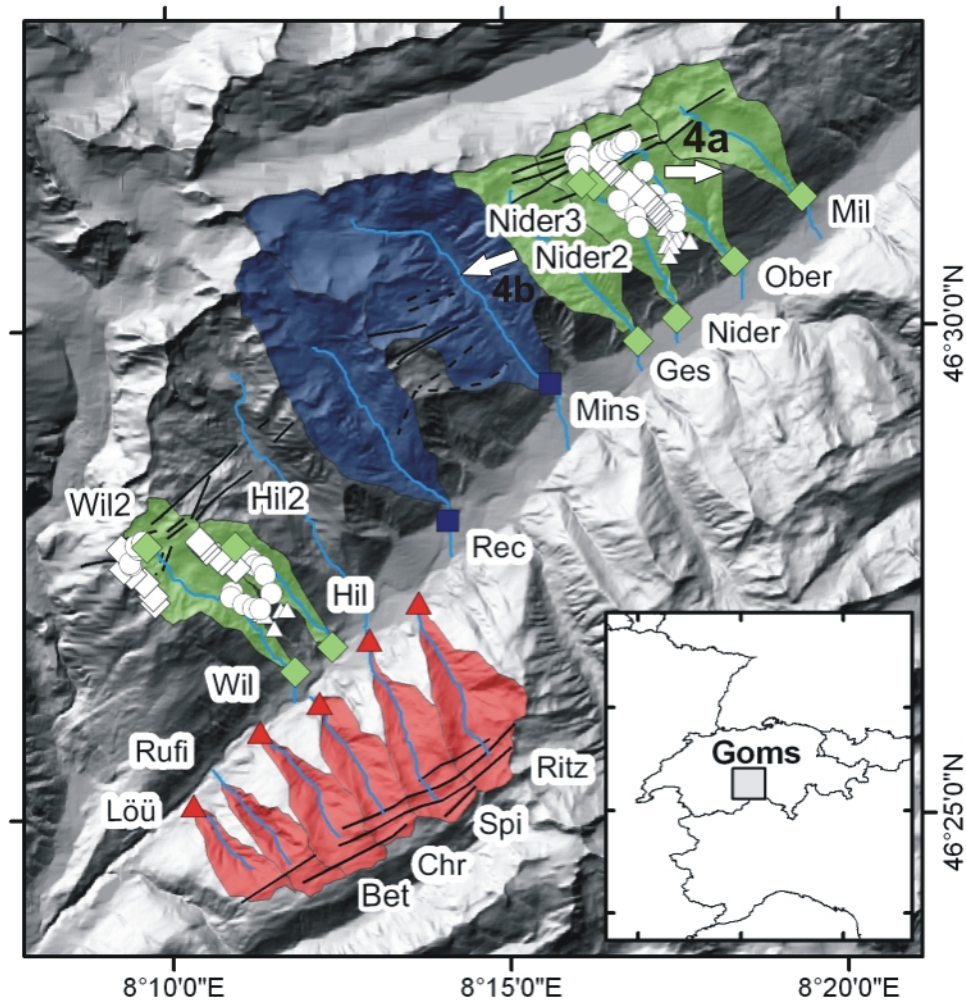
Figure 20. Location map showing stream sample locations (glacially scoured basins in blue with squares, non-scoured basins in green with diamonds and southern basins in red with triangles), and faults in black. Soil sample locations are shown in white (ridge top with a diamond, valley side with a star, interfluvial surfaces with a triangle). Photo locations for Figure 4 are marked with a white arrow.

ice (Jäckli, 1970; Florineth and Schlüchter, 1998; Kelly et al., 2004). Through repeated Pleistocene glaciations, this large glacial system helped form the wide U-shaped valley known as Goms. Retreat of the Rhone glacier before 18 kyr BP (Kelly et al., 2006) left behind hanging upper valleys and glacial meltwater-incised side valleys. The valleys are separated by broad soil-mantled ridges. At lower elevations, triangular interfluvial surfaces are found between the streams (Figure 21a). Some of the side valleys were covered by glaciers, possibly lasting into the Younger Dryas. Where these glaciers were large, the valleys have been deeply scoured, with wide valley bottoms, steep walls, and U-shaped cross-sections (Figure 21c). The 3 scoured valleys, the Mins, Rec, and a non-sampled valley in Figure 1, are still host to small modern glaciers between 0.5 and 3 km^2 in size. In all other side valleys, small or non- erosive Pleistocene glaciers lead to unscoured main valleys with
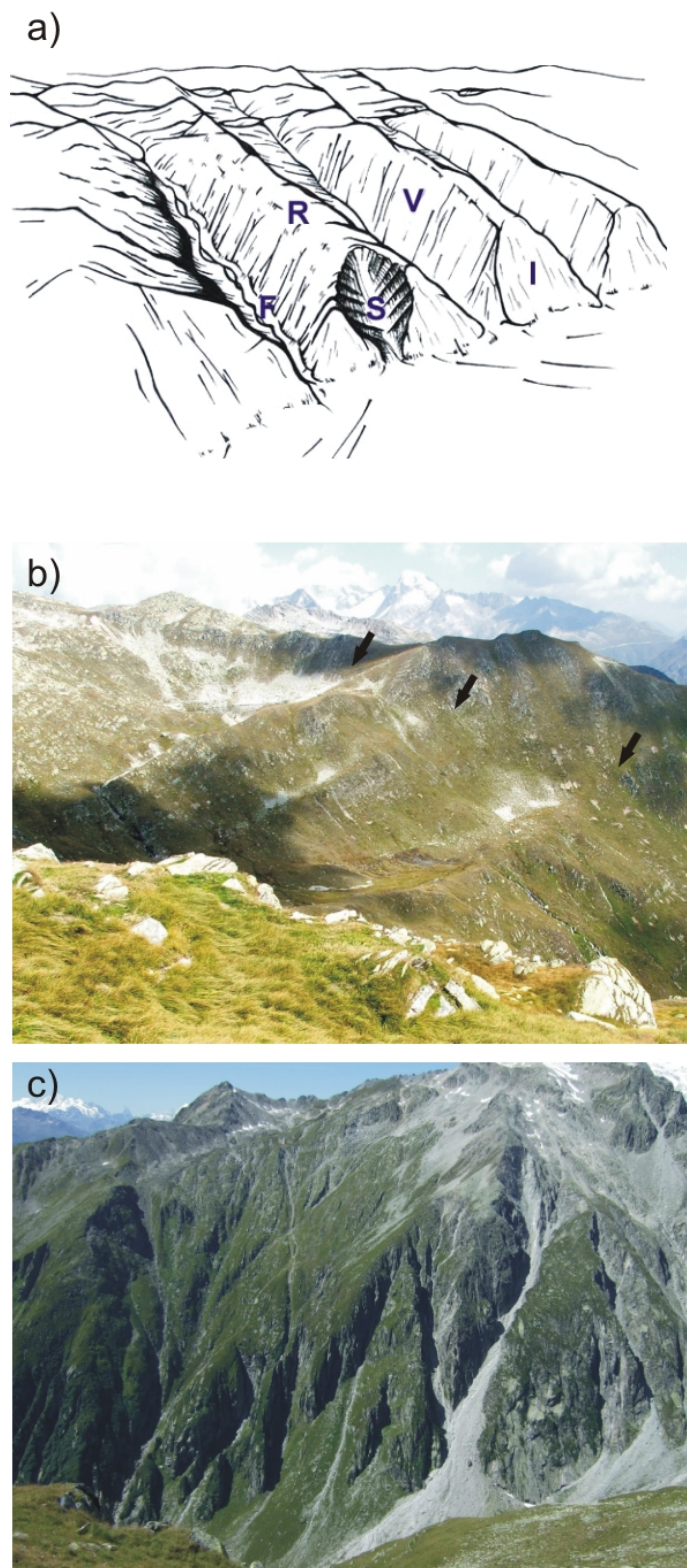
Figure 21. a) Schematic diagram of the lateral valleys of the Goms, showing; ridges (R), valleys (V), interfluvial surfaces (I), colluvial fans (F), and large scale failure scars (S). b) The upper sections of the Oberbach basin, where valley-side-up scarps are indicated by arrows. c) In the Minsterbach, where glaciers have excavated the faults, the steep valley sides promote debris flows.

cirque basins and incised lower reaches (Figure 21b). Upon the retreat of the Rhone glacier, stress gradients caused the creation of gravitational faults and reactivation of previously active faults or shear zones (Ustaszewski and Pfiffner, in press). As reported by Ustaszewski and Pfiffner. (in press) and Persaud and Pfiffner (2004), such post-glacial surface ruptures are common features throughout the Swiss Alps. These post-glacial scarps are valley-side-up. Faults scarps in non-scoured basins are continuous from the ridge tops across the valley bottoms. In the case of glacially scoured basins, the composite fault scarps are only present on the ridge tops and valley sides, disappearing in the valley bottoms. This landform assemblage leads to the surmise that the scarps were either eroded by the glaciers, or their formation was suppressed by overlying ice. In the southern valleys feeding the Goms main valley, the faults strike more southerly than the main ridge resulting in more scarps affecting larger basin areas in the southeastern valleys than in the southwestern.

4.3. METHODS

We measured a total of 30 in situ-produced cosmogenic ^{10}Be derived denudation rates on stream sediments and soils in the upper Rhone Valley. 17 stream sediment samples, of ~5 kg each, were collected from 15 drainage basins in the Goms (Figure 20). Stream samples came from two main settings, glacially scoured valleys with U-shaped cross-sections (Rec, Mins), and fluvially dominated valleys lacking evidence of extensive glacial scouring. These samples are subdivided into those entering the Rhone from the north (Wil, Hil, Ges, Nider, Ober, Mil) and from the south (Ritz, Spi, Chr, Bet, Rufi, Lou). While the non-scoured northern basins, with the exception of Hilpersbach, are all affected by valley-side-up faults, a gradient in the southern section is apparent, with fault scarp density decreasing towards the west (Figure 20). In 3 valleys, stream sediment was also sampled in the upper part of the basins (Wil2, Hil2, Nider2, Nider3). Three main geomorphic surfaces were selected for soil sampling; ridges, valley sides, and interfluvial surfaces (Figure 21a). In order to capture the maximum variability of each region, we adopted a semi-random sampling scheme (e.g. Riebe et al, 2004). A total of 65 soil samples of ~ 0.5 kg each were combined based on geomorphic location into 10 different amalgamated samples of between 4 and 12 individual samples, O-R, O-Rg, O-V, O-I, N-V, N-Vg, H-R, H-I, W-R, and W-I (where the first letter refers to the drainage basin name; O for Oberbach, N for Niderbach, H for Hilpersbach, and W for

Wilerbach, and the second to the geomorphic domain; R for ridge, V for valley, and I for interfluve. The postscript "g" is included for granite parent rock; all other soils are developed on gneissic rocks.

Denudation rates of stream sediments were calculated from ^{10}Be/^{9}Be ratios measured at the AMS at ETH Zürich (Synal et al., 1997). Because this landscape was covered with thick, erosive ice up to 15 kyr BP (Kelly et al., 2006), and some of our denudation rates are low, steady state with respect to cosmogenic nuclides can not necessarily be assumed. Therefore, the concentration of cosmogenic nuclides, N, is governed by both the denudation rate, ε, and the initial exposure age, t (Lal, 1991):

$$N(x,t) = \frac{P(0)}{\lambda + \frac{\rho\varepsilon}{\Lambda}} \times \left(1 - e^{-\left(\lambda + \frac{\rho\varepsilon}{\Lambda}\right)t} \right) \qquad\qquad 9$$

where, P(0) and Λ are the summed production rate and absorption mean free path for nucleons, fast and stopped muons described in Schaller et al. (2002), ρ is rock density, and λ is the half-life. Scaling followed the latitude and altitude scaling laws of Dunai (2000). Topographic shielding factors were calculated on a pixel-by-pixel basis from 30m SRTM data (Norton and Vanacker, in press) Snow shielding factors were calculated using an altitude dependant snow depth and duration function derived from the monthly Swiss snow depth maps of Auer (2003). Amalgamated soil sample denudation rates were calculated in the same way with the difference that shielding factors and production rates were calculated for each sampling point and averaged.

4.4. RESULTS

^{10}Be-derived basin-averaged denudation rates in the lateral valleys of the upper Rhone basin vary from 61 to 2100 mm ky^{-1} (Table 4). To the north of the Rhone, the highest rates are found in scoured basins with modern glaciers and no scarps in the valley bottoms, while the lowest are found in those valleys in which faulting is prevalent (Figure 22). In the southern valleys, where there is no evidence of Holocene glacial cover, a gradient in

denudation rates from 240-1400 mm ky^{-1} was nevertheless measured. For the valleys in which upper-basin samples were also taken (Nider2, Nider3, Wil2, Hil2), the rates are always similar to those measured near the confluence with the Rhone (Table 4). Denudation rates calculated from amalgamated soil samples are quite homogeneous, with rates varying from 22-100 mm ky^{-1}.

4.5. DISCUSSION

Hillslope denudation rates measured in the non-scoured basins of Goms are quite uniform and low compared to basin-averaged rates from similar environments in the Central Alps (Wittmann et al., 2007). The mean basin-averaged denudation rate is 240 mm ky^{-1} from stream sediment in the non-scoured valleys. A comparison of soil denudation rates and basin-averaged denudation rates reveal non-uniform erosional response. Basin-averaged denudation rates from river sediments draining non-scoured valleys are 2.8 times those of
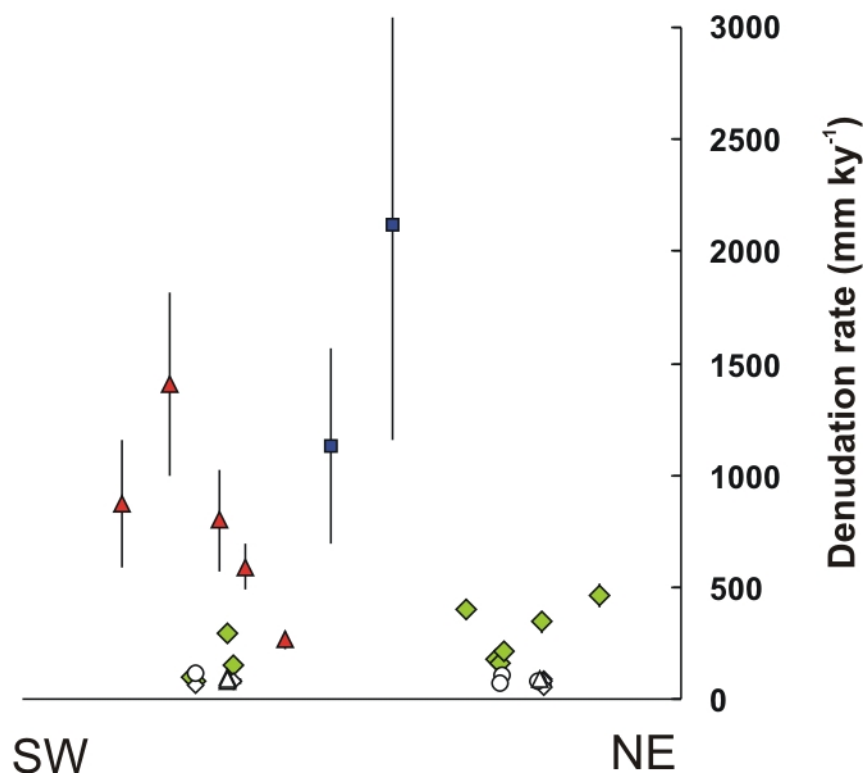
Figure 22. Basin-averaged denudation rates for the Goms watersheds. X-axis is the SW-NE location of the valleys along the Rhone River. Glacially scoured basins (blue squares) to the north of the Rhone have considerably higher denudation rates than non-scoured basins (green diamonds). To the south of the Rhone (red triangles), denudation rates increase towards the southwest. Amalgamated soil samples (open symbols match those in Figure 20) are consistently low.

amalgamated soil denudation rate values. We suggest that this is due to the competition between the two dominant modes of sediment transport that are common in the upper Rhone Valley. Basins with extensive soil mantling are dominated by diffusive creep, while stochastic processes (rock falls, landslides, and debris flows) are prevalent where soils are lacking. The soil denudation data provide an average rate of 86 mm ky^{-1}. Based on field mapping and aerial imagery, the percentage of soil-covered slopes in the non-scoured valleys is estimated to be 90%. Using the amalgamated soil denudation rates as the rate of hillslope creep together with the total basin averaged denudation rates, a mass balance equation can be used to estimate the importance of rapid, stochastic, transport processes (i.e. rock falls, debris flows, etc.) on the entire system. While they account for only 10% of the landscape, bare rock regions account for over half of the total denudation in the non-scoured basins and are denuding at high rates, ~1400 mm ky^{-1}. This value becomes even larger when the same analysis is applied to the glacially scoured basins. In these valleys, where debris flows are most prevalent, an upper denudation end member rate of up to 7000 mm ky^{-1} is inferred.

Despite the uniformity of their denudation rates, some geomorphic information can be gleaned from the amalgamated soils. The landforms with the lowest hillslope gradients, the ridges at 23°, also have the lowest average denudation rates, ~45+/-4 mm ky^{-1}, while the valley slopes, 26°, have higher average denudation rates, ~74+/-7 mm ky^{-1}, and the interfluvial samples at the steepest angle, 34°, denude at intermediate rates of 64+/-5 mm ky^{-1}. Our data show that in the Goms, while a threshold angle does appear to exist based on basin-averaged denudation rates, soil-mantled slopes can be maintained well above the basin threshold gradient (Figure 22). Where valley side-up scarps are intact and glacial scouring is minimal, hillslopes are shallower, especially in the upper parts of the basins (Table 4). That the interfluvial surfaces have lower denudation rates than the valley hillslopes despite higher gradients is contradictory to theory (Ahnert, 1970; Montgomery, 2001; Montgomery and Brandon, 2002). This is most likely due to forest cover which is common at these lower elevations, but is absent in the higher valley slopes. The presence of deeper rooting vegetation might also explain how these steep terrains are able to sustain soil cover over such long averaging times, 5-11 kyr. These interfluvial facets are, however, prone to large-scale deep seated failure as is evidenced by the presence of large landslide-debris flow scars on some of the interfluves (Figure 21a).

The large variation in denudation rates between the lateral valleys in the Goms is not a response to rock uplift, as geomorphic baselevel is not decreasing, but must have some

other driving force. We suggest the variations are dependant on the spatial distribution of soil cover, which in turn is related to the local sediment transport regime. This is due in part to a unique form of faulting, with the valley-side-up, leading to a situation in which the presence of scarps creates accommodation space, slowing down the sediment cascade. The slower sediment transport rates translate into reduced denudation, which is important because the lower slope angles support a system dominated by creep processes. In the valleys in which the faults were removed by glacial action, hillslopes adjacent to the channels have much higher relief. Other studies (Montgomery and Brandon, 2002; Binnie et al., 2007) have suggested that once these hillslopes pass beyond the threshold gradient for hillslope creep, then the system will switch to one in which landsliding and debris flows prevail. Indeed, in the glaciated basins, the fault region erodes through debris flow action. On hillslopes between the channels of the scoured valleys, creep is still the main process (Figure 21b), but the relative contribution of creep to the sum of all erosion processes is much lower than that of the unscoured valleys.
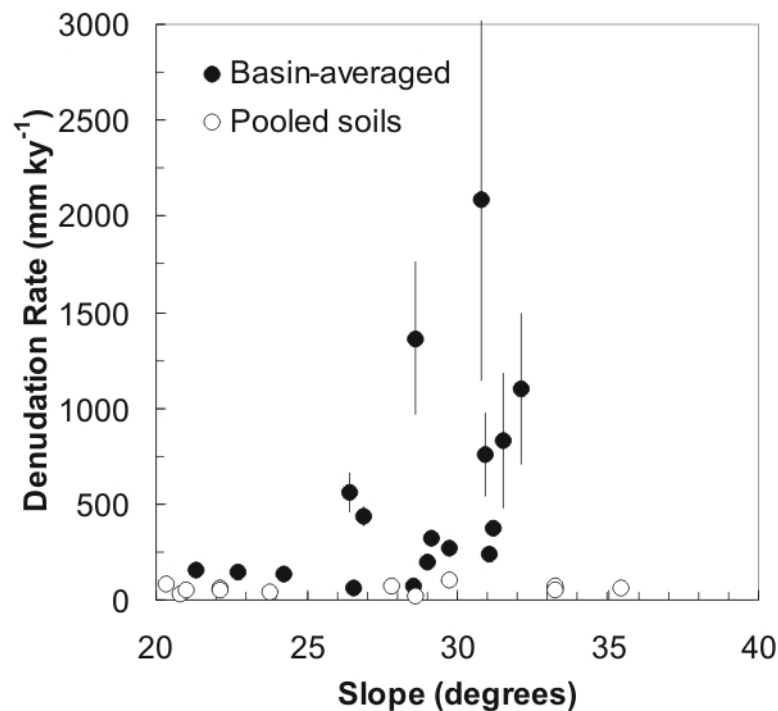
Figure 23. Denudation rates plotted against mean elevation for both basin-averaged sediment samples (filled circles) and amalgamated soil samples (open circles). Basin-averaged denudation rates are limited at threshold hillslope angles, with rates increasing dramatically above ~25°. Amalgamated soil samples show no correlation with hillslope gradients, remaining between ~80 and 150 mm ky^{-1} regardless of slope.

4.5. CONCLUSIONS

Therefore, we conclude that it is the pre-conditioning by glacial erosion, not glacial erosion itself that dictates the pace of erosion processes in the Holocene. While all soil-mantled hillslopes denude at a "background" denudation rate of 22-100 mm ky^{-1}, debris flow and rock fall overwhelm the erosional system where the conditions prevail for these types of mass wasting. This is the case in the glacially-scoured valleys and in those valleys of the southern flank where valley-side-up fault scarps are absent. Where these faults do occur, they aid in keeping the soil cover in place, resulting in lower valley-scale denudation rates.

It is worth noting that an area- and flux-weighted denudation rate for all the tributaries studied here results in a denudation rate of 1.4 mm ky^{-1} for the entire upper Goms valley. This rate is similar to large-catchment rates in this part of the Central Alps (Wittmann et al., 2007) and also with the range of geodetic rock uplift rates (Kahle et al., 1997; Schlatter et al., 2005). We observe that differential, competitive erosional processes in the upper Rhone valley are setting the pace of denudation. This is in the absence of possible uplift-driven base level lowering in the form of bedrock incision in the Rhone trunk stream, lending support to the hypothesis that it is denudation that may be setting the pace of rock uplift in the Alps.

Table 1. ^{10}Be-derived denudation rates

	Sample	Longitude	Latitude	Area	Slope	Altitude	10Be conc.[a]	Error	Shielding factor[b]	Snow factor[c]	Denudation rate (15kyr)[d]	Error
		(dd)	(dd)	(10^{-4} km^2)	(degrees)	(m)	(10^4 atoms g$_{qtz}^{-1}$)				(mm ky^{-1})	
Streams	Mil	8.3230	46.5223	4.1	27	2355	4.14	0.44	0.95	0.84	439	52
	Ober	8.3061	46.5115	3.6	29	2302	5.44	0.69	0.95	0.84	321	46
	Nider1	8.2692	46.5246	0.9	21	2687	13.42	1.27	0.97	0.81	159	17
	Nider2	8.2723	46.5243	1.09	23	2686	14.59	0.99	0.97	0.81	145	11
	Nider3	8.2921	46.5011	2.9	29	2312	8.63	0.96	0.94	0.84	199	25
	Ges	8.2814	46.4994	9.5	31	2335	4.67	0.47	0.94	0.83	377	41
	Mins	8.2608	46.4908	14.6	31	2492	0.74	0.19	0.92	0.62	2080	940
	Rec	8.2392	46.4681	12.2	32	2517	1.58	0.39	0.92	0.70	1100	390
	Hil	8.2081	46.4477	1.6	30	2142	5.78	0.58	0.94	0.85	273	31
	Hil2	8.1826	46.4631	0.3	24	2513	14.03	1.30	0.97	0.82	135	14
	Wil	8.1971	46.4424	4.9	27	2379	23.29	1.54	0.95	0.83	60.5	7.8
	Wil2	8.1731	46.4594	0.4	29	2632	23.29	1.75	0.96	0.81	76.2	8.9
	Ritz	8.2257	46.4520	4.1	31	2147	6.45	0.91	0.93	0.85	242	38
	Spi	8.2107	46.4464	2.8	26	2219	3.04	0.48	0.95	0.85	560	100
	Chr	8.2038	46.4362	2.7	31	2032	2.01	0.42	0.94	0.86	760	220
	Bet	8.1886	46.4315	2.3	29	2082	1.18	0.25	0.94	0.86	1360	400
	Lou	8.1722	46.4185	1.4	32	1927	1.72	0.41	0.94	0.87	830	350
Soils	O-R	-	-	-	22	2659	28.68	0.88	0.99	0.81	64.1	2.7
	O-R(2)	-	-	-	22	2349	25.99	1.38	0.99	0.84	53.9	4.4
	O-Rg	-	-	-	29	2623	43.02	1.68	0.98	0.81	21.8	2.2
	O-Vg	-	-	-	20	2631	22.94	1.65	0.98	0.81	87.2	7.9
	O-I	-	-	-	35	2029	18.99	1.43	0.96	0.86	62.0	7.0
	N-V	-	-	-	30	2164	15.13	1.50	0.96	0.85	99	12
	N-Vg	-	-	-	24	2637	35.39	1.85	0.98	0.81	40.1	3.7
	H-R	-	-	-	21	2573	38.10	1.25	0.98	0.82	29.7	2.0
	H-I	-	-	-	33	1867	16.32	1.52	0.96	0.87	66.3	9.2
	H-I(2)	-	-	-	33	1867	14.86	1.09	0.96	0.87	76.9	7.8
	H-I(3)	-	-	-	33	1867	18.87	0.81	0.96	0.87	50.9	3.5
	W-R	-	-	-	21	2659	31.44	2.63	0.99	0.81	54.7	6.9
	W-V	-	-	-	28	2403	22.32	1.77	0.96	0.83	70.9	7.7

[a] ^{10}Be concentration with 1σ analytical error.
[b] Shielding factor is a catchment wide skyline shielding correction factor.
[c] Snow factor is a correction employed for snow shielding.
[d] Denudation rates calculated using the production rates and absorption coefficients of Schaller et al. (2002) and the scaling laws of Dunai (2000).

CHAPTER 5. HIGH DEGREES OF CHEMICAL WEATHERING ON STEEP, SLOWLY ERODING HILLSLOPES IN A POST-GLACIAL ALPINE LANDSCAPE

ABSTRACT

Rates of chemical weathering in the central Swiss Alps were calculated using a combination of ^{10}Be derived denudation rates and elemental mass loss in soils in order to determine chemical and physical weathering rates of individual landforms. The weathering signal varies with elevation and hillslope morphology, such that landforms in the same drainage basin exhibit different chemical weathering intensities, with chemical depletion fractions, CDF, ranging from 0.12 to 0.48. Ridge tops and interfluvial surfaces are associated with high degrees of chemical weathering, while hillslopes have a smaller chemical weathering contribution at equivalent elevations. A decline in the chemical weathering fraction with elevation indicates temperature being a dominant controlling factor on chemical weathering rates in these high Alpine basins. By comparing these data with modern stream cation flux, we are able to show that the chemical weathering rates of 14 to 80 t km^{-2} yr^{-1} have not varied significantly over Holocene timescales.

5.1. INTRODUCTION

Removal of atmospheric CO_2 by chemical weathering represents a mechanism that is essential to balancing volcanic emissions, thereby maintaining CO_2 levels over geologic time scales at levels that favor a habitable climate on Earth. The formation of mountain ranges should facilitate an increase in silicate weathering rates and consequently a reduction in atmospheric CO_2 and global temperatures. Of great interest today is the current trend of warming which will have direct impact upon surface geomorphic systems. A prerequisite for modeling future geomorphic response to climate change is knowledge of past and present driving forces. The last two decades in particular have seen advances in the ability to accurately quantify weathering over varying timescales. Basin-averaged denudation rates can

be calculated from cosmogenic nuclide concentrations in stream sediments (Brown et al., 1995; Granger et al., 1996; Schaller et al., 2001; Kirchner et al., 2001). Bedrock denudation rates can be similarly determined from the concentration of cosmogenic nuclides in weathered regolith (Riebe et al., 2004a). When used in conjunction with chemical depletion fractions derived from solute loss mass balance based on concentrations of refractory elements, the total denudation rate can be split into chemical and physical components. Riebe et al. (2004a) have used the combination of CDF and cosmogenic nuclide-derived denudation rates to demonstrate variation in chemical weathering rate with altitude in the Santa Rosa Mountains, California. In other studies, Riebe et al. (2001b, 2001b, 2004a) show a strong correlation between physical erosion and chemical weathering rates. While both CDF and cosmogenic nuclide-derived denudation rates average over the time of soil formation, 10^2-10^4 yrs, modern chemical weathering rates can be calculated using stream cation flux if stream discharge is known. Cation flux has been used extensively in the European Alps in order to characterize chemical weathering in proglacial and postglacial environments (Sharp et al., 1995; Hosein et al., 2004; Georg et al., 2006). Modern chemical weathering rates in formerly glaciated watersheds are often as much as an order of magnitude smaller than the long-term rates in the same regions (i.e. Taylor and Blum, 1995; Anderson et al., 2000). Furthermore, Green et al. (2006) and Burke et al. (2007), working on well studied soils in Australia and California (Heimsath et al., 2000, 2005) suggest that chemical weathering rates and CDF either increase or decrease with distance from ridgetops due to varying soil depth and mass transport. Yoo et al. (2007), also working in southeast Australia, has noted that downslope movement of soil material in the dissolved or solid state leads to a systematic redistribution of elements in these soils, with most of the solutes produced high on the ridge some of which are reprecipitated at lower elevation.

Here we attempt to address the question of the driving forces and rates of chemical weathering in the high Central Swiss Alps. We use Zr-derived CDF in conjunction with denudation rates of amalgamated soils samples to calculate chemical and physical rates in the upper Rhone Valley. Specific questions include; 1) Do the relationships between position on the hillslope and chemical weathering rates that have been shown in the low relief settings of coastal California and Australia (Green et al., 2006; Burke et al., 2007) hold for the steep, high relief settings of the Central Alps. 2) What is the temporal evolution of chemical weathering rates in these partially glaciated basins? 3) Does the correlation between

chemical weathering and physical erosion rates hold in areas undergoing transient response to Pleistocene glaciation?

5.1.1. Geomorphic setting

The Upper Rhone Valley, a.k.a. Goms (Figure 24), is located in the high central Swiss Alps. The northern and southern sides of the valley are underlain by the crystalline Aar and Gotthard Massifs respectively, with the meta-sedimentary Furka-Useren-Garvera Zone and Gomser Zwischenmassif between. The study area includes portions of six watersheds on the northern side of the Rhone. All sampling locations are underlain by the Aar Massif, which consists of granite (34% quartz, 35% plagioclase, 27% orthoclase and 4% mica) found only in the upper most sections of the northern lateral valleys, and gneiss (23 % quartz, 53% plagioclase, 17% orthoclase, <7% mica) as calculated from bedrock elemental data. These rocks dip steeply north northwest to vertical, striking roughly parallel to the main Rhone
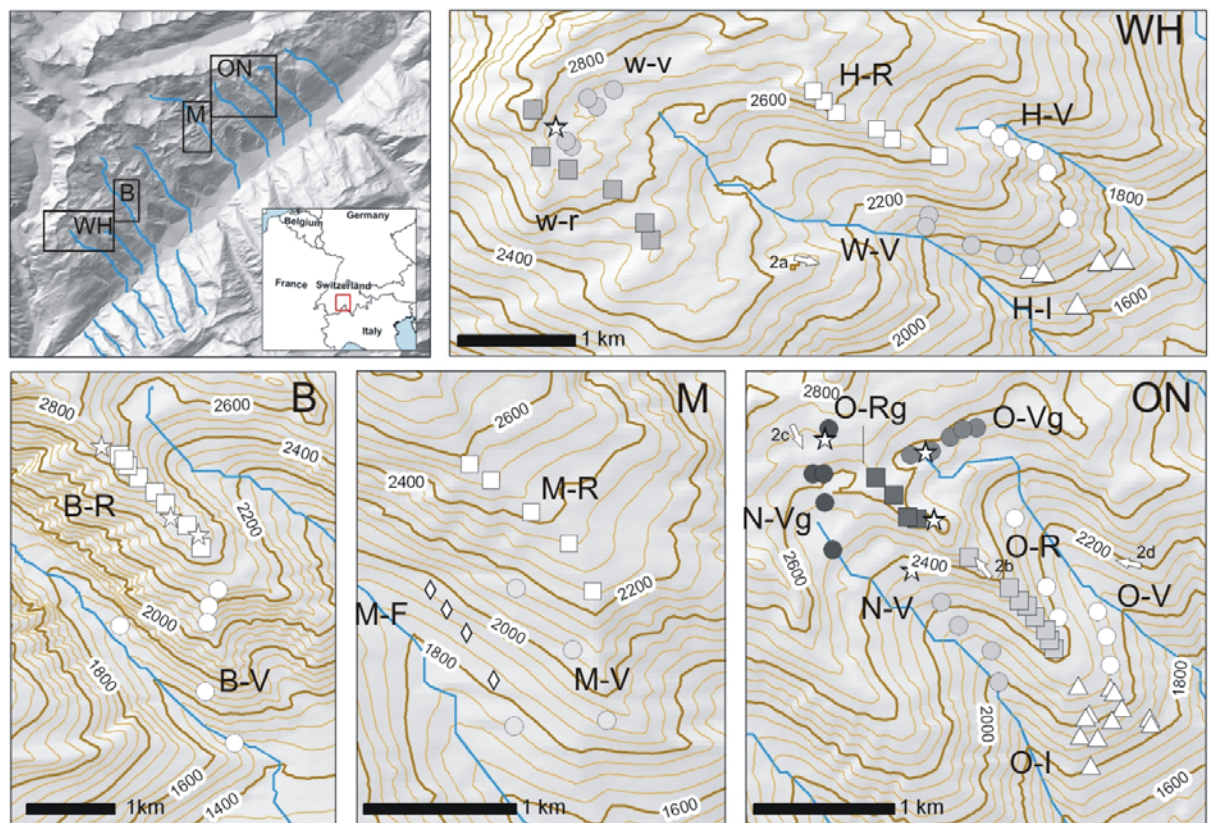
Figure 24. Location map of Goms and studied valleys showing sample sites. WH) sampling locations in the Wilerbach and Hilperschbach valleys (W- and H-), ON) Oberbach and Niderbach catchments (O- and N-), M) Minstigerbach valley (M-), and B) Walibach valley (B-). Ridge top samples (R) are shown with a square, valley side and upper basin samples (V) with a circle, interfluvial surfaces (I) with a triangle, and colluvial fans (F) with diamonds. Bedrock samples are marked with a star. Photo locations for Figure 25 are marked with white arrows.

Valley. Shear zones and large scale sackungen are abundant in the Aar Massif, and parallel the dominant foliation. A Swiss Meteo station at Ulrichen, in the Goms, 1345 m, records 3.1°C and 1137 mm yr^{-1} annual averages for temperature and precipitation.

During the LGM, the Rhone Glacier and its tributaries filled the valley to elevations of at least 2600 meters (Kelly et al., 2004). Post-LGM retreat of the Rhone Glacier opened the main Goms valley. Later, during the Younger Dryas, the northern lateral tributary valleys developed and contained cirque and valley glaciers of varying sizes. Retreat of the Rhone glacier allowed for the accumulation of alluvial and colluvial fans on the valley floor at the mouths of the lateral valleys and at large-scale slope failures. Smaller colluvial fans and talus cones are a common feature in the large lateral valleys and upper sections of the smaller valleys. Between the streams, relict triangular interfluvial surfaces remain (Figure 25a). These are typified by soil mantling with little to no bedrock exposure. The interfluves give way at higher elevations to broadly convex ridges with marked steps along their lengths (Figure 25b). The ridge tops are mantled by less than 50 cm deep soil, with bedrock patches becoming more prevalent at higher elevations as the soil become thinner. At the highest elevations, above 2700 meters, soils disappear almost completely. At low elevations, valley hillslopes (Figure 25c, d) have similar morphologies to the interfluvial surfaces, with soil cover and dense vegetation in the form of mostly pine, larch and grasses. At higher elevations, the valleys widen and vegetation switches to mosses and then disappears, as on the ridge tops. The main difference between the high elevation ridges and valleys is related to the presence of valley-side-up scarps (Ustaszewski and Pfiffner, 2008) that create abundant small lakes and basins in the valleys.

These faults are of uncertain origin, but are most likely due to neo-tectonic reactivation through differential glacioisostatic rebound of previous zones of weakness, gravitational collapse (which is more common at lower elevations), or a combination of these (termed composite faults by Ustaszewski and Pfiffner (2008)). In all cases, the scarps are parallel to the main Rhone Valley and exhibit valley-side-up geometry. The presence of these faults together with minimal glacial scouring results in slow denudation rates where present (Chapter 3). Basin-wide denudation rates are highest in the glacially scoured valleys, 1100-2100 mm ky^{-1} and lowest in the non-scoured, faulted valleys, 61-440 mm ky^{-1}. The most important consequence of the faults for the weathering regime is that hillslopes throughout the region are soil mantled, with removal of material being primarily through

Figure 25. Geomorphic settings in the Goms; a) forested interfluvial surfaces (triangular face is ~800m tall), b) broad ridge top.

Figure 25 continued. c) upper basins with thin soils (sheep for scale), and d) steep fluvial hillslopes.

diffusive creep processes where the soils are present, and debris flow processes where not present.

5.2. SAMPLING AND METHODOLOGY

A total of 104 soil and 10 bedrock samples were taken from four geomorphic zones in the upper Rhone Valley (Figure 24). Soils varied in thickness between ~10 and >100 cm. We randomized the sampling so that a wide range of soil depths are represented thereby measuring landscape-wide process rates (Riebe et al., 2003). Soils below the organic horizon were sampled from across the selected geomorphic regions to average out morphometric controls on soil production rates. In this way, we attempt to capture the wider trends of process rates throughout the region which are important for understanding the relationship between landforms, although admittedly sacrificing the fine resolution of other studies (Heimsath et al., 2001; Heimsath et al., 2005; Green et al., 2006; Burke et al., 2007). Interfluvial surfaces consistently have thicker soils (50-100 cm) as evidenced in road and trail cuts, while ridge tops and high elevation basins tended towards thin (0-50 cm) soils. These differences in soil depth are inherent to the different landforms, and therefore represent exactly the variations that we are trying to measure. By sampling on a variety of hillslope gradients and curvatures, the variations within individual landforms were minimized.

Four individual geomorphic domains were selected for analysis; ridge tops, interfluvial surfaces, basins and valley slopes, and colluvial fans (Figures 24 and 25). All samples were sieved to remove rock fragments larger than 1 cm. Care was taken to disaggregate the soils so that large soil particles would not be sieved away. A subsample of each individual soil was powdered and measured for major and trace element concentrations using X-ray fluorescence. The samples from the same domain; ridge, valley, etc., were then pooled using an equal mass of each, from which ^{10}Be concentrations in quartz were measured (Chapter 3) to determine total (chemical and physical) denudation rates (e.g. Riebe et al., 2004a).

In addition to weathered regolith, mass-balance approaches to chemical weathering require the measurement of representative parent material, i.e. fresh bedrock. A total of 10 samples from the two dominant lithologies were collected and analyzed for major and trace elements. It can be difficult in regions with high chemical weathering rates to find fresh

bedrock. The absence of alteration was verified using visual, microscopic, and elemental analysis. Effort was made to collect unweathered bedrock, however as White et al. (2001) showed, seemingly unweathered bedrock can be deeply altered with plagioclase as the first reactant. No evidence for plagioclase weathering was found in the collected bedrock samples.

As stated above, recent studies of chemical and physical weathering (Riebe et al., 2003; Green et al., 2006; Burke et al., 2007) rely on mass-balance equations using zirconium as an immobile element. Chemical weathering rates are calculated from the total denudation rate and the ratio of a conservative element in the parent and weathered material;

$$W = D \times \left(1 - \frac{C_{i,p}}{C_{i,w}} \right) \qquad\qquad 10$$

where W is the chemical weathering rate, D is the denudation rate, C_i is the concentration of an immobile element (here Zr) the parent (p) and weathered material (w), respectively. Denudation rates are typically estimated either from suspended sediment load data from rivers, or in situ-produced cosmogenic nuclides in rock, regolith or soil, and elemental concentrations are normally measured on bedrock and soil or saprolite. The final term in equation 10 is defined as the chemical depletion fraction by Riebe et al. (2001a, 2001b).

$$\left(1 - \frac{C_{i,p}}{C_{i,w}} \right) = CDF \qquad\qquad 11$$

The CDF is a measure of the fraction of total weathering due to chemical processes. This study follows sampling methodologies similar to those of Riebe et al. (2003) in order to measure chemical and physical weathering rates as the landscape scale. [10]Be derived hillslope denudation rates were measured on soil samples which were pooled and manually mixed using an equal mass of each soil (Chapter 3). One major advantage of this method is that the [10]Be-derived denudation rates are calculated from exactly the same samples from which the chemical analyses were performed (Riebe et al., 2003), so that any (quite probable) spatial variation in rates does not bias the results. A density of 2.7 g cm^{-3} is used for calculating sediment yields from the cosmogenic nuclide-derived denudation rates because

Table 5. Topographic, chemical, and physical parameters for the pooled soil samples.

Location	Elevation (m) [a]	Slope (°) [a]	CDF(Zr) [b]	Denudation Rate [c] (mm ky-1)	Chemical Flux [d] (t km^{-2} yr^{-1})	Physical Flux [e] (t km^{-2} yr^{-1})
W-R	2671 ± 106	21 ± 9	0.25 ± 0.06	55 ± 14	37 ± 22	111 ± 31
H-R	2549 ± 109	21 ± 8	0.30 ± 0.04	30 ± 8	24 ± 13	56 ± 19
B-R	2415 ± 5	26 ± 5	0.37 ± 0.15	-		-
M-R	2565 ± 11	24 ± 11	0.33 ± 0.10	-		-
O-R	2306 ± 86	22 ± 7	0.39 ± 0.04	59 ± 11	61 ± 18	98 ± 25
O-Rg	2616 ± 35	29 ± 16	0.12 ± 0.09	22 ± 8	7 ± 12	52 ± 18
W-V	2341 ± 376	28 ± 15	0.31 ± 0.05	71 ± 15	60 ± 24	132 ± 33
H-V	2120 ± 104	34 ± 7	0.27 ± 0.07	-		-
B-V	1967 ± 5	31 ± 5	0.37 ± 0.17	-		-
M-V	1910 ± 8	33 ± 8	0.35 ± 0.09	-		-
N-V	2099 ± 92	30 ± 3	0.34 ± 0.05	99 ± 20	90 ± 32	177 ± 45
O-V	2153 ± 94	30 ± 4	0.37 ± 0.06	-		-
N-Vg	2606 ± 79	24 ± 5	0.26 ± 0.04	40 ± 10	28 ± 16	81 ± 23
O-Vg	2565 ± 17	20 ± 14	0.21 ± 0.05	87 ± 17	50 ± 27	186 ± 39
H-I	1781 ± 84	33 ± 6	0.38 ± 0.04	65 ± 12	66 ± 18	109 ± 26
O-I	1966 ± 102	35 ± 6	0.40 ± 0.02	62 ± 12	66 ± 19	101 ± 27
B-F	1904 ± 7	34 ± 7	0.48 ± 0.19	-		-

[a] calculated from SRTM data, errors are 1-sigma
[b] calculated using equation 11, standard errors are reported
[c] originally reported in Chapter 3
[d] calculated using equation 10 and a density of 2.7g cm^{-2}
[e] equal to D-W

we are measuring the total rate of conversion of bedrock to soil, which at steady state is equal to the sum of the rate of soil removal from the surface by erosion and the removal of dissolved species in solution. Also, the ^{10}Be derived denudation rates and ages are calculated based on this density.

Chemical analysis was performed on individual soils. The results were then averaged for each landform using the arithmetic mean, with standard errors (e.g. Riebe et al., 2001a, 2001b) are reported for each element (Table 6). In this way, we get the variability of the dataset along with the landform averages which can be directly compared to the pooled denudation rates. Topographic metrics, elevation and slope, are similarly averaged, with the difference that the 1-sigma variance is reported instead of the standard error.

5.3. RESULTS

Chemical depletion fractions calculated from zirconium concentrations in soils and bedrock vary between 0.1 and 0.5, (Figure 26), indicating that chemical weathering accounts for between 10 and 50% of total denudation in this setting. The colluvial fan and interfluvial samples also appear to have higher average CDF than the ridges and valleys. For the two
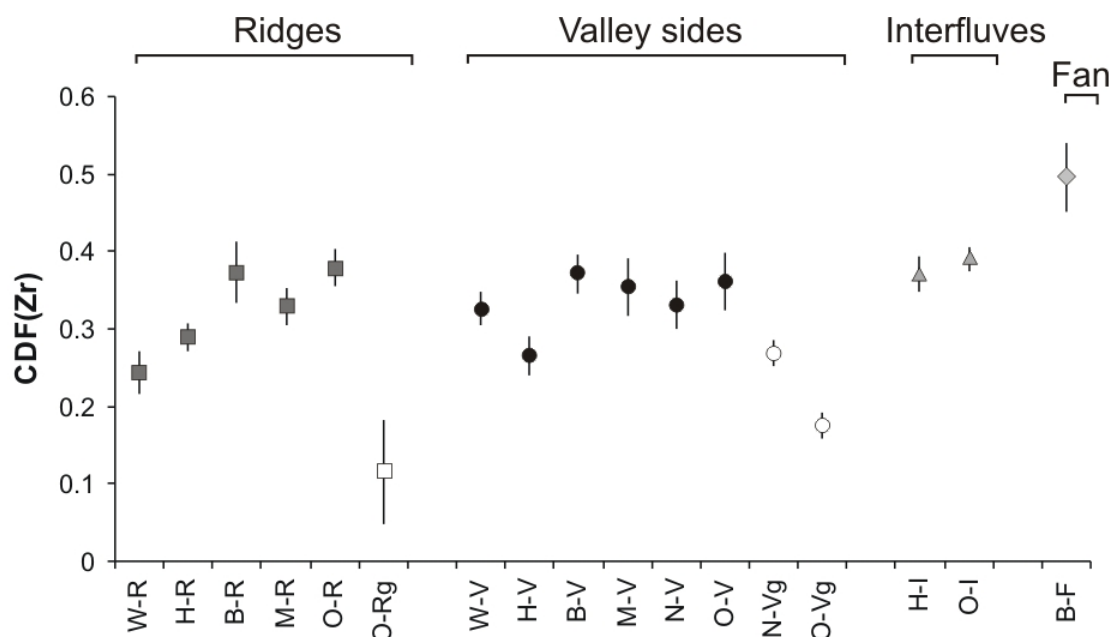
Figure 26. Average CDF values for each sampling location. Symbols match Figure 24, with ridge top samples shown with a square, valley side and upper basin samples with a circle, interfluvial surfaces with a triangle, and colluvial fans with a diamond. Samples are grouped according to landform, and sorted within each category, left to right from SW to NE. Granite lithologies are indicated with open symbols.

landforms in which they are found (i.e. valleys and ridges), granites have lower CDF than the gneisses. Chemical weathering rates for individual landforms were calculated using Zr based CDF and ^{10}Be derived soil denudation rates. These soil based chemical weathering rates vary between 7 and 90 t km^{-2} y^{-1}, based on a density of 2.7 g cm^{-3} (Table 5, Figure 27).

5.4. DISCUSSION

5.4.1. Controls on chemical weathering rates

Despite the clarity of the relationships between lithology and CDF (Figure 26) and geomorphic position and CDF (Figure 27), the causes are not so straightforward. Granite is only found at elevations above 2500 meters where soils are thinner, and only in the NE ridges and basins, while gneisses are found in all basins at lower elevations. In this case, CDF might be a function of soil depth (Green et al., 2006), or lithology as suggested above. Alternatively, chemical weathering rates may be causally related to elevation. A plot of mean elevation vs. CDF (Figure 27a) shows a broadly negative correlation. Altitude in and of itself should exert no control over chemical weathering, but many of the processes that scale with
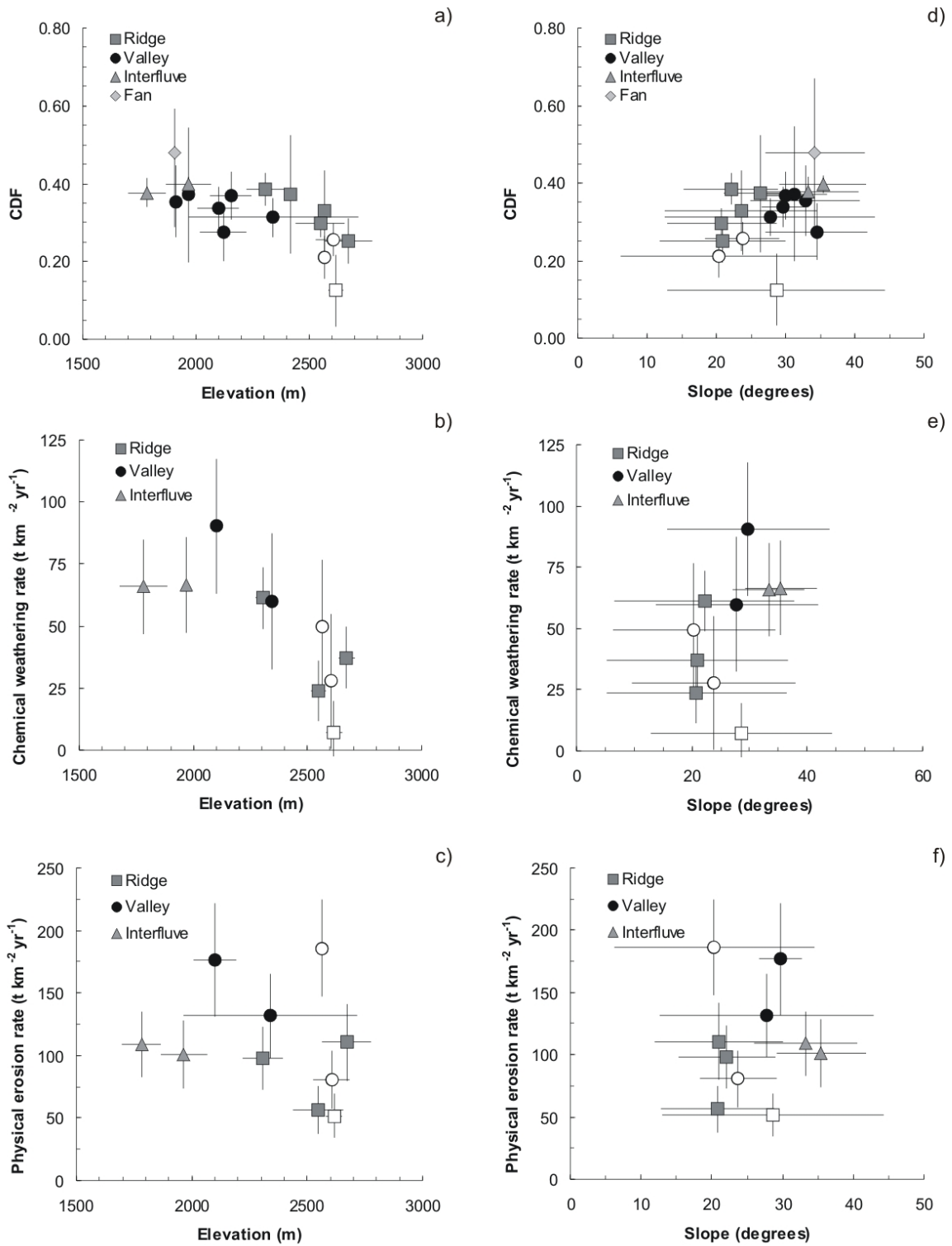
Figure 27. CDF plotted against (a) elevation and (d) hillslope gradient for the amalgamated soil samples. (b) and (e) show the chemical weathering rate vs. elevation and hillslope gradient. In (c) and (f), physical erosion rate is plotted against elevation and hillslope gradient.   Granite lithologies are shown with open symbols.

elevation are likely to have a profound impact on the chemical weathering rate. Two such factors are temperature and vegetation cover. The veracity of these potential controlling factors is discussed in detail in the following sections.

5.4.1.1. Geomorphic controls

Chemical depletion fractions vary within and between the individual landforms (Figures 26 and Table 5). Colluvial fans exhibit the highest CDF value, 0.5±0.2, followed by interfluvial surfaces, 0.4±0.04; and valley hillslopes, 0.3±0.2, and ridgetops, 0.3±0.2 when excluding the 3 granite samples (Table 5). Yoo et al. (2007) show that where hillslope transport of soil occurs, CDF-derived weathering rates can overestimate the true weathering rate such that mass loss due to chemical weathering decreases away from ridges, and in their study area, mass gains even occur. This does not appear to be the case for the Goms as can be seen from the individual element concentrations and mass loss calculations (Table 6, Figure 28). Yoo et al. (2007) show decreasing mass loss shifting to mass gains in some cases for reported oxides (Si, Al, Fe, Mg, Ca, Na, K, and P) with increasing distance from the ridgetop, whereas the mean mass loss in on ridgetops in the Goms are equivalent within error to those on hillslopes for these oxides. Because there is no measured mass gain downslope, the original equations of Riebe et al. (2001a, 2001b) may be used without the modifications for transport of Yoo et al. (2007).

Despite the large spread in the data, meaningful relationships can be identified when comparing the plots of CDF and the chemical weathering rate of individual landforms against elevation and slope (Figure 27). CDF of ridge top samples are consistently higher than those in the valleys at the same mean elevation (Figure 27a). This shows that the total contribution of chemical weathering processes to total denudation is higher on ridges than on valley hillslopes, confirming the findings of Burke et al. (2007) and Yoo et al. (2007), who found that chemical weathering decreased with distance from a ridge top. Ridges by their nature have shallower slopes than the hillslopes to either side, therefore, physical transport rates on the ridge should be lower than on hillslopes leading to higher CDF for the same amount of total denudation. This appears to be the case as, despite high standard deviations, the mean sample slopes for ridges, 24±19º, are lower than those of the adjacent valleys, 31±21º (Figure 28a, b). Interfluvial surfaces in general exhibit high slopes, 34±9º, high CDF values of ca. 0.4±0.04, and denudation rates similar to ridges (again using only the gneissic landforms, Table 5). These surfaces are forested and have very active soil mixing processes. However,

due to the extensive vegetation, which acts as a screen and stabilizer, physical rates remain low, despite the high slopes (Figure 27d). The fan soils have the highest CDF measured, 0.48±0.19, indicating that nearly half the mass loss is due to chemical dissolution. The location of the fans at the foot of the steep side valleys of the glacially scoured basins might results in slow sediment transport allowing stronger chemical weathering to occur. It is also likely that the fan material, derived from the overlying hillslopes, was weathered before being deposited.

5.4.1.2. Lithological controls

CDF can also provide an insight into mineralogical controls over weathering processes. The relative mass loss of individual element, $\tau_{i,j}$, can be calculated using the concentration, C, of immobile (i) or mobile (j) elements in either the weathered material (w) or the parent material (p) (Brimhall and Dietrich, 1987).

$$\tau_{i,j} = \left(\frac{C_{j,w}}{C_{j,p}} \frac{C_{i,p}}{C_{i,w}} - 1 \right)$$

13

The trend for soils developed on granitic lithologies to be less weathered than for gneisses is also apparent in the elemental mass loss data, with 10-20% less mass lost from granites than from gneiss (Figure 28). Because these two rock types are mineralogically similar, this difference in chemical weathering must have some other cause such as increased jointing or weak sheared zones in the gneisses. In all samples, large mass loss of calcium and sodium (~ 50% for each) is evidence for rapid weathering of plagioclase. Lower potassium and aluminum losses (~38%) indicate either minimal potassium feldspar dissolution, or the formation of illite clays, leading to retention of potassium in the soils. The fact that Si and Al are more closely correlated than Al and K suggests that the later is the case. Furthermore, titanium is also shown to be a conservative element with an average $\tau_{Zr,Ti}$ of 0 (Table 6).
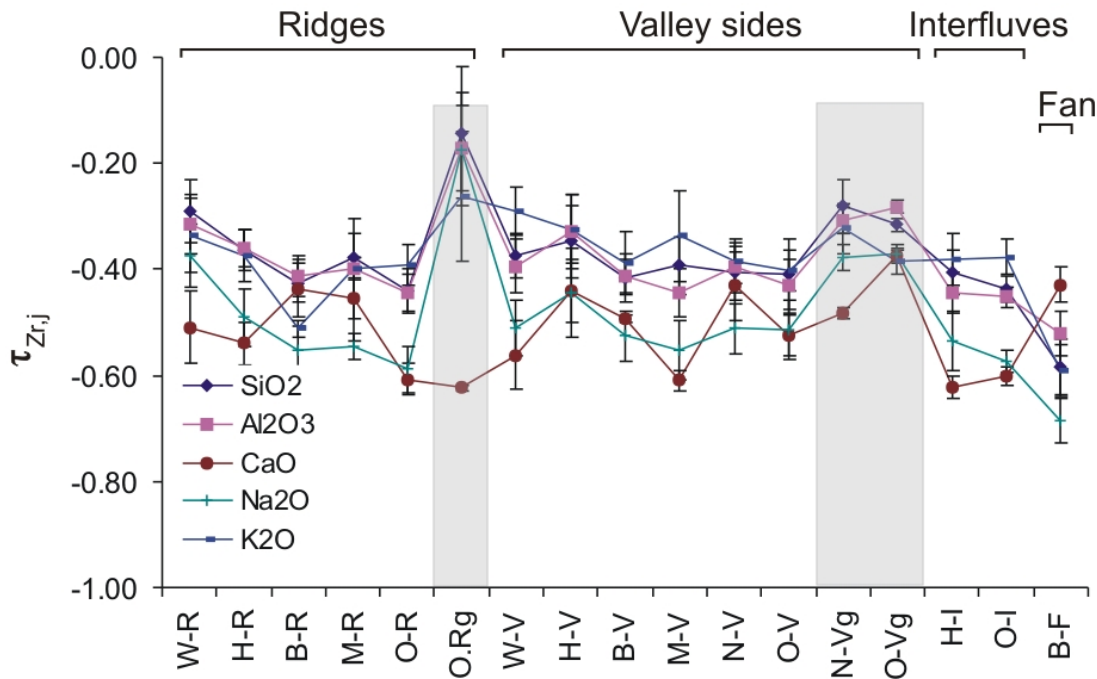
Figure 28. Mass loss of the major mobile rock forming cations for each sampling region. Samples are grouped according to landform, and sorted within each category, left to right from SW to NE. Granitic terrains are marked by grey shading.

5.4.1.3. Effects of vegetation

A review of the direct links between chemical weathering and vegetation was recently given by Amundson et al. (2007). The action of roots disrupts the soil body and provides conduits for downward flow of surface water. This acts to constantly refresh the groundwater, driving chemical weathering. Furthermore, vegetation also releases abundant organic acids, which aid in the weathering reactions (Berner et al., 2004; Richter et al., 2007). In the Goms valleys, trees give way to grasses and then patchy mosses by ~2400 meters in the valleys. This reduction in vegetation with altitude, could also lead to lower CDF at higher elevations.

5.4.1.4. Temperature controls

If chemical weathering rates are temperature dependent (Vebel,1993; Brady and Carrol, 1994; White and Blum, 1995; Oliva et al., 2003; Riebe et al., 2004a) then they should decrease with altitude. The dependence of weathering on temperature has been modeled using Arrhenius equations (e.g. White and Blum, 1995):

$$W_j = A\,\mathrm{e}^{\frac{\Delta E_a}{RT}} \qquad\qquad 14$$

Where W_j is the weathering rate of element j, A is a weathering constant, ΔEa is the activation energy (kJ mol^{-1}), R is the gas constant, and T is the temperature. Activation energies for common silicate minerals vary from about 50 to 120 kJ mol^{-1} (White, 2003). The most appropriate value for the current study is that of 77 kJ mol^{-1} (Vebel, 1993) for plagioclase weathering determined from granites. One can also model the change in CDF with altitude (Riebe et al., 2004a) by substituting equation 14 into equation 10, assuming that the weathering constant, A, is the same for each location, and solving for the change in chemical depletion fraction caused by a temperature change from T_1 to T_2, $\Delta CDF_{1,2}$:

$$\Delta CDF_{1,2} = \mathrm{e}^{\frac{\Delta E_a}{R}\left(\frac{1}{T_2}-\frac{1}{T_1}\right)} \qquad\qquad 15$$

As mean temperature drops with a lapse rate of ~0.6°C per 100 meters, the approximately
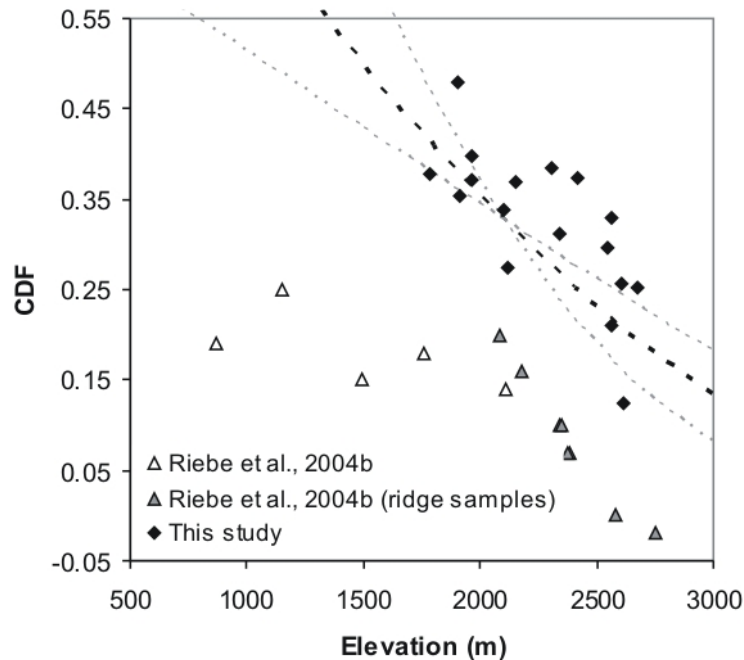
Figure 29. Chemical depletion fractions plotted against elevation. An Arrhenius equation, 15, as modified by Riebe et al. (2004a) (dashed line) scaled to the mean annual temperature and average CDF at 2 km, and an activation energy of 77 kJ mol^{-1} (Vebel, 1993), suggests that the decrease in CDF with altitude is due to temperature effects. The trends for the minimum and maximum, 50 and 120 kJ mol^{-1}, activation energies are shown with grey dashed lines.

1500 m relief across these valleys results in significantly lower temperatures in the upper basins. Using this lapse rate, temperatures can be estimated for each elevation, from a starting mean annual temperature of 3.1ºC, for the town of Ulrichen at the mouth of the Oberbach at 1345 m, yielding negative average annual temperature above approximately 1900 meters. While the data of Riebe et al. (2004a) did not decrease with the rate predicted by temperature controlled kinetics, weathering in the Goms is well described by the Arrhenius relationship. This means that the ~46% decrease in chemical depletion fractions from the lowest to the highest sampling locations, which are ~5.4ºC colder, can be explained by reduced reaction kinetics (Figure 29). Furthermore, the good fit with the activation energy reported for plagioclase by Vebel (1993) further supports that weathering in these valleys proceeds primarily through plagioclase breakdown.

5.4.2. Weathering in the Holocene

The soil mass loss method used here measures total mass loss over the residence time of the soil. Determination of chemical weathering rates, therefore, requires knowledge of the residence time of the soil. The pooled soil denudation rates used here, based on cosmogenic nuclide concentration, average denudation through a depth of roughly 70 cm (including muon production) so that the constant denudation rate residence time within this interval can be calculated. The soils in the Goms with denudation rates of 22 to 99 mm ky^{-1} are therefore formed over approximately 5-12 kyr.

For comparison with mass loss-derived chemical weathering rates of 7-90 t km^{-2} yr^{-1} in the Goms, modern chemical weathering rates can be calculated from cation fluxes in streams. While there are no stream cation flux data for these valleys, studies have been carried out in similar settings in the Swiss Alps (Sharp et al., 1995; Hosein et al., 2004; Georg et al., 2006) yielding chemical weathering rates of ~35±13 t km^{-2} y^{-1}. These rates are within error of the long-term rates for the Goms. A compilation of mountainous granitic catchments by West et al. (2005) yields ~20 t km^{-2} y^{-1} average, and ~47 t km^{-2} y^{-1} maximum values for chemical weathering rates. In other mountainous regions, (Dethier and Lazarus, 2006) report 2-6 t km^{-2} y^{-1} for the Front Range of the Rocky Mountains, and (Anderson et al., 2000) 10-120 t km^{-2} y^{-1} (16 t km^{-2} y^{-1} away from the glacier) for the Bench Glacier in Alaska. So it is unlikely that our new value under- or overestimates the modern chemical weathering rate significantly. This implies that early post-glacial chemical weathering rates in this region were similar to today, in contrast other glacial settings (Taylor and Blum, 1995; Anderson et

al., 2000). The rate of chemical weathering decreases with soil age in the case of the Wind River Mountains (Taylor and Blum, 1995), and distance from the modern glacier (a proxy for soil age) in the Bench Glacier, Alaska (Anderson et al., 2000). It is possible that the majority
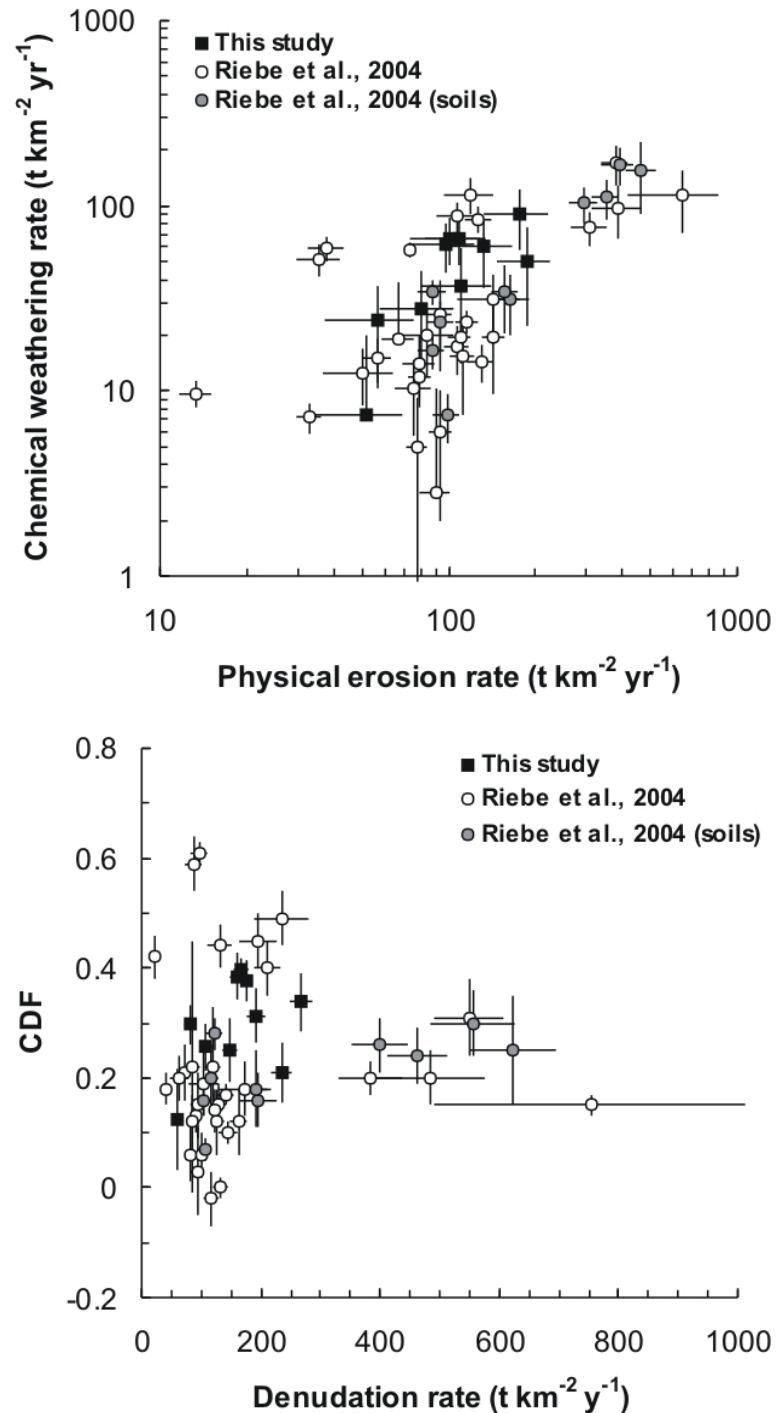
Figure 30. a) Chemical weathering rate plotted against physical denudation rate, and b) CDF_{Zr} plotted against total denudation rate. Black squares are data from this study, circles are from Riebe et al. (2004b), open circles are data derived from sediment sampling (hollows or streams), while grey circles are derived from pooled soils.

of the weathering measured by mass loss occurred shortly after deglaciation and that modern hillslope chemical weathering rates are lower. However, as the variation in our long-term chemical weathering rates, 7-90 t km^{-2} yr^{-1}, are of the same order as modern variations measured from cations in solution in similar environments (e.g. Taylor and Blum, 1995 and Anderson et al., 2000) it is probable that this is not the case and that short-term and long-term rates are similar.

5.4.3. Relation between physical and chemical weathering

Riebe et al. (2004b) reported that chemical weathering rates are related to physical erosion rates for granitic terrains, with an order of magnitude variability. The Goms data plot into this general trend, but show much less variability in physical erosion rates (Figure 30a). It should also be noted that a portion of the denudation rates from Riebe et al. (2004b) are basin-averaged rates as opposed to pooled soil rates reported here. The use of basin-averaged rates is valid if the rates derived from individual soil samples are scalable to the entire drainage basin (e.g. Riebe et al., 2004a). In the Goms, basin-averaged rates are faster by almost a factor of three than the pooled soils from which the CDF values were calculated (Chapter 3). Clearly, in the upper Rhone valley, process rates are not equivalent at hillslope and basin scales. Therefore, the discrepancy between high CDF-derived chemical weathering rates (i.e. Riebe et al., 2004b) and low stream cation-derived chemical weathering rates described by West et al. (2005) might be due to the invalid assumption of scaleability. If the data of Riebe et al. (2004b) are also not scaleable, then the open symbols in Figure 30b should be discarded. The small range of measured denudation rates in the Goms leads to a weak correlation between chemical weathering and physical erosion (Figure 30a). Together with the strong correlation between temperature and chemical weathering (Figure 29), this further supports a kinetic temperature control of chemical weathering.

5.5. CONCLUSIONS

The landform dependent chemical weathering and physical erosion rates measured here provide a key to understanding basin-wide weathering processes and post-glacial weathering dynamics. Chemical weathering is not constant across even small drainage basins, as shown by variations CDF and elemental mass loss with lithology and landscape

position. Soils developed on high elevation granites are less weathered than those formed on gneisses. Ridges and valleys have distinct weathering signatures. Longer soil residence times (i.e. slower denudation rates) result in more intense chemical weathering for ridge tops than the adjacent valley hillslopes. The average long-term chemical weathering rate, 49 ± 25 t km^{-2} yr^{-1}, is within the range of modern cation flux-based chemical weathering rates in the Swiss Alps, 35 ± 13 t km^{-2} y^{-1}.

Here, we have shown that chemical weathering is a function of temperature such that, as temperature decreases with elevation, CDF and chemical weathering rates decrease. This is in contradiction to previous studies (Riebe et al., 2001a, 2001b, 2004b); chemical weathering in Goms appears to be controlled by temperature. This may be due to the incomplete linkage between rock uplift (Schlatter et al., 2005) and denudation in the upper Rhone valley. An uplifting bedrock knickpoint at the outlet of the Goms negates the effect of rock uplift locally by maintaining the geomorphic baselevel for these valleys, despite rapid uplift of the entire system relative to the Swiss Mittelland. This special case leads to a situation in which the driving force between chemical and physical weathering may be determined. The relationship between chemical and physical weathering processes, in which chemical alteration enhances physical disintegration and visa versa ensures that these rates will be to some degree covariant, however without rejuvenation in the form of incision to drive physical processes, chemical weathering set by reaction kinetics appears to dominate weathering of soil covered hillslopes in the upper Rhone basin.

Table 6. Elemental analysis of pooled soil samples averaged from individual samples. Standard errors for each element are reported.

Element concentrations

	Samples	SiO₂ %	TiO₂ %	Al₂O₃ %	Fe₂O₃ %	MgO %	CaO %	Na₂O %	K₂O %	Rb ppm	Sr ppm	Zr ppm
W-R	6	71.83 ± 0.35	0.17 ± 0.01	12.11 ± 0.21	1.58 ± 0.12	0.39 ± 0.05	0.27 ± 0.15	3.44 ± 0.17	3.74 ± 0.11	143.8 ± 5.3	73.0 ± 62.2	117.8 ± 15.1
H-R	6	62.63 ± 0.46	0.49 ± 0.02	14.70 ± 0.07	3.97 ± 0.17	0.91 ± 0.07	1.41 ± 0.07	3.27 ± 0.17	2.83 ± 0.13	99.1 ± 9.2	515.9 ± 41.7	186.8 ± 8.7
B-R	5	66.44 ± 0.56	0.37 ± 0.01	13.52 ± 0.13	2.56 ± 0.13	0.95 ± 0.04	1.34 ± 0.11	3.02 ± 0.13	3.11 ± 0.10	146.9 ± 9.7	361.9 ± 41.1	162.3 ± 12.2
M-R	8	63.47 ± 0.88	0.46 ± 0.03	15.23 ± 0.26	3.02 ± 0.28	0.80 ± 0.13	1.97 ± 0.21	3.52 ± 0.09	2.24 ± 0.22	87.2 ± 19.0	702.2 ± 74.6	181.6 ± 7.6
O-R	8	62.45 ± 0.34	0.43 ± 0.02	14.75 ± 0.09	2.92 ± 0.25	0.81 ± 0.05	1.44 ± 0.06	3.54 ± 0.10	2.54 ± 0.08	101.8 ± 3.7	568.2 ± 26.4	161.3 ± 10.7
O-Rg	4	65.36 ± 0.32	0.37 ± 0.01	14.84 ± 0.13	2.67 ± 0.03	0.98 ± 0.03	1.47 ± 0.03	4.14 ± 0.13	2.52 ± 0.08	97.8 ± 6.8	535.5 ± 7.6	155.2 ± 16.8
W-V	10	63.47 ± 0.35	0.21 ± 0.01	11.44 ± 0.15	1.34 ± 0.14	0.31 ± 0.08	0.44 ± 0.11	2.88 ± 0.10	3.39 ± 0.11	139.0 ± 6.2	92.0 ± 47.9	125.6 ± 11.7
H-V	6	72.84 ± 0.33	0.16 ± 0.03	12.23 ± 0.15	1.46 ± 0.33	0.24 ± 0.09	0.43 ± 0.10	3.17 ± 0.17	4.12 ± 0.09	154.2 ± 8.3	75.8 ± 39.5	137.0 ± 14.9
B-V	4	64.37 ± 1.01	0.43 ± 0.03	14.69 ± 0.05	2.83 ± 0.29	1.01 ± 0.13	1.68 ± 0.05	3.79 ± 0.17	2.74 ± 0.17	106.2 ± 7.6	585.0 ± 13.4	185.8 ± 8.4
M-V	6	61.92 ± 0.98	0.48 ± 0.02	14.81 ± 0.15	3.38 ± 0.20	1.38 ± 0.05	1.87 ± 0.07	3.64 ± 0.17	2.65 ± 0.15	104.0 ± 2.3	593.0 ± 28.8	172.8 ± 10.6
N-V	4	64.60 ± 0.60	0.37 ± 0.03	13.95 ± 0.13	2.62 ± 0.26	0.85 ± 0.15	1.34 ± 0.07	3.38 ± 0.06	2.87 ± 0.03	116.8 ± 2.5	423.8 ± 23.7	176.5 ± 15.7
O-V	6	63.84 ± 0.87	0.42 ± 0.03	15.18 ± 0.10	3.00 ± 0.24	1.08 ± 0.08	1.77 ± 0.09	3.72 ± 0.11	2.76 ± 0.11	109.5 ± 8.2	554.5 ± 66.0	179.0 ± 18.1
N-Vg	5	61.88 ± 0.22	0.47 ± 0.01	14.98 ± 0.14	3.61 ± 0.09	1.28 ± 0.01	1.70 ± 0.03	3.72 ± 0.07	2.67 ± 0.08	107.0 ± 5.3	573.5 ± 3.9	161.3 ± 7.7
O-Vg	5	64.74 ± 0.62	0.44 ± 0.00	14.74 ± 0.09	3.02 ± 0.04	1.23 ± 0.01	1.42 ± 0.01	3.58 ± 0.04	3.04 ± 0.05	116.8 ± 2.4	479.5 ± 0.8	173.4 ± 3.6
H-I	5	65.81 ± 0.77	0.42 ± 0.02	14.43 ± 0.14	2.89 ± 0.18	0.84 ± 0.05	1.33 ± 0.04	3.65 ± 0.20	2.81 ± 0.08	119.4 ± 2.7	411.0 ± 27.0	181.6 ± 9.9
O-I	12	64.37 ± 0.29	0.45 ± 0.01	14.71 ± 0.05	3.10 ± 0.09	0.97 ± 0.04	1.46 ± 0.06	3.48 ± 0.05	2.93 ± 0.06	130.6 ± 4.5	475.8 ± 19.7	188.0 ± 6.7
B-F	5	56.52 ± 0.60	0.74 ± 0.14	15.49 ± 0.33	5.26 ± 0.01	1.98 ± 0.18	2.55 ± 0.08	3.06 ± 0.06	2.29 ± 0.02	119.6 ± 0.2	663.6 ± 0.4	229.2 ± 18.9
Granite	5	35.20 ± 0.35	0.08 ± 0.00	6.92 ± 0.19	0.91 ± 0.04	0.15 ± 0.02	0.44 ± 0.13	2.80 ± 0.11	3.74 ± 0.13	189.6 ± 3.9	77.2 ± 7.9	100.6 ± 2.8
Gneiss	5	32.29 ± 0.07	0.17 ± 0.00	8.59 ± 0.05	1.29 ± 0.05	0.59 ± 0.07	1.56 ± 0.22	3.68 ± 0.12	2.36 ± 0.10	103.0 ± 6.1	781.0 ± 64.2	111.8 ± 3.2

Mass Loss (relative to Zr)

	SiO₂	TiO₂	Al₂O₃	Fe₂O₃	MgO	CaO	Na₂O	K₂O	Rb	Sr
W-R	-0.29 ± 0.06	-0.06 ± 0.05	-0.31 ± 0.06	0.06 ± 0.05	-0.24 ± 0.08	-0.51 ± 0.07	-0.37 ± 0.06	-0.33 ± 0.07	-0.30 ± 0.04	-0.48 ± 0.07
H-R	-0.36 ± 0.04	0.03 ± 0.03	-0.36 ± 0.04	0.10 ± 0.08	-0.42 ± 0.08	-0.54 ± 0.04	-0.49 ± 0.05	-0.37 ± 0.05	-0.31 ± 0.06	-0.48 ± 0.06
B-R	-0.42 ± 0.04	-0.01 ± 0.07	-0.41 ± 0.04	0.04 ± 0.13	-0.48 ± 0.08	-0.44 ± 0.06	-0.55 ± 0.02	-0.51 ± 0.02	-0.48 ± 0.04	-0.43 ± 0.06
M-R	-0.38 ± 0.04	0.10 ± 0.09	-0.40 ± 0.02	0.00 ± 0.12	-0.10 ± 0.13	-0.46 ± 0.08	-0.55 ± 0.04	-0.40 ± 0.09	-0.26 ± 0.17	-0.36 ± 0.06
O-R	-0.44 ± 0.04	0.01 ± 0.04	-0.44 ± 0.04	0.27 ± 0.07	-0.43 ± 0.04	-0.61 ± 0.03	-0.59 ± 0.04	-0.39 ± 0.04	-0.41 ± 0.03	-0.60 ± 0.03
O-Rg	-0.14 ± 0.12	0.12 ± 0.03	-0.17 ± 0.08	0.09 ± 0.10	0.46 ± 0.10	-0.62 ± 0.01	-0.17 ± 0.11	-0.26 ± 0.12	-0.32 ± 0.14	-0.18 ± 0.00
W-V	-0.37 ± 0.04	-0.01 ± 0.06	-0.39 ± 0.05	0.07 ± 0.11	-0.16 ± 0.12	-0.56 ± 0.06	-0.51 ± 0.05	-0.29 ± 0.05	-0.25 ± 0.05	-0.59 ± 0.06
H-V	-0.35 ± 0.07	0.14 ± 0.08	-0.33 ± 0.07	0.38 ± 0.15	-0.04 ± 0.13	-0.44 ± 0.06	-0.44 ± 0.08	-0.32 ± 0.06	-0.26 ± 0.05	-0.46 ± 0.07
B-V	-0.42 ± 0.05	-0.10 ± 0.07	-0.41 ± 0.03	0.00 ± 0.09	-0.32 ± 0.11	-0.49 ± 0.01	-0.53 ± 0.05	-0.39 ± 0.06	-0.33 ± 0.05	-0.55 ± 0.02
M-V	-0.39 ± 0.05	-0.19 ± 0.06	-0.44 ± 0.04	-0.11 ± 0.07	-0.45 ± 0.04	-0.61 ± 0.02	-0.55 ± 0.04	-0.34 ± 0.09	-0.27 ± 0.05	-0.66 ± 0.01
N-V	-0.41 ± 0.07	0.07 ± 0.08	-0.40 ± 0.05	0.19 ± 0.11	-0.08 ± 0.14	-0.43 ± 0.06	-0.51 ± 0.05	-0.39 ± 0.04	-0.33 ± 0.05	-0.50 ± 0.04
O-V	-0.41 ± 0.07	-0.08 ± 0.09	-0.43 ± 0.05	-0.06 ± 0.11	-0.35 ± 0.10	-0.52 ± 0.04	-0.52 ± 0.06	-0.40 ± 0.04	-0.36 ± 0.07	-0.53 ± 0.07
N-Vg	-0.28 ± 0.05	-0.12 ± 0.04	-0.31 ± 0.02	-0.18 ± 0.05	-0.29 ± 0.02	-0.48 ± 0.01	-0.38 ± 0.02	-0.32 ± 0.05	-0.40 ± 0.05	-0.28 ± 0.00
O-Vg	-0.31 ± 0.01	0.27 ± 0.02	-0.28 ± 0.01	-0.15 ± 0.03	0.04 ± 0.01	-0.38 ± 0.01	-0.37 ± 0.02	-0.38 ± 0.02	-0.40 ± 0.03	-0.01 ± 0.00
H-I	-0.40 ± 0.04	-0.12 ± 0.04	-0.44 ± 0.04	-0.04 ± 0.05	-0.47 ± 0.04	-0.62 ± 0.02	-0.53 ± 0.05	-0.38 ± 0.05	-0.28 ± 0.03	-0.67 ± 0.04
O-I	-0.44 ± 0.02	-0.07 ± 0.02	-0.45 ± 0.02	0.00 ± 0.03	-0.40 ± 0.04	-0.60 ± 0.02	-0.57 ± 0.02	-0.38 ± 0.03	-0.23 ± 0.04	-0.64 ± 0.02
B-F	-0.58 ± 0.05	0.24 ± 0.05	-0.52 ± 0.04	0.39 ± 0.05	-0.01 ± 0.07	-0.43 ± 0.03	-0.69 ± 0.04	-0.59 ± 0.05	-0.42 ± 0.04	-0.59 ± 0.01
Average values	-0.38 ± 0.09	0.01 ± 0.13	-0.38 ± 0.08	0.06 ± 0.17	-0.22 ± 0.25	-0.51 ± 0.08	-0.49 ± 0.12	-0.38 ± 0.08	-0.33 ± 0.07	-0.47 ± 0.18

CHAPTER 6. ISOSTATIC UPLIFT AS A DRIVER OF GLACIAL ADVANCES AFTER THE LAST GLACIAL MAXIMUM

ABSTRACT

Quaternary climate change triggered cycles of worldwide growth and subsequent decay of ice caps and mountain glaciers by causing temporal variations in temperature and precipitation. Glacial re-advances after the Last Glacial Maximum (LGM) were, however, not always associated with a pronounced cooling event, which raises the question about an alternative trigger. Here we show, using a combination of equilibrium line altitude (ELA) reconstructions for the European Alps and three-dimensional numerical modelling of glacioisostatic rebound, that post-LGM glacial advances in regions glaciated during the LGM were at least partially triggered by isostatic uplift that occurred in response to the removal of the LGM ice mass. Similar to a temperature drop, glacioisostatic uplift increases the accumulation area of glaciers and hence promotes their growth, but without requiring changes in temperature or precipitation. For the European Alps our models predict ~150 m of uplift between the LGM and the Younger Dryas epoch, which is equivalent to a temperature decrease of ~2°C. The resulting ~50% increase in the glacier accumulation area may explain the advance of glaciers up to the Younger Dryas, although these epochs were often associated with only a small temperature drop. Our findings imply that isostatic uplift can resolve the discrepancy between minimal cooling signals and post-LGM glacial advances and may explain their global spatiotemporal asynchronicity in timing and extent.

6.1. INTRODUCTION

Glacial advances after the LGM differed in timing and intensity both on a global and a regional scale and did not always occur in phase with a cooling event. This is best documented for the Younger Dryas, which lasted from ~12.9-11.7 ka BP (Rasmussen et al., 2006). For example, pollen data from New Zealand indicate the Younger Dryas advance of glaciers in the Southern Alps was not associated with a considerable temperature drop

(Singer et al., 1998; Rother and Shulmeister, 2006; Barrows et al., 2007). Similar evidence has been found in Scandinavia where the ice sheet advanced before the beginning of the relatively warm Younger Dryas (Birks and Ammann, 2000; Mangerud, 2004; Lohne et al., 2007). Mountain glaciers in the western USA generally started to advance before or early during the Younger Dryas and reached their maximum extent during the late Younger Dryas or even afterwards, as shown by radiocarbon dating of organic material buried beneath or overlying glacial deposits (Heine, 1998; Kovanen and Easterbrook, 2001) and cosmogenic nuclide dating of minimum moraine ages (Licciardi et al., 2004). In the European Alps, cosmogenic nuclide dating (Ivy-Ochs et al., 2006) has been used to date the moraines of post-LGM stadials. As noted by Lotter et al. (2000) for the case of the Younger Dryas, calculated temperature changes, based on pollen and chydorids, are smaller than those based
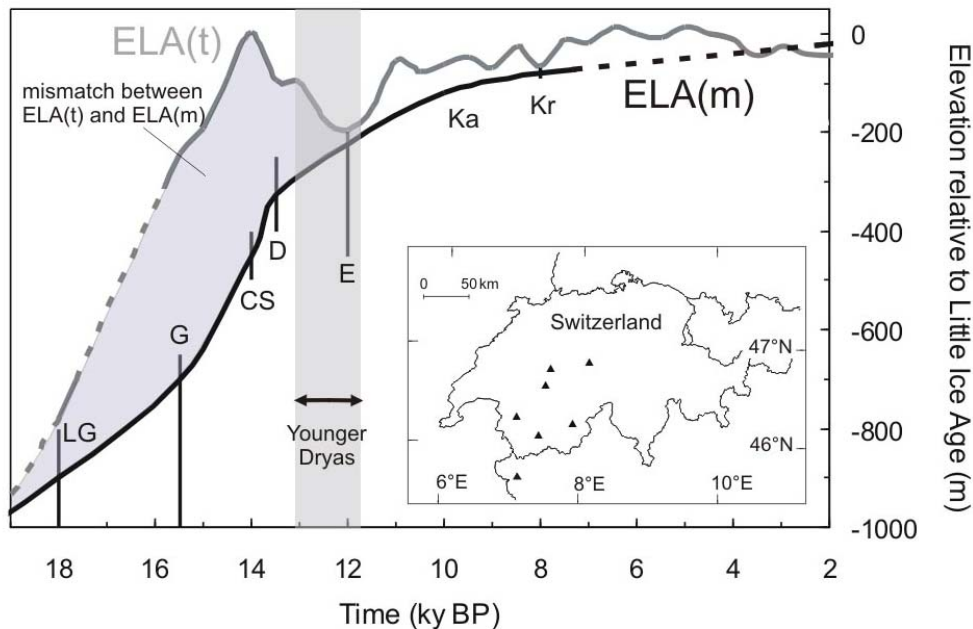
Figure 31: Diagram showing the discrepancy between two different estimates of the post-LGM equilibrium line altitude (ELA) in the European Alps. ELA(t), grey, was derived by compiling temperature proxies for the Alps and central Europe (Peyron et al., 1998; Lotter et al., 2000, Heiri et al., 2003; Heiri and Millet, 2005; Larocque and Finsinger, 2008; Kerschner and Ivy-Ochs, 2008) and converting them to altitude with a standard lapse rate of 65 m °C^{-1} (Vincent, 2002), $ELA(t) = \left[T_{(LIA)} - T_{(t)} \right] \times 65 m / °C$, based on the assumption of precipitation equal to or below modern levels (Kerschner and Ivy-Ochs, 2008). ELA(m), black, is based on the elevations of moraines throughout the Alps as calculated using the AAR method with a ratio of 0.65 between the glacier accumulation and ablation area (Ivy-Ochs, et al., 2006 and references therein), (note that the curve is of the maximum ELA(m) depression for advances in the dry Central Alps, and the lines are dashed where uncertain). Bars on the ELA(m) curve refer to the minimum and maximum ELA depression reported for the Kromer (Kr), Kartell, (Ka), Egesen (E), Daun (D), Clavadel/Senders (CS), Gschnitz (G), and Late glacial decay (LG) stadials as reported by Ivy Ochs et al. (2006). Both estimates are shown relative to Little Ice Age values. Inset map shows the climate study locations (black triangles).

on glacial-geomorphic evidence. Similar to the Younger Dryas in New Zealand and Scandinavia, glacial advances in the European Alps do not seem be triggered by temperature drop alone. This is revealed by comparing two different estimates of the equilibrium line altitude (ELA), which marks the boundary between the accumulation and ablation areas of a glacier. In principle, the ELA can be derived either from climate proxies, which can be converted to altitude using a lapse rate (ELA(t)), or from moraines (ELA(m)). In the case of purely climate-driven glacial advances, ELA(m) and ELA(t) are expected to be similar. However, in case of the European Alps, the curves of ELA(t) derived from chironomid and pollen data (Peyron et al., 1998; Lotter et al., 2000; Heiri et al., 2003; Heiri and Millet, 2005; Larocque and Finsinger, 2008) and ELA(m) derived from moraines (Ivy-Ochs et al., 2006) are not of similar magnitude between 18 and 12 ka BP (Fig. 1). Within this interval, ELA(m) is always considerably lower than ELA(t) and does not reflect the temperature fluctuations. From the onset of deglaciation through the Younger Dryas, the difference varies between 25 and 450 m (Figure 31).

6.1.1. Equilibrium line altitude discrepancies

The discrepancy between the temperature records and the magnitude of the glacial advances suggests that the growth of the glaciers during the post-LGM was triggered by an additional process. As increased precipitation can probably be excluded because precipitation during these stadials was lower than modern values in the central parts of the Alps (Kerschner and Ivy-Ochs, 2008), non-climate related drivers may play a role. Here we investigate if isostatic uplift of the lithosphere caused by deglaciation after the LGM may have promoted glacial re-advances by uplifting the mountains and enlarging glacier accumulation areas. Considerable isostatic uplift after the LGM has occurred in North America (Farrand, 1962) and Europe (Lambeck et al., 1998; Persaud and Pfiffner, 2004) but the effect of postglacial uplift on the size of glacier accumulation areas has not been addressed previously. We hypothesize that post-LGM uplift of the Alps could at least partially explain the mismatch between the two ELA curves. Isostatic uplift would cause a fall of the ELA(m) relative to the rising mountains by the same amount as the uplift, while its effect on the ELA(t) should be negligible. To test our hypothesis, we analyzed the spatiotemporal evolution of isostatic uplift of the European Alps between the LGM and Younger Dryas. This analysis involved two steps: the reconstruction of the LGM ice cover and three-dimensional numerical modelling to compute the uplift resulting from the decay of

this ice mass. To reconstruct the extent of the Alpine glaciers, we created a model of the LGM ice mass based on trimline elevation trends and the position of the ice margin, which together constrain the surface of the ice sheet (Jäckli, 1960; Florineth and Schlüchter, 1998; Kelly et al., 2006; Ivy-Ochs et al., 2006). The volume of the ice mass was then calculated by subtracting the ground elevation, based on the 3" SRTM dataset, from the altitude of the ice surface. Our preferred ice model (Figure 32a) yields an average ice thickness of 460 m, which is similar to the mean ice thickness of 500 m derived by Jäckli (1960) for the Swiss Alps.

6.2. FINITE-ELEMENT MODELING

In the second step we carried out finite-element modelling using the commercial software ABAQUS. The three-dimensional model comprises a 100-km-thick lithosphere, which is subdivided into an elastic 20-km-thick upper crust, a viscoelastic 20-km-thick lower crust and a viscoelastic 60-km-thick lithospheric mantle (Figure 32b). As the Alpine lithosphere probably has a strong lower crust (Schmid et al., 1996), we apply a viscosity of 1×10^{22} Pa s to this layer. The strength of the lithospheric mantle is, however, poorly constrained for the Alps. Following Jackson (2002), who argues for a weak lithospheric mantle beneath orogens like the Himalayas, we assume a viscosity of 1×10^{20} Pa s. For computational feasibility, the model does not take into account potential lateral variations in the rheological structure of the Alps. Gravity is included as a body force. To account for isostatic effects, a lithostatic pressure and an elastic foundation, which represents an asthenosphere with a density of $\rho = 3200$ kg/m^3, are applied at the bottom of the model. Dashpot elements at the bottom of model mimic the viscosity of the asthenosphere ($\eta = 1 \times 10^{19}$ Pa s). The model sides are fixed in all directions. All experiments start with the establishment of isostatic equilibrium before a pressure representing the LGM ice cover of the Alps is applied to the top of the model (Figure 32c). To account for the variable thickness of the Alpine ice mass, areas of same ice thickness on the model surface are defined such that the sum of the products of area and ice thickness equals the volume and mean ice thickness of our ice model. The temporal evolution of the pressure is adjusted to the glacial history of the Alps (Ivy-Ochs et al., 2006) and starts with a linear increase of the ice mass between 35 and
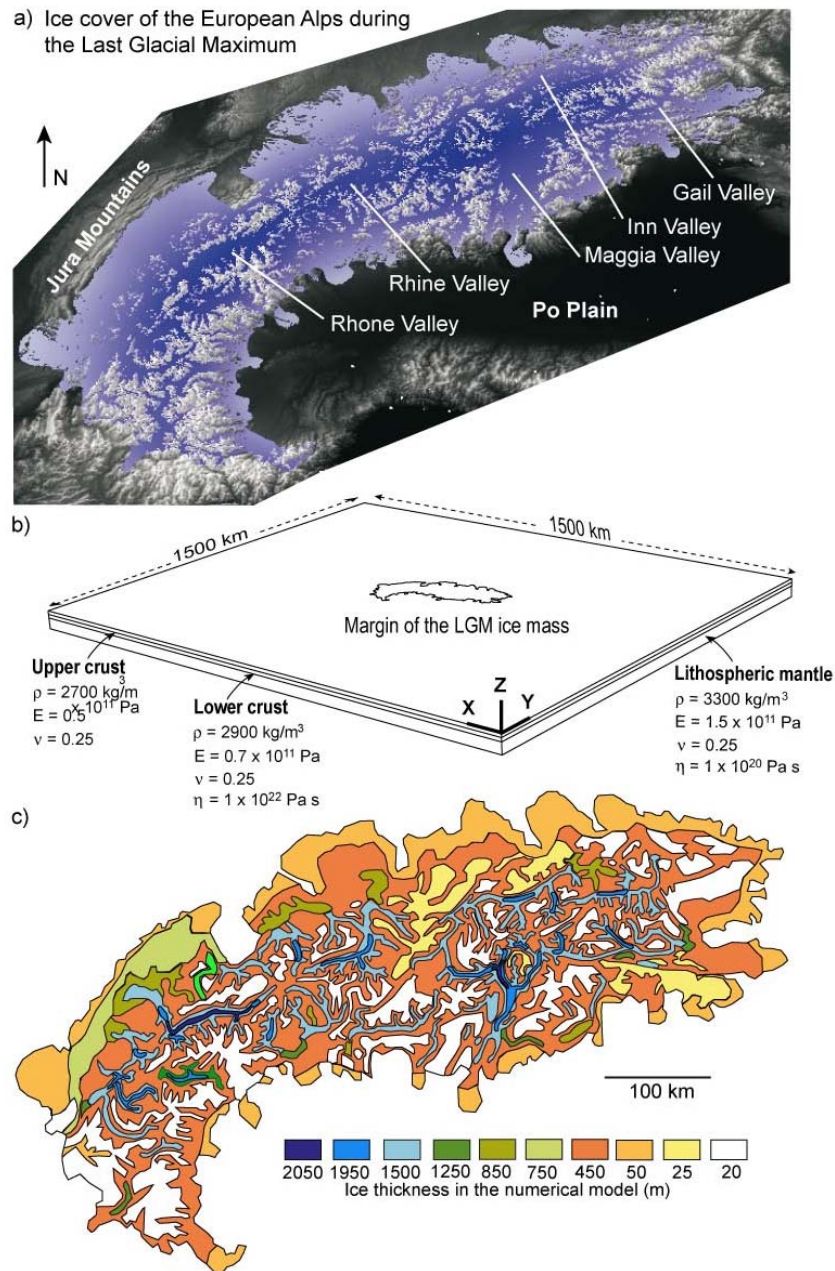
Figure 32: LGM ice cover of the European Alps. a) Perspective view of the ice mass as reconstructed based on trimlines and moraines at the ice margin (Jäckli, 1960; Florineth and Schlüchter, 1998; Kelly et al., 2006). b) Perspective view of the finite-element model. Rheological parameters are density (ρ), elastic modulus (E), Poisson's ratio (ν) and viscosity (η). The edge length of the elements is ~1 km in the model center where the load is applied and increases to ~20 km to the model sides. c) Representation of the LGM ice mass in the European Alps as areas of same ice thickness on top of the finite-element model.

26 ka BP. Until 21 ka BP, the load is at its maximum. Between 21 and 18 ka BP, all ice in the areas representing the Alpine foreland as well as two-thirds of the glaciers in the Alps is removed. All remaining ice is removed by 15 ka BP, which reflects that Alpine passes and valleys were probably ice free by 15-14 ka BP (Welten, 1982; Kelly, et al., 2004; Ivy-Ochs, et al., 2006).

6.3. RESULTS

The model results show that removal of the LGM ice mass causes up to 151 m of uplift until 13 ka BP, i.e. the beginning of the Younger Dryas (Figure 33a). The temporal evolution of the vertical displacement at a point P that is located on the surface of the model shows that uplift occurs at an average rate of ~19 mm/a between 21 and 13 ka BP (Figure 33b). After the complete removal of the ice cover, the uplift rate decreases gradually owing to the presence of the viscous layers and is 0.2 mm/a at the end of the model run, i.e. today. The amount of uplift predicted by our model (~150 m) can account for ~30% of the ELA mismatch for the early post-LGM stadials (Figure 31) and is equal to the mismatch between ELA(m) and ELA(t) when the latter reaches its minimum during the Younger Dryas (Figure 31). In comparison, the calculated uplift of the central Alps would have the same effect as a temperature decrease by up to 2°C, using an ELA lapse rate of 65 m °C^{-1} (Vincent, 2002). This means that uplift allows the local air temperatures to remain warmer than in previous scenarios and hence resolves the discrepancy between the inferred temperature drop and the larger extent of the post-LGM valley glaciers. To illustrate the effect of isostatic uplift on the glacial system, we estimate the increase in the glacier accumulation area resulting from a maximum of 150 m of isostatic uplift of the European Alps. We use the change in the total area of the orogen above the ELA(m) as a proxy, which yields a maximum estimate of the additional glacier accumulation area. To calculate the change in the total area above the ELA, we corrected the modern landsurface for rebound and subtracted the model results at 21 and 13 ka BP from the DEM. Total area above the ELA is then the difference between the ELA and the paleoelevation dataset. The results of our analysis show the aerial increase due to isostatic uplift between the LGM and the Younger Dryas is 1950 km^2 (Figure 33c). This represents a 50% increase in glacier accumulation area by postglacial uplift alone and results
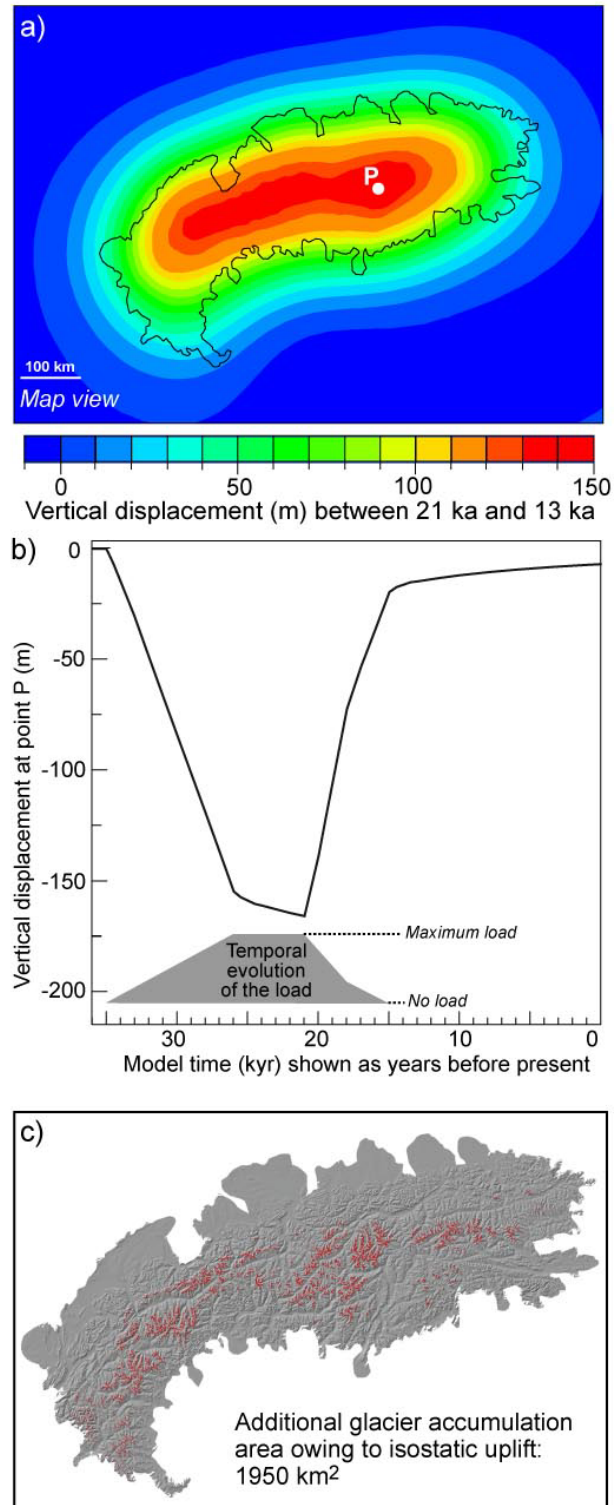
Figure 33: a) Calculated isostatic uplift between 21 ka and 13 ka of the European Alps resulting from deglaciation after the LGM. Margin of the LGM ice cover is indicated by a black line. b) Temporal evolution of the vertical displacement at point P (location of P is indicated in a). c) Map showing the additional area above the ELA (shown in red) owing to uplift of the Alps between the end of the LGM and the beginning of the Younger Dryas. The aerial increase of 1950 km^2 represents a 50% increase in accumulation area.

in a strongly positive mass balance, which, in concert with the beginning temperature drop (Figure 31), should promote the advance of the ice front.

The pronounced spatial variation in the isostatic uplift of the Alps, as suggested by our model results, provides a lucid explanation why dates of the Younger Dryas and other post-LGM advances in the Alps show considerable variability (Ivy-Ochs et al., 2006). Given that this deglaciation-induced uplift is probably amplified by glacial erosion (Champagnac et al., 2007) and sediment transport to the foreland basins (Hinderer, 2001), it is likely that uplift-induced increase in the accumulation areas of glaciers played a role in triggering the Younger Dryas and the other post-LGM glacial advances in the Alps. Furthermore, the temporal evolution of isostatic uplift may explain why some regions in the Alps like the Grimsel Pass remained ice-covered until 14 to 11.3 ka BP (Ivy-Ochs et al., 2006). Most uplift occurred shortly after the onset of deglaciation and may hence have provided a
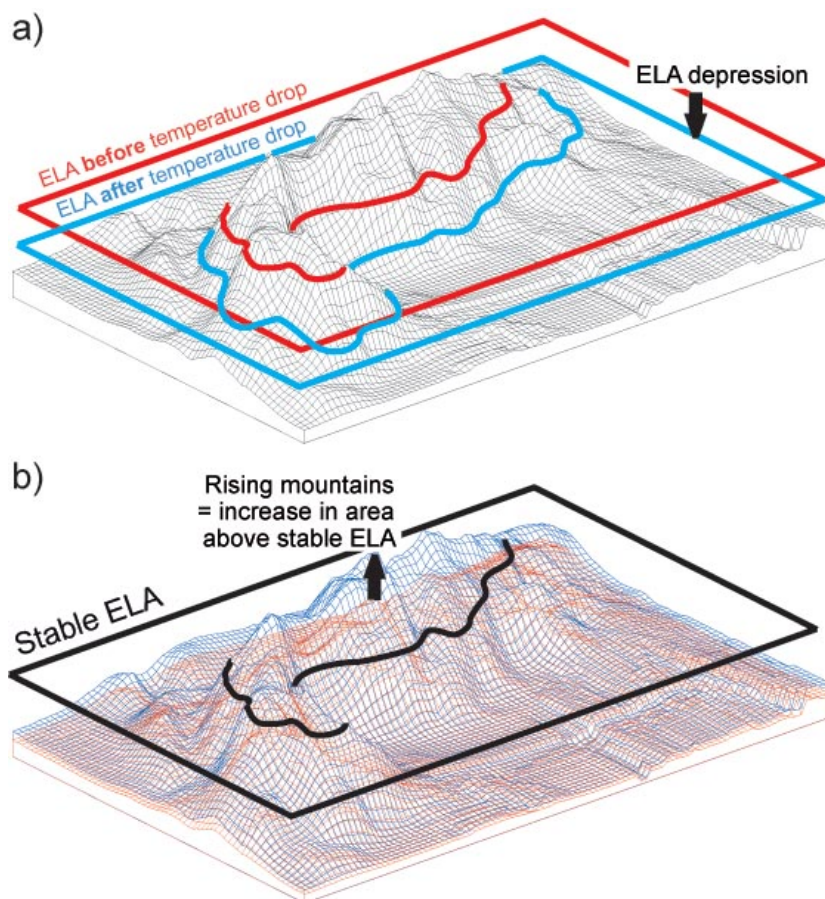
Figure 34: Possible explanations for the depression of the ELA. a) Traditional view: The depression of the ELA is caused by a decrease in the temperature. b) Mechanism proposed by this study: Isostatic uplift of a mountain range relative to a stable ELA causing an increase in the glacier accumulation area. This corresponds to a relative lowering of the ELA with respect to the rising mountains, which is not associated with changes in temperature or precipitation conditions.

counterbalance to the rapidly rising temperatures, with the result that the existence of glaciers in the central Alps was prolonged. We speculate that the ELA(m) curve actually reflects this competition between temperature increase over post-glacial timescales and isostatic uplift because it always remains lower than the ELA(t) and shows a lagged increase that may be interpreted as a signal of the isostatic uplift on the valley glaciers as recorded by the position of moraines.

6.4. CONCLUSION

In conclusion, our study provides evidence that postglacial uplift may have been an important driver of the post-LGM glacial advances. It extends the traditional view that glaciers grow mainly due to a climate-driven ELA depression (Figure 44a) by showing that the rise of mountain ranges relative to a stable ELA has a similar effect (Figure 44b). As a consequence, the beginning of the post-LGM glacial phases does not necessarily correspond to the degrading climatic conditions that are recorded in ice cores (Shakun et al., 2007), but could predate the cooling events. Glaciers within individual mountain ranges may not be uplifted at the same rate and therefore asynchronous advances should be common phenomenon, despite a globally synchronous climate change.

REFERENCES CITED

Ahnert F. 1970. Functional relationship between denudation, relief and uplift in large mid-latitude drainage basins. *American Journal of Science* **268,** 243-263.

Allkofer O. 1975. Introduction to cosmic radiation. Verlag Karl Thiemig, Munich, 221 p.

Amundson R., Richter D., Humphreys G., Jobbagy E. and Gaillardet J. 2007. Coupling between biota and Earth materials in the critical zone. *Elements* **3**, 327-332.

Anderson S, Drever J, Frost C and Holden P. 2000. Chemical weathering in the foreland of a retreating glacier. *Geochimica et Cosmochimica Acta* **64**, 1173-1189.

April R., Newton R. and Coles L. 1986. Chemical weathering in two Adirondack watersheds: past and present-day rates. *Geological Society of America Bulletin* **97**, 1143-1158.

Auer, M., 2003. Regionalisierung von Schneeparametern - Eine Methode zur Darstellung von Schneeparametern im Relief. Unpublished Masters Thesis. Universitaet Bern, Bern, 97 pp.

Bain D., Mellor A., Robertson-Rintoul M., and Buckland S. 1993. Variations in weathering processes and rates with time in a chronosequence of soils from Glen Feshie, Scotland. *Geoderma* **57**, 275-293.

Bard, E., Hamelin, B., Fairbanks, R G. and Zindler, A. 1990. Calibration of the C-14 timescale over the past 30,000 years using mass spectrometric U-Th. *Nature* **345**, 405-410.

Barrows, T., Lehman, S., Fifield, L. and Deckker, P. 2007. Absence of cooling in New Zealand and the adjacent ocean during the Younger Dryas chronozone. *Science* **318**, 86-88.

Beer, J., Raisbeck, G.M. and Yiou, F., 1991. Time variations of [10]Be and solar activity. *In The Sun in Time,* (eds, Sonnett, C.P., Giampapa, M.S. and Mathews, M.S.) The University of Arizona Press, Tucson, pp. 343–359

Berner, R.A., Lasage, A.C. and Garrels, R.M. 1983. The carbonate-silicate geochemical cycle and its effect on atmospheric carbon dioxide over the past 100 million years. *American Journal of Science* **283**, 641-683.

Bierman P. and Steig E. 1996.Estimating rates of denudation using cosmogenic isotope abundances in sediment. *Earth Surface Processes and Landforms* **21**, 125-139.

Bierman, P., Nichols, K., 2004. Rock to sediment - slope to sea with [10]Be - rates of landscape change. *Annual Reviews in Earth and Planetary Sciences* **32**, 215-255, doi:10.1146/annurev.earth.32.101802.120539

Binnie S., Phillips W., Summerfield, M.A. and Fitfield, L.K. 2007, Tectonic uplift, threshold hillslopes, and denudation rates in a developing mountain range: *Geology* **35**, 743-746.

Birks, H.H. and Ammann, B. 2000. Two terrestrial records of rapid climatic change during the glacial-Holocene transition (14,000-9,000 calendar years B.P.) from Europe. *Proc. Nat. Acad. Sci.* **97**, 1390-1394.

Brady, P. and Carrol, S. 1994. Direct effects of CO_2 and temperature on silicate weathering: possible implications for climate control. *Geochimica Cosmochimica Acta* **58**, 1853-1863.

Braun, J., Heimsath, A., Chappell, J. 2001. Sediment transport mechanisms on soil-mantled hillslopes. *Geology* **29**, 683-686.

Brimhall, G.H. and Dietrich, W.E. 1987. Constitutive mass balance relations between chemical composition, volume, density, porosity, and strain in metasomatic hydrochemical systems: Results on weathering and pedogenesis. *Geochimica et Cosmochimica Acta* **51**, 567-587

Brocard, G., van der Beek, P., Bourles, D., Siame, L., Mugnier, J., 2003. Long-term fluvial incision rates and postglacial river relaxation time in the French Western Alps from [10]Be dating of alluvial terraces with assessment of inheritance, soil development and wind ablation effects. *Earth and Planetary Science Letters* **209**, 197-214.

Brown, E., Edmond, J., Raisbeck, G., Yiou, F., Kurz, M. and Brook E. 1991. Examination of surface exposure ages of Antarctic moraines using in situ-produced [10]Be and [26]Al. *Geochimica et Cosmochimica Acta* **55**, 2269-2283.

Brown, E., Stallard, R., Larsen, M., Raisbeck, G. and Yiou, F. 1995. Denudation rates determined from the accumulation of in situ- produced [10]Be in the Luquillo experimental forest, Puerto Rico. *Earth and Planetary Science Letters* **129**, 193-202.

Burbank, D., Leland, J., Fielding, E., Anderson, R., Brozovic, N., Reid, M. and Duncan C. 1996. Bedrock incision, rock uplift and threshold hillslopes in the northwestern Himalayas. *Nature* **379**, 505-510.

Burrough, P.A. and McDonnell, R. 1998. Principles of geographical information systems. Oxford University Press. Oxford, 333p.

Burke, B., Heimsath, A. and White, A. 2007. Coupling chemical weathering with soil production across soil-mantled landscapes. *Earth Surface Processees and Landforms* **32**, 853-873.

Champagnac, J., Molnar, P., Anderson, R., Sue, C. and Delacou, B. 2007. Quaternary erosion-induced isostatic rebound in the Western Alps. *Geology* **35,** 195-198.

Chadwick, O., Brimhall, G. and Hendricks, D. 1990. From black box to a grey box: a mass balance interpretation of pedogenesis. *Geomorphology* **3**, 369-390.

Chen-Feng, Y., Lee T., Brown, L., Shen, J. and Ju-Chin C. 1988. [10]Be study of rapid erosion in Taiwan: *Geochimica et Cosmochimica Acta*, **52**, 2687-2691.

Clapp, E., Bierman, P., Caffee, M. 2002. Using [10]Be and [26]Al to determine sediment generation rates and identify sediment source areas in an arid region drainage basin. *Geomorphology* **45**, 89-104.

Clark, M., Maheo, G., Saleeby, J. and Farley, K. 2005. The non-equilibrium landscape of the southern Sierra Nevada, California. *GSA Today* **15**, 4-10.

Cleaves, E. 1993. Climatic impact on isovolumetric weathering of a coarse-grained schist in the Northern Piedmont province of the Central Atlantic states. *Geomorphology* **8**, 191-198.

Codilean, A. 2006. Calculation of the cosmogenic nuclide production topographic shielding scaling factor for large areas using DEMs. *Earth Surface Process and Landforms* **31**, 785-794.

Dethier, D. and Lazarus, E. 2006. Geomorphic inferences from regolith thickness, chemical denudation and CDR erosion rates near the glacial limit, Boulder Creek catchment and vicinity, Colorado. *Geomorphology* **75**, 384-399.

Dorsey, R. and Roering, J., 2006. Quaternary landscape evolution in the San Jacinto fault zone, Peninsular Ranges of Southern California: transient response to strike-slip fault initiation. *Geomorphology* **73**, 16-32.

Dunai, T.J. 2000. Scaling factors for production rates of in situ produced cosmogenic nuclides: a critical reevaluation. *Earth and Planetary Science Letters* **176**,157-169.

Dunai, T.J. 2001. Influence of secular variation on the geomagnetic field on production rates of in situ produced cosmogenic nuclides. *Earth and Planetary Science Letters* **193**, 197-212.

Dunai, T.J., et al. 2005.CRONUS-EU. Cosmic ray produced nuclide systematics - The European contribution. *Geochim. Cosmochim. Acta* **69**, A165.

Dunne, J., Elmore, D. and Muzikar, P. 1999. Scaling factors for the rates of production of cosmogenic nuclides for geometric shielding and attenuation at depth on sloped surfaces. *Geomorphology* **27**, 3-11.

Eco, U. 1994. On the impossibility of drawing a map of the empire on a scale of 1 to 1. In *How to travel with a salmon*. Harcourt Brace and Company, Orlando, 95-106.

Farrand, W. 1962. Postglacial uplift in North America. *Am. J. Sci.* **260**, 181-199.

Florineth, D. and Schlüchter, C. 1998. Reconstructing the last glacial maximum (LGM) ice surface geometry and flowlines in the Central Swiss Alps. *Eclogae Geologicae Helvetiae* **91**, 391-407.

Frank, M., Schwarz, B., Baumann, S. Kubik, P., Suter, M. and Mangini, A. 1997. A 200 kyr record of cosmogenic radionuclide production rate and geomagnetic field intensity from [10]Be in globally stacked deep sea sediments: *Earth and Planetary Science Letters* **149**, 121-129.

References Cited

Frisch, W., Kuhlemann, J., Dunkl, I. and Brügel, A. 1998. Palinspastic reconstruction and topographic evolution of the Eastern Alps during late Tertiary extrusion. *Tectonophysics* **297**, 1–15.

Furbish, D. and Fagherazzi, S. 2001. Stability of creeping soil and implications for hillslope evolution. *Water Resources Research* **37**, 2607-2618.

Georg, R.B., Reynolds, B.C., Frank, M. and Haliday, A.N. 2006. Mechanisms controlling the silicon isotopic composition of river waters. *Earth and Planetary Science Letters* **249**, 290-306.

Gosse, J. and Phillips, F. 2001. Terrestrial in situ cosmogenic nuclides: theory and application. *Quaternary Science Reviews* **20**, 1475-1560.

Granger, D.E. and Muzikar, P. 2001. Dating sediment burial with in situ-produced cosmogenic nuclides: theory, techniques, and limitations. *Earth and Planetary Science Letters* **188**, 269-281.

Granger D.E. and Riebe, C.S. 2007. Cosmogenic nuclides in weathering and erosion. *In Surface and Ground Water, Weathering, and Soils* (ed. J.I. Drever) *Treatise on Geochemistry* **5** (eds. H.D. Holland and K.K. Turekian), Elsevier-Pergamon, Oxford, 1-40.

Granger, D.E. and Smith, A. 2000. Dating buried sediments using radioactive decay and muogenic production of ^{26}Al and ^{10}Be. *Nuclear Instruments and Methods in Physics Research B* **172**, 822-826.

Granger, D.E., Kirchner, J. and Finkel, R. 1996. Spatially averaged long-term erosion rates measured from in situ-produced cosmogenic nuclides in alluvial sediment. *Journal of Geology* **104**, 249-257.

Granger, D.E., Kirchner, J.W. and Finkel, R.B. 1997. Quaternary downcutting rate of the New River, Virginia, measured from differential decay of cosmogenic ^{26}Al and ^{10}Be in cave-deposited alluvium. *Geology* **25,** 107-110.

Green, E., Dietrich, W. and Banfield, J. 2006. Quantification of chemical weathering rates across an actively eroding hillslope. *Earth and Planetary Science Letters* **242**, 155-169.

Greenlee, D.D. 1987. Raster and vector processing for scanned linework. *Photogrammetric Engineering and Remote Sensing* **53**, 1383-1387.

Gudmundsson, G.H. 1994. An order-of-magnitude estimate of the current uplift-rates in Switzerland caused by the Würm Alpine deglaciation, *Eclogae Geologicae Helvetiae* **87,** 545-557.

Hancock, G.S., Anderson, R.S., Chadwick, O.A., and Finkel, R.C. (1999) Dating fluvial terraces with ^{10}Be and ^{26}Al profiles, Wind River, Wyoming. *Geomorphology* **27,** 41-60.

Harrois, L. and Moore, J. 1988. The C.I.W. index: a new chemical index of weathering. *Sedimentary Geology* **55,** 319-322.

Hayakawa, Z. and Oguchi, T. 2006. DEM-based identification of fluvial knickzones and its application to Japanese mountain rivers. *Geomorphology* **78**, 90-106.

Heimsath, A., Chappell, J., Dietrich, W., Nishiizumi, K. and Finkel, R. 2000. Soil production on a retreating escarpment in southeastern Australia. *Geology* **28**, 787-790.

Heimsath, A., Chappell, J., Dietrich, W., Nishiizumi, K. and Finkel, R. 2001a. Late Quaternary erosion in southeastern Australia: a field example using cosmogenic nuclides. *Quaternary International* **82-85**, 169-185.

Heimsath, A., Dietrich, W., Kunihiko, M. and Finkel, R. 1997. The soil production function and landscape equilibrium. *Nature* **388**, 358-361.

Heimsath, A., Dietrich, W., Nishiizumi, K. and Finkel, R. 1999. Cosmogenic nuclides, topography, and the spatial variation of soil depth. *Geomorphology* **27**, 151-172.

Heimsath, A., Dietrich, W., Nishiizumi, K. and Finkel, R. 2001b. Stochastic processes of soil production and transport: erosion rates, topographic variation and cosmogenic nuclides in the Oregon Coast Range. *Earth Surface Processes and Landforms* **26**, 531-552.

Heimsath, A., Furbish, D. and Dietrich, W. 2005. The illusion of diffusion: field evidence for depth-dependent sediment transport. *Geology* **33**, 949-952.

Heine, J. 1998. Extent, timing, and climatic implications of glacier advances Mount Rainier, Washington, U.S.A., at the Pleistocene/Holocene transition. *Quat. Sci. Rev.* **17**, 1139-1148.

Heiri, O., Lotter, A., Hausmann, S. and Kienast, F. 2003. A chironomid-based Holocene summer air temperature reconstruction from the Swiss Alps. *The Holocene* **13**, 477-484.

Heiri, O. and Millet, L. 2005. Reconstruction of Late Glacial summer temperatures from chironomid assemblages in Lac Lautrey (France). *J. Quat. Sci.* **20**, 33-44.

Heisinger, B., Lal, D., Jull, A.J.T., Kubik, P.W., Ivy-Ochs, S., Neumaier, S., Knie, K., Lazarev V. and Nolte, E. 2002a. Production of selected cosmogenic radionuclides by muons: 1. Fast muons. *Earth Planet. Sci. Lett.* **200**, 345–355.

Heisinger, B., Lal, D., Jull, A.J.T., Kubik, P.W., Ivy-Ochs, S., Knie, K. and Nolte, E. 2002b. Production of selected cosmogenic radionuclides by muons: 2. Capture of negative muons. *Earth Planet. Sci. Lett.* **200**, 357–369.

Hewawasam, T., von Blanckenburg, F., Schaller, M. and Kubik, P.K. 2003. Increase of human over natural erosion rates in tropical highlands constrained by cosmogenic nuclides. *Geology* **31**, 597-600.

Hinderer, M. 2001. Late Quaternary denudation of the Alps, valley and lake fillings and modern river loads. *Geodinamica Acta* **14**, 231-263.

Hormes A, Müller, B. and Schlüchter, C. 2001. The Alps with little ice: evidence for eight Holocene phases of reduced glacier extent in the Central Swiss Alps. *The Holocene* **11**, 255-265. DOI: 10.1191/095968301675275728.

Hosein, R., Arn, K., Steinmann, P., Adatte, T. and Foellmi, K. 2004. Carbonate and silicate weathering in two presently glaciated, crystalline catchments in the Swiss Alps. *Geochimica et Cosmochimica Acta* **68**, 1021-1033.

Iacumin, P. and Quercioli, C. 1993. A new technique for quantitative separation of quartz from feldspars. *European Journal of Mineralogy* **3**, 677-678.

Ivy-Ochs, S., Schlüchter, C., Kubik, P.W., Synal, H.A., Beer, J. and Kerschner, H. 1996. The exposure age of an Egesen moraine at Julier Pass, Switzerland, measured with the cosmogenic radionuclides 10Be, 26Al and 36Cl. *Eclogae Geologicae Helvetiae* **89**, 1049–1063.

Ivy-Ochs, S., Schaefer, J., Kubik, P., Synal, H., Schlüchter, C. 2004. Timing of deglaciation on the northern Alpine Foreland (Switzerland). *Eclogae Geologicae Helvetiae* **97**, 47-55.

Ivy-Ochs, S., Kerschner, H., Reuther, A., Maisch, M., Sailer, R. et al. 2006. The timing of glacier advances in the northern European Alps based on surface exposure dating with cosmogenic [10]Be, [26]Al, [36]Cl, and [21]Ne. *Geol. Soc. Am. Spec. Paper* **415**, 43-60.

Jäckli A. 1970. Die Schweiz zur letzten Eiszeit. Atlas der Schweiz Blatt 6, Bundesamt für Landestopographie, Wabern-Bern.

Jackson, J. 2002. Strength of the continental lithosphere: Time to abandon the jelly sandwich? *GSA Today* **12(9)**, 4-10.

Jenson, S.K. and Domingue, J.O. 1988. Extracting topographic structure from Digital Elevation Data for Geographic Information Systems. *Photogrammetric Engineering and Remote Sensing* **54(11)**, 1593-1600.

Joerin, U.E., Stocker, T.F., and Schlüchter, C., 2006. Multicentury glacier fluctuations in the Swiss Alps during the Alps. *The Holocene*, **16**. 697-704.

Kahle, H., Geiger, A., Buerki, B., Gubler, E., Marti, U., Wirth, B., Rothacher, M., Gurtner, W., Beutler, G., Bauersima, I. and Pfiffner, O.E.A. 1997. Recent crustal movements, geoid and density distribution: contribution from integrated satellite and terrestrial measurements. In *Results of the National Research Program 20 (NRP 20)*. Pfiffner O.E.A. (Ed.). 251-259.

Kelly, M., Buoncristiani, J. and Schlüchter, C. 2004, A reconstruction of the Last Glacial Maximum (LGM) ice-surface geometry in the western Swiss Alps and contiguous Alpine regions in Italy and France. *Eclogae Geologicae Helvetiae* **97**, 57-75.

Kelly, M., Ivy-Ochs, S., Kubik, P., von Blanckenburg, F. and Schlüchter, C. 2006. Chronology of deglaciation based on [10]Be dates of glacial erosional features in the Grimsel Pass region, Central Swiss Alps. *Boreas* **35**, 634-643.

Kerschner, H. and Ivy-Ochs, S. 2008. Palaeoclimate from glaciers: examples from the Eastern Alps during the Alpine Lateglacial and early Holocene. *Global and Planetary Change* **60**, 58-71.

Kirby, K., Johnson, C., Furlong, K., Heimsath, A., 2007. Transient channel incision along Bolinas Ridge, California: evidence for differential rock uplift adjacent to the San Andreas Fault. *Journal of Geophysical Research* **112**, F03S07.

Kirchner, J., Finkel, R., Riebe, C., Granger, D., Clayton, J., King, J. and Megahan, W. 2001. Mountain erosion over 10 yr, 10 k.y., and 10 m.y. time scales: *Geology* **29**, 591-594.

Kirkwood, S. and Nesbitt, H. 1991. Formation and evolution of soils from an acidified watershed: Plastic Lake, Ontario, Canada. *Geochimica Cosmochemica Acta* **55**, 1793-1806.

Kohl, C. and Nishiizumi, K. 1992. Chemical isolation of quartz for measurement of in situ-produced cosmogenic nuclides. *Geochimica et Cosmochimica Acta* **56**, 3583-3587.

Korup, O. 2006. Rock-slope failure and the river long profile. *Geology* **34**, 45-48.

Kovanen, D. and Easterbrook, D. 2001. Late Pleistocene, post-Vashon, alpine glaciation of the Nooksack drainage, North Cascades, Washington. *GSA Bull.* **113**, 274-288.

Kubik, P.W., Ivy-Ochs, S., 2004. A re-evaluation of the 0-10 ka ^{10}Be production rate for exposure dating obtained from the Koefels (Austria) landslide. *Nuclear Instruments and Methods in Physics Research, Section B: Beam Interactions with Materials and Atoms* **223-224**, 618-622.

Kubik, P.K., Ivy-Ochs, S., Masarik, J., Frank, M. and Schlüchter C. 1998. ^{10}Be and ^{26}Al production rates deduced from an instantaneous event within the dendro-calibration curve, the landslide of Koefels, Oetz valley, Austria. *Earth and Planetary Science Letters* **161**, 231-241.

Kurz, M. 1986. Cosmogenic helium in a terrestrial igneous rock: *Nature* **320**, 435-439.

Lal D. 1991. Cosmic ray labeling of erosion surfaces: in situ nuclide production rates and erosion models. *Earth and Planetary Science Letters* **104**, 424-439.

Lal, D. and Peters, B. 1967. Cosmic ray-produced radioactivity on the Earth. In *Handbuch der physik*. Fluegge S (Ed.). 551-612.

Lambeck, K., Smither, C. and Johnston, P. 1998. Sea-level change, glacial rebound and mantle viscosity for northern Europe. *Geophys. J. Int.* **142**, 102-144.

Larocque, I. and Finsinger, W. 2008. Late-Glacial chironomid-based temperature reconstructions for Lago Piccolo di Avigliana in the southwestern Alps (Italy). *Palaeogeogr. Palaeoclimatol. Palaeoecol.* **257**, 207-223.

Laubsher, H.P. 1992. Jura kinematics and the Molasse Basin, *Eclogae Geologicae Helvetiae* **85**, 287-303.

Licciardi, J., Clark, P., Brook, E., Elmore, D. and Sharma, P. 2004. Variable responses of western U.S. glaciers during the last deglaciation. *Geology* **32**, 81-84.

Lifton, N.A., Jull, A.J.T. and Quade, J. 2001. A new extraction technique and production rate estimate for in situ cosmogenic ^{14}C in quartz. *Geochimica et Cosmochimica Acta* **65**, 1953-1969.

Lohne, O., Bondevik, S., Mangerud, J. and Svendsen, J. 2007. Sea-level fluctuations imply that the Younger Dryas ice-sheet expansion in western Norway commenced during the Allerød. *Quat. Sci. Rev.* **26**, 2128-2151.

Lotter, A., Birks, H., Eicher, U., Hofmann, W., Schwander, J. et al. 2000. Younger Dryas and Allerod summer temperatures at Gerzensee (Switzerland) inferred from fossil pollen and cladoceran assemblages. *Paleogeogr. Palaeoclimatol. Palaeoecol.* **159**, 349-361.

Mangerud, J. 2004. Ice sheet limits on Norway and the Norwegian continental shelf. in Ehlers, J. and Gibbard, P. (Eds.). *Quaternary Glaciations – Extent and Chronology. Vol. 1. Europe*, Elsevier, Amsterdam, 271-294.

Masarik, J., Frank, M., Schaefer, J. and Wieler, R. 2001. Correction of in situ cosmogenic nuclide production rates for geomagnetic field intensity variations during the past 800,000 years. *Geochimica et Cosmochimica Acta* **65**, 2995-3003.

Matmon, A., Bierman, P., Larsen, J., Southworth, S., Pavich, M. and Caffee, M. 2003a. Temporally and spatially uniform rates of erosion in the southern Appalachian Great Smoky Mountains. *Geology* **31**, 155-158.

Matmon, A., Bierman, P., Larsen, J., Southworth, S., Pavich, M., Finkel, R. and Caffee, M. 2003b. Erosion of an ancient mountain range, the Great Smoky Mountains, North Carolina and Tennessee. *American Journal of Science* **303**, 817-855.

Matter A, 1964. Sedimentologische Untersuchungen im östlichen Napfgebiet (Entlebuch- tal der Grossen Fontanne, Kt. Luzern). *Eclogae Geologicae Helvetiae* **57**, 315-428.

Montgomery, D., Foufoula-Georgiou, E. 1993. Channel network source representation using digital elevation models. *Water Resources Research* **29**, 3925-3934.

Montgomery, D. 2001, Slope distributions, threshold hillslopes, and steady-state topography. *American Journal of Science* **301**, 432-454.

Montgomery, D. and Brandon, M. 2002. Topographic controls on erosion rates in tectonically active mountain ranges. *Earth and Planetary Science Letters* **201**, 481-489.

Montgomery, D. 2002. Valley formation by fluvial and glacial erosion. *Geology* **30**, 1047-1050.

Morel, P., von Blanckenburg, F., Schaller, M., Kubik, P.K. and Hinderer, M., 2003. Lithology, landscape dissection and glaciation controls on catchment erosion as determined by cosmogenic nuclides in river sediment (the Wutach Gorge, Black Forest). *Terra Nova* **15**, 398-404.

Mudd, S.M. and Furbish, D. 2005. Lateral migration of hillcrests in response to channel incision in soil-mantled landscapes. *Journal of Geophysical Research* **110**, F04026.

Mudd S.M. and Furbis, D. 2007. Responses of soil-mantled hillslopes to transient channel incision rates: *Journal of Geophysical Research*, **112**, F03S18.

Müller, B. and Schlüchter, C., 1997. Zur Stellung der Zeller Schotter in der Alpinen Eiszeiten-Chronologie und ihre stratigraphische Beziehung zu den Schieferkohlen von Gondiswil. *Eclogae Geologicae Helvetiae* **90**, 211-227.

Nesbitt, H. and Young, G. 1982. Early Proterozoic climates and plate motions inferred from major element chemistry of lutites. *Nature* **299**, 715-717.

Nishiizumi, K., Winterer, E., Kohl, C., Klein, J., Middleton, R., Lal, D. and Arnold, J. 1989. Cosmic ray production rates of ^{10}Be and ^{26}Al in quartz from glacially polished rocks. *Journal of Geophysical Research* **94**, 17907-17915.

Nishiizumi, K., Lal, D., Klein, J., Middleton, R. and Arnold, J. 1986. Production of ^{10}Be and ^{26}Al by cosmic rays in terrestrial quartz in situ and implications for erosion rates. *Nature*, **319**, 134-136.

Norton, K.P., von Blanckenburg, F., Schlunegger, F., Schwab, M., and Kubik, P.W. 2008. Cosmogenic nuclide-based investigation of spatial erosion and hillslope channel coupling in the transient foreland of the Swiss Alps. *Geomorphology* **95**, 474-486. doi:10.1016/j.geomorph.2007.07.013

Norton, K.P. and Vanacker, V. in press. Effects of terrain smoothing on topographic shielding correction factors for cosmogenic nuclide-derived estimates of basin-averaged denudation rates: *Earth Surface Processes and Landforms*. doi: 10.1002/esp.1700

Oliva, P., Vries, J. and Dupre, B. 2003. Chemical weathering in granitic terrains. *Chemical Geology* **202**, 225-256.

Onuchin A and Burenina T. 1996.Climatic and geographic patterns in snow density dynamics, northern eurasia. *Arctic and Alpine Research* **28**, 99-103.

Pavich, M. 1986. Processes and rates of saprolite production and erosion on a foliated granitic rock of the Virginia Piedmont. Dethier, S. and Coleman, D. (Eds.). Academic Press.

Pazzaglia, F., Brandon, M., 2001. A fluvial record of long-term steady-state uplift and erosion across the Cascadia Forearc High, western Washington state. *American Journal of Science* **301**, 385-431.

Perg, L.A., Anderson, R.S. and Finkel, R.C. 2001. Use of a new ^{10}Be and ^{26}Al inventory method to date marine terraces, Santa Cruz, California, USA. *Geology* **29**, 879-882.

Persaud, M. and Pfiffner, O. 2004. Active deformation in the Eastern Swiss Alps: post-glacial faults, seismicity and surface uplift. *Tectonophysics* **385,** 59-84.

Peyron, O., Guiot, J., Cheddadi, R., Tarasov, P., Reille, M. et al. 1998. Climatic reconstruction in Europe for 18,000 yr B.P. from pollen data. *Quat. Res.* **49**, 183-196.

Pfiffner, O.A., Frei, W., Valasek, P., Stäuble, M., Levato, L., Dubois, L., Schmid, SM. and Smithson, S.B. 1990. Results from deep seismic reflection profiling in the Eastern Swiss Alps, line NFP 20-East. *Tectonics* **9**, 1327-1355.

Pratt-Sitaula, B., Burbank, D., Heimsath, A., Ojha, T. 2004. Landscape disequilibrium on 1000-10,000 year scales Marsyandi River, Nepal, central Himalaya. *Geomorphology* **58**, 223-241.

Rabus, B., Eineder, M., Roth, A. and Bamler, R. 2003. The shuttle radar topographic mission - a new class of digital elevation models acquired by spaceborne radar. *ISPRS J. Photogramm. Remote Sens.* **57**, 241-262.

Rasmussen, S., Andersen, K., Svensson, A., Steffensen, J., Vinther, M. et al. 2006. A new Greenland ice core chronology for the Last Glacial termination. *J. Geophy. Res.* **111**, D06102. doi:10.1029/2005JD0067079

Raymo, M. E. and Ruddiman, W. F. 1992. Tectonic forcing of late Cenozoic climate. *Nature* **359**, 117 - 122.

Richter, D.D., Oh, N.H., Fimmen, R.L. and Jackson, J.A. 2007. The rhizosphere and soil formation. In. Zoe, C. and Whitbeck, J. eds. *The Rhizosphere – An Ecological Perspective.* Springer-Verlag, in press.

Riebe, C.S., Kirchner, J.W., Granger, D. E. and Finkel, R. 2001a. Minimal climatic control on erosion rates in the Sierra Nevada, California. *Geology* **29**, 447-450.

Riebe, C. S., Kirchner, J.W., Granger, D. E. and Finkel, R. 2001b. Strong tectonic and weak climatic control of long-term chemical weathering rates. *Geology* **29**, 511-514.

Riebe, C.S., Kirchner, J.W. and Granger, D.E., 2001c. Quantifying quartz enrichment and its consequences for cosmogenic measurements of erosion rates from alluvial sediment and regolith. *Geomorphology* **40**, 15-19.

Riebe, C. S., Kirchner, J. W. and Finkel, R. 2003. Long-term rates of chemical weathering and physical erosion from cosmogenic nuclides and geochemical mass balance. *Geochimica et Cosmochimica Acta* **67**, 4411-4427.

Riebe, C. S., Kirchner, J. W. and Finkel, R. 2004a. Sharp decrease in long-term chemical weathering rates along an altitudinal transect. *Earth and Planetary Science Letters* **218**, 421-434.

Riebe, C. S., Kirchner, J W. and Finkel, R. 2004b. Erosional and climatic effects on long-term chemical weathering rates in granitic landscapes spanning diverse climate regimes. *Earth and Planetary Science Letters* **224**, 547-562.

Roering, J., Kirchner, J. W. and Dietrich, W. 1999. Evidence for nonlinear, diffusive sediment transport on hillslopes and implications for landscape morphology. *Water Resources Research* **35**, 853-870.

Rother, H. and Shulmeister, J. 2006. Synoptic climate change as a driver of late quaternary glaciations in the mid-latitudes of the southern hemisphere. *Climate of the Past* **2**, 11-19.

Rosenbloom, N. and Anderson, R. 1994. Evolution of the marine terraced landscape, Santa Cruz, California. *Journal of Geophysical Research* **99**, 14013-14030.

Schaefer J.E.A. 2005. The CRONUS-Earth (Cosmic-Ray prOduced NUclide Systematics on Earth) initiative. *Geochimica et Cosmochimica Acta* **69**, A167.

Schaller, M., von Blanckenburg, F., Veldkamp, A., Tebbens, L., Hovius, N. and Kubik, P. 2002. A 30,000 yr record of erosion rates from cosmogenic ^{10}Be in middle European river terraces. *Earth and Planetary Science Letters* **204**, 307-320.

Schaller, M., von Blanckenburg, F., Hovius, N., Veldkamp, A., van den Berg, M. and Kubik, P. 2004. Paleoerosion rates from cosmogenic ^{10}Be in a 1.3 Ma terrace sequence: response of the river Meuse to changes in climate and rock uplift. *Journal of Geology* **112**, 127-144.

Schildgen, T., Phillips, W. and Purves, R. 2005. Simulation of snow shielding corrections for cosmogenic nuclide surface exposure studies. *Geomorphology* **64**, 67-85.

Schlatter, A., Schneider, D., Geiger, A. and Kahle, H. 2005. Recent vertical movements from precise levelling in the vicinity of the city of Basel, Switzerland. *International Journal of Earth Sciences (Geologische Rundschau)* **94**, 507-514.

Schmid, S.M., Fügenshuh, B., Kissling, E. and Schuster, R. 2004, Tectonic map and overall architecture of the Alpine orogen. *Eclogae Geologicae Helvetiae* **97**, 93-117.

Schmid, S.M., Pfiffner, O.A., Froitzheim, N., Schönborn, G. and Kissling, E. 1996. Geophysical-geological transect and tectonic evolution of the Swiss-Italian Alps. *Tectonics* **15**, 1036-1064.

Schmidt, K. and Montgomery, D. 1995. Limits to relief. *Science* **270**, 617-620.

Schlunegger, F., Matter, A., Burbank, D.W., Leu, W., Mange, M.A. and Matyas, J. 1997 Sedimentary sequences, seismofacies and evolution of depositional systems of the Oligo-Miocene Lower Freshwater Molasse Group, Switzerland. *Basin Res.* **9**, 1-26.

Schlunegger, F., Detzner, K. and Olsson, D. 2002. The evolution towards steady state erosion in a soil-mantled drainage basin: semi-quantitative data from a transient landscape in the Swiss Alps. *Geomorphology* **43**, 55-76.

Schlunegger, F., Schneider, H., 2005. Relief-rejuvenation and topographic length scales in a fluvial drainage basin, Napf area, central Switzerland. *Geomorphology* **69**, 102-117.

Schmid, S., Pfiffner, O.A., Froitzheim, N., Schönborn, G. and Kissling, E. 1996. Geophysical-geological transect and tectonic evolution of the Swiss-Italian Alps. *Tectonics* **15**, 1036-1064.

Shakun, J., Burns, S.J., Fleitmann, D., Kramers, J., Matter, A., et al. 2007. A high-resolution, absolute-dated deglacial speleothem record of Indian Ocean climate from Socotra Island, Yemen. *Earth Planet. Sci. Lett.* **259**, 442-456.

Sharp, M., Tranter, M., Brown, G. and Skidmore, M., 1995. Rates of chemical denudation and CO_2 drawdown in a glacier-covered alpine catchment. *Geology* **23**, 61-64.

Shepard, M., Campbell, B., Bulmer, M.H., Farr, T.G., Gaddis, L. and Plaut, J. 2001. The roughness of natural terrain: a planetary and remote sensing perspective. *Journal of Geophysical Research* **106**, 32777-32795.

Singer, C., Shulmeister, J. and McLea, B. 1998. Evidence against a significant Younger Dryas cooling event in New Zealand. *Science* **281**, 812-814.

Small, E., Anderson, R., Hancock, G., 1999. Estimates of the rate of regolith production using ^{10}Be and ^{26}Al from an alpine hillslope. *Geomorphology* **27**, 131-150.

Stone, J.O.H. 1998. A rapid fusion method for the extraction of 10Be from soils and silicates. *Geochimica et Cosmochimica Acta* (Scientific comment) **62**, 555-561.

Stone, J.O.H. 2000. Air pressure and cosmogenic isotope production. *Journal of Geophysical Research B: Solid Earth* **105**, 23753-23759.

Synal, H., Bonani, G., Doebeli, M., Ender, R., Gartenmann, P., Kubik, P., Schnabel, C. and Suter, M. 1997. Status report of the PSI/ETH AMS facility: *Nuclear Instruments and Methods in Physics Research, Section B: Beam Interactions with Materials and Atoms* **B123**, 62-68.

Tarboton, D., Bras, R. and Rodriguez-Iturbe, I. 1991. On the extraction of channel networks from digital elevation data. *Hydrological Processes* **5**, 81-100.

Taylor, A. and Blum, J. 1995. Relation between soil age and silicate weaterhing rates determined from the chemical evolution of a glacial chronosequence. *Geology* **23**, 979-982.

Templeton, D. 1953. Nuclear reactions induced by high energy particles: *Annual review of nuclear science* **2**, 93-104.

Ustaszewski, M. and Pfiffner, O.A. 2008. Neotectonic faulting, uplift and seismicity in the Central and Western Swiss Alps. in Siegesmund, S., Fügenschuh, B., Froitzheim, N. (eds.). Geological Society, London **298,** 231-249. DOI: 10.1144/SP298.12

Vanacker, V., von Blanckenburg, F., Grovers, G., Molina, A., Poesen, J. and Deckers, J. 2007. Restoring dense vegetation can slow moutain erosion to near natural benchmark levels. *Geology* **35**, 303-306. DOI: 10.1130/G23109A.1

Vanacker, V., von Blanckenburg, F., Hewawasam, T. and Kubik, P.K. 2007. Constraining landscape development of the Sri Lankan escarpment with cosmogenic nuclides in river sediment. *Earth and Planetary Science Letters* **253**, 402-414.

Vebel, M. 1993. Temperature dependence of silicate weathering in nature: how strong a feedback on long-term accumulation of atmospheric CO_2 and global greenhouse warming. *Geology* **21**, 1059-1062.

Vincent, C. 2002. Influence of climate change over the 20th Century on four French glacier mass balances. *J. Geophys. Res.* **107**, ACL 4-1 - 4-12.

von Blanckenburg, F., Belshaw, N. and O'Nions, R. 1996. Separation of [9]Be and cosmogenic [10]Be from environmental materials and SIMS isotope dilution analysis. *Chemical Geology* **129**, 93-99.

von Blanckenburg, F., Hewawasam, T. and Kubik, P.K. 2004. Cosmogenic nuclide evidence for low weathering and denudation in the wet, tropical highlands of Sri Lanka. *Journal of Geophysical Research* **109**, 10.1029/2003JF000049

von Blanckenburg, F. 2005. The control mechanisms of erosion and weathering at basin scale from cosmogenic nuclides in river sediment. *Earth and Planetary Science Letters* **237**, 462-479.

Walker, J.C.G., Hays, P.B. and Kasting, J.F.1981. A negative feedback mechanism for the long-term stabilization of Earth's surface temperature. *Geophysical Research Letters* **86,** 9776–9782.

Webb, D. and Howard, R. 1994. The solar cycle variation of coronal mass ejections and the solar wind flux. *Journal of Geophysical Research* **99**, 4201-4220.

Welten, M. 1982. Vegetationsgeschichtliche Untersuchungen in den Westlichen Schweizer Alpen; Bern-Wallis. *Denkschriften der Schweizerischen Naturforschenden Gesellschaft* **95**, 1-105.

West, A., Galy, A. and Bickle, M. 2005. Tectonic and climatic controls on silicate weathering. *Earth and Planetary Science Letters* **235**, 211-228.

Whipple, K., Tucker, G., 1999. Dynamics of the stream-power river incision model: implications for height limits of mountain ranges, landscape response timescales, and research needs. *Journal of Geophysical Research B: Solid Earth* **104**, 17661-17674.

White, A. 2003. Natural weathering rates of silicate minerals. In *Surface and Ground Water, Weathering, and Soils* (ed. J.I. Drever) *Treatise on Geochemistry* **5** (eds. H.D. Holland and K.K. Turekian), Elsevier-Pergamon, Oxford, 134-164.

White, A., Blum, A., Schulz, M., Vivit, D., Larsen, M. and Murphy, S. 1998. Chemiccal weathering in a tropical watershed, Luquillo Mountains, Puerto Rico: I. long-term versus short-term chemical fluxes. *Geochimica Cosmochimicha Acta* **62**, 209-226.

White, A., Bullen, T., Schulz, M., Blum, A., Huntington, G. and Peters, N. 2001. Differential rates of feldspar weathering in granitic regoliths. *Geochimica et Cosmochimica Acta* **65**, 847-869.

White, A. and Blum, A. 1995. Effects of climate on chemical weathering in watersheds. *Geochimica et Cosmochimica Acta* **59**,1729-1747.

Willenbring (Staiger), J., Gosse, J., Toracinta, R., Oglesby, B., Fastook, J. and Johnson,J.V. 2007. Atmospheric scaling of cosmogenic nuclide production: Climate effect, *J. Geophys. Res.* **112**, B02205, doi:10.1029/2005JB003811

Wittmann, H. von Blanckenburg, F., Kruesmann, T., Norton, K.P. and Kubik. P.K. 2007. The relation between rock uplift and denudation from cosmogenic nuclides in river sediment in the Central Alps of Switzerland. *Journal of Geophysical Research A: Earth Surface* **112**, F04010.

Wobus, C.W., Heimsathe, A., Whipple, K.X. and Hodges, K.V. 2005, Active out-of-sequence thrust faulting in the central Nepalese Himalaya. *Nature* **434**, 1008-1011.

Wolock, D. and McCabe, G.J. 2000. Differences in topographic characteristics computed from 100- and 1000-m resolution digital elevation model data. *Hydrological Processes* **14**, 987-1002.

Yoo, K., Amundson, R., Heimsath, A.M., Dietrich, W.E. and Brimhall, G.H. 2007. Integration of geochemical mass balance with sediment transport to calculate rates of soil chemical weathering and transport on hillslopes. *Journal of Geophysical Research* **112**, F02013.

Zhang, P., Molnar, P. and Downs, W. 2001. Increased sedimentation rates and grain sizes 2-4 Myr ago due to the influence of climate change on erosion rates. *Nature* **410**, 891-897.

Zhang, W. and Montgomery, D. 1994. Digital Elevation Model grid size, landscape representation, and hydrologic simulations. *Water Resources Research* **30(4)**, 1019-1028.

Zhang, X., Drake, N., Wainwright, J. and Mulligan, M. 1999. Comparison of slope estimates from low resolution DEMs: scaling issues and a fractal method for their solution. *Earth Surface Processes and Landforms* **24**, 763-779.

A1. Cosmogenic nuclides: theory and methods

Cosmic rays and the particles that they produce have been a subject of intensive and fruitful research for the last century. It was particularly the work of Lal and Peters (1967) which laid the groundwork for the use of terrestrial cosmogenic nuclides in the Earth Sciences. These are isotopes produced by cosmic rays in Earth's atmosphere and crust. In this work, Lal and Peters (1967) described the production of secondary cosmic rays which are responsible for creating cosmogenic nuclides. In the 1980's, attention focused on the so-called 'in situ-produced' cosmogenic nuclides. These early works (Kurz, 1986; Nishiizumi et al., 1986; Chen-Feng You et al., 1988) showed the promise of the method. These early works were followed by a flourish of research on the scaling laws of primary and secondary particles (Lal, 1991; Dunai, 2000; Stone, 2000; Masarik et al., 2001; Lifton et al., 2001). The production rates of in situ-produced cosmogenic nuclides in minerals was investigated by (Nishiizumi et al., 1989, Kubik et al., 1998). In-depth discussions of the principles can be found in an excellent review by Gosse and Phillips (2001). The importance of sample geometry (Dunne et al., 1999) and exposure history (Nishiizumi et al.,1989, Lifton et al., 2001) have also been explored. The range of applications for in situ-produced cosmogenic nuclides is still rapidly expanding. Exposure ages have been used to unravel the chronology of Alpine glaciation (Ivy-Ochs et al., 1996, 2004). Dating of cave deposits (Granger et al., 1997) and terraces (Schaller et al., 2004) have shed light on the control mechanisms of fluvial incision. Basin-averaged denudation rates (Brown et al., 1995; Granger et al., 1996) have widened the field. Hewawasam et al. (2003) and Vanacker et al., (2007) quantified the impact of anthropogenic modification on natural erosion rates. Recent applications have moved to the orogen scale, where new thrust faults have been identified (Wobus et al., 2005) and the correlation between rock uplift rates and denudation rates proven (Wittmann et al., 2007). What follows is a summary of the most important aspects of how galactic cosmic radiation produces an atom of ^{10}Be in a grain of quartz at the Earth's surface, the nuclide used in this study.

A1.1. PRODUCTION RATES

Galactic cosmic radiation is mostly composed of high energy protons, $0.1\text{-}10^{20}$ GeV, thought to be produced in our galaxy during supernova explosions. These primary particles interact with nuclei in the upper atmosphere to create a cascade of secondary particles of lower energy (Figure A1). These reactions produce nucleonic particles, protons and neutrons, and unstable mesonic particles, pions and muons (Allkofer, 1975). These particles may retain enough energy to interact with another nucleus and propagate the particle cascade. While many of these secondary particles reach the ground, the majority react in the atmosphere to create meteoric cosmogenic nuclides. It is those particles that arrive at the surface with sufficient energy that are responsible for producing in situ cosmogenic nuclides. There are numerous nuclides that can be produced in this manner. Only a handful of these are in common use in the Earth Sciences; ^{3}He, ^{10}Be, ^{14}C, ^{21}Ne, ^{26}Al and ^{36}Cl. This study focuses on ^{10}Be, so the following discussion will be based on this nuclide, however the theory remains similar for the others.
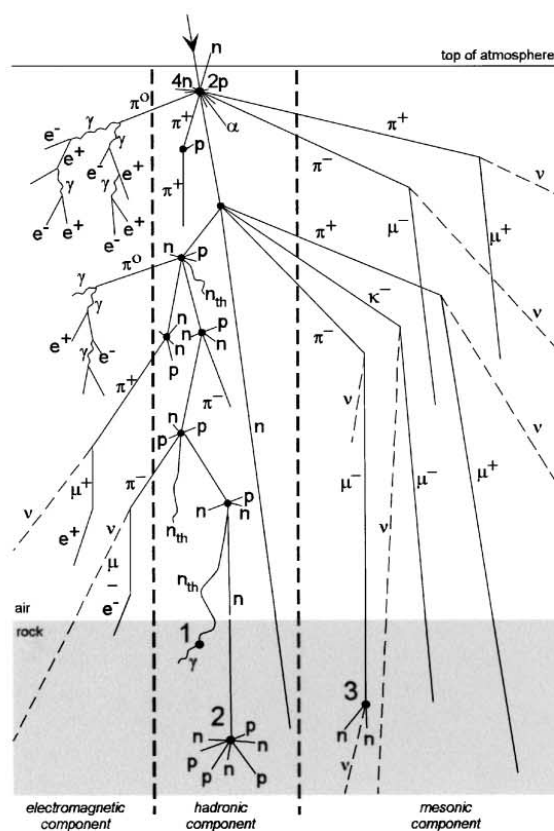
Figure A1. Secondary cosmic ray cascade generated from primary cosmic radiation in the upper atmosphere (Gosse and Phillips, 2001).

Energetic secondary nucleons, mostly neutrons, produce ^{10}Be through spallation reactions mostly with ^{16}O (Templeton, 1953). Quartz, with a regular chemical composition and abundant occurrence in the continental crust, is an ideal mineral for ^{10}Be studies. In a spallation reaction, the initial energy gained from neutron impact is dissipated by spalling off smaller nuclear particles in the form of protons, alpha particles, and neutrons. In many cases, secondary particles are ejected, albeit with lower energy. There is a higher probability that very heavy, near the original atomic mass, or very light particles will be produced. This leads to lower production rates for ^{10}Be from oxygen and silicon, ^{16}O(n,4p3n)^{10}Be, ^{28}Si(n,x)^{10}Be, than for other nuclides such as ^{26}Al in silicon, ^{28}Si(n,2pn)^{26}Al (roughly 1 to 6 in this case). ^{10}Be remains one of the most widely used nuclides because unlike aluminum, beryllium is a rare element. Therefore, the stable isotope ^{9}Be can be added as a spike and the nuclide ratios measured with an accelerator mass spectrometer (Synal et al., 1997). ^{10}Be can also be formed in quartz through negative muon capture. In these reactions, a negative muon, produced by the decay of unstable secondary mesonic particles, is captured by a target nucleus. Despite the fact that about half of the cosmic ray flux consists of muons at Earth's surface, these reactions are much rarer than neutron spallation because they are not subject to strong nuclear interactions as are neutrons. Muon reactions take the form of either nuclear capture of a slow negative muon (hereafter referred to as stopped muons), or even spallation with fast muons, ^{16}O(μ^-,αpn)^{10}Be, ^{28}Si(μ^-,x)^{10}Be. The vast majority (98%) of ^{10}Be in the top few meters of the surface are formed through spallation reactions (Gosse and Phillips, 2001). Due to their weak interaction with target nuclei, muons penetrate much deeper than neutrons. The vastly shorter attenuation path length for neutrons versus stopped and fast muons, ~160 g cm^{-2} vs. ~1500 g cm^{-2} and ~3800 g cm^{-2}, respectively, means that the importance of spallation reactions decreases rapidly with depth so that by ~3m, muon reactions become the dominant production reactions (also see Figure A4). The decrease of production rates with depth in a material is described by its attenuation mean free path length and is dependant on the size and energy of the secondary cosmic rays and the thermodynamic properties of the target material. The adsorption mean free path length for neutron spallation reaction is ~160 g cm^{-2}, corresponding to a depth of ~60 cm in continental rocks. The muogenic component can be separated into stopped and fast components with adsorption depth scales of ~0.5 and 14 m for stopped and fast muons respectively (Granger and Smith, 2000; Schaller et al., 2002). Path lengths and production reactions will be discussed in the next section. A major complication arises with respect to attenuation lengths in the form of the distribution of the incoming

particles. A given particle traveling at an acute angle to the surface will traverse a greater atmospheric depth than one traveling vertically. The longer path leads to variations in particle flux and energy distribution with the angle of incidence, being highest for vertical and lowest for horizontal trajectories (Nishiizumi, et al., 1986). This also causes the attenuation lengths for non-vertical trajectories to be shorter than that for vertical trajectories.

This incoming secondary ray flux is also significantly modulated before it reaches the surface. Interactions with Earth's magnetic field, solar winds, and the atmosphere leads to large variations in the cosmic ray flux with space and time. Earth's magnetic field acts primarily as a high pass filter allowing higher energy particles to pass while rejecting lower energies. Cut-off rigidities, the lower bound of allowable energy, are highest at the equator and reduce towards the poles (Lal and Peters, 1967). This means that only high energy particles penetrate at Equatorial latitudes, while a larger distribution of particles enter the atmosphere near the poles. The resultant increasing flux from equator to poles causes higher production rates at higher latitudes, about which more will be described in the next section. In addition to causing a spatial variation in flux, the magnetic field has also caused temporal variations (Lal and Peters, 1967; Nishiizumi et al., 1989). Cosmic ray flux varies inversely with field intensity. This means that production rates of cosmogenic nuclides, including ^{10}Be will change with time (Figure A2). This has been shown in marine sediments using meteoric ^{10}Be and tree rings using ^{14}C, (Bard et al., 1990) and is supported by magnetic field variations through time. Nishiizumi et al. (1989) and Frank et al. (1997) have shown that production
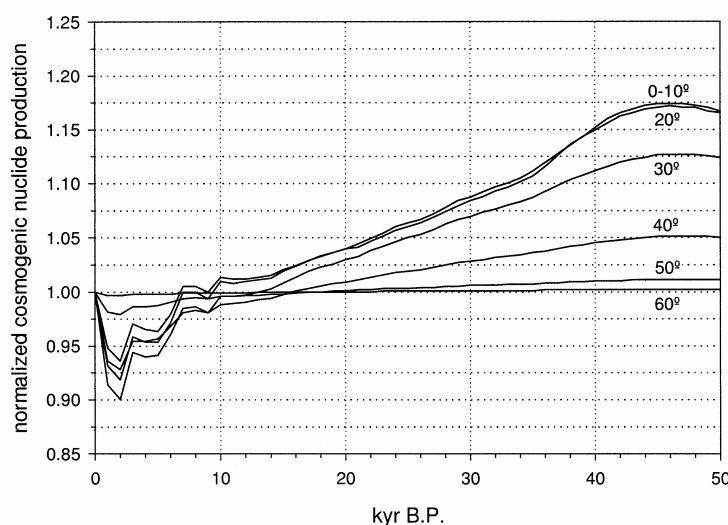
Figure A2. Time integrated production rates for the last 50 ka by latitude normalized to the present day production rate. Note that the variations become less pronounced at higher latitudes (Dunai, 2001).

rates over the last ~100 ka have been as much as 30% higher than the modern value (Masarik et al., 2001).

Another temporal variation is solar modulation, with periods of high activity generating higher solar wind activity (Beer, 1991), which in turn are close proxies for coronal mass ejection (Webb and Howard, 1994). In contrast with the case of Earth's magnetic field, the solar-wind phenomenon is cyclic, causing short-term variations around a long-term mean. The overall effect on the primary cosmic ray flux and the resultant production of cosmogenic nuclides is therefore most likely negligible, unless a longer-term cycle exists (Gosse and Phillips, 2001). As mentioned above, Earth's magnetic field is the cause of latitudinal variations in the flux of secondary cosmic radiation. These variations will now be described in more depth.

Due to the lower cut-off rigidity near the poles, more radiation with a wider distribution of energies is incident on Earth's atmosphere in these regions. The increase from Equator to poles is however not constant. Cosmic ray flux is low and relatively stable up to ~30° latitude then increases up to ~60° after which there is little variation (Lal, 1991). The high fluxes in the polar regions do not translate into high production rates of cosmogenic nuclides (Figure A3) because the majority of the increased flux is in the form of lower energy particles which are not capable of the nuclear reactions which create cosmogenic nuclides.
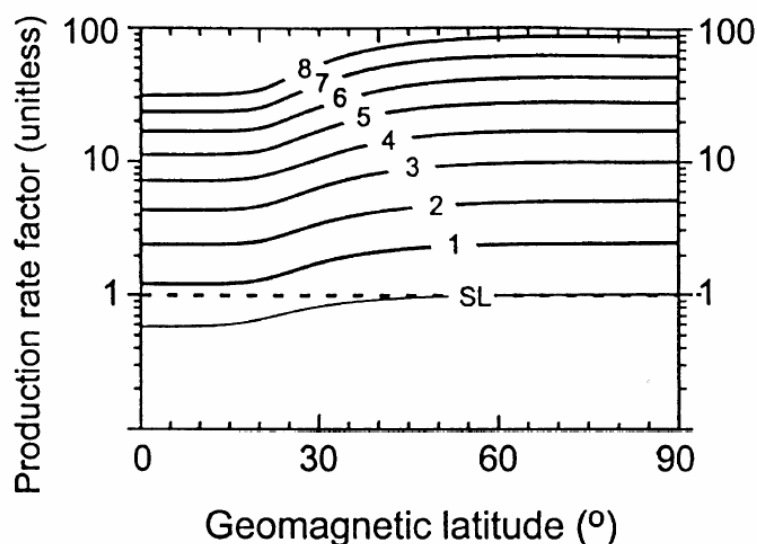
Figure A3. Changes in production rates of cosmogenic nuclides with altitude (atmospheric depth) and latitude (Lal, 1991, as modified by Gosse and Phillips, 2001). Curves represent the relative production rate at a given elevation (labels are in km).

Finally, the largest effects occurs due to the dependence of cosmic ray flux with air pressure, and hence altitude. As stated above, the secondary cosmic rays are attenuated with depth (Lal and Peters, 1967). This holds true for both the solid Earth and the atmosphere. With a mean free path length of ~160 g cm^{-2}, the e-folding length of the particle flux in the atmosphere is ~0.8km. This means that the particle flux reduces by 1/e with every 0.8km of elevation change, and that at higher elevations there will be a higher flux and subsequently higher production rates (Figure A3). An interesting problem arises here with respect to past climate change. Willenbring et al. (2007) showed that during glacial periods, compression of the air column results in changes in nuclide production rates at the same altitude with time.

In addition to the latitudinal variations, there are longitudinal changes in the flux. These are related to quasi-stationary, ~3ky, air pressure anomalies (Stone, 2000). These are capable of changing production rates by up to 8%. These modulations are seldom included in cosmogenic studies, based on the difficulty and uncertainty involved in their estimates. As the anomalies have large spatial scales, it is less important to correct for them in erosion rate studies. Even if the absolute erosion rates are over or under estimated, the relationships between basins in the same geographic region (i.e. the Alps) will remain unchanged.

All of these factors that modulate the flux of cosmic rays reaching the surface must be accounted for when determining the production rate of cosmogenic nuclides in mineral grains. The calculation and scaling of production rates will be discussed in the following section.

Due to the complexities of the spatial and temporal variations in cosmogenic nuclide production rates, related to the modulations in cosmic ray flux discussed above, it is convenient to define a global base value from which these changes may be modeled. This value is known as the sea-level high latitude production rate, and represents the production rate of a given cosmogenic nuclide, ^{10}Be in our case, scaled to the value that it would have at sea-level at latitudes higher than 60°. Numerous estimates for the SLHL production rate for ^{10}Be exist, ranging from 4.74 to 6.4 atoms g_{qtz}^{-1} yr^{-1} (Gosse and Phillips, 2001), but rescaling according to Stone (2000) brings most to a range between 5.1 and 5.5 atoms g_{qtz}^{-1} yr^{-1}. There are two methods for determining the production rates of cosmogenic nuclides in a given mineral. They can either be calculated from theoretical predictions based on particle physics, or the concentration of a nuclide in a surface of known age can be measured and used to calculate the production rate required to produce that concentration. Both methods yield considerable spread in rates. To complicate matters further, values based on measurements

require the use of some type of scaling laws in order to determine the SLHL values for that surface. The various researchers have not all used the same scaling factors (Kubik et al., 1998; Dunai, 2000; Granger and Smith, 2000). This means that these production rates are not interchangeable, and that a given production rate must be used with the appropriate scaling laws.

In order to accurately calculate exposure times or erosion rates (as discussed in the next section), it is necessary to accurately model the production of in situ cosmogenic nuclides through time with depth in rock or sediment. As stated above, ^{10}Be in quartz is produced through nucleonic spallation reactions and muon capture processes. So any accurate production rate model must include terms for both types of reactions. The change in neutron spallation with depth can be well modeled using the sum of two exponential equations;

$$P_{nuc}(z) = P_{nuc}(0) \times \sum_{i=1}^{2} a_i \times e^{\frac{-z \times \rho}{b_i}} \qquad \text{A1}$$

where $P_{nuc}(z)$ is the production rate from spallation reactions at a depth of z, $P_{nuc}(0)$ is the nucleonic spallation component of the SLHL production rate at depth 0, ρ is the density of the overlying material, and a_i and b_i are scaling coefficients (Kubik et al., 1998; Dunai, 2000; Schaller et al., 2002). In the upper few meters of the surface, nucleonic spallation reactions dominate the ^{10}Be production (Figure A4), with muogenic reactions accounting for 3.6% of the nuclide concentration, assuming a non-eroding surface and the production coefficients of Schaller et al. (2002), Table A1). Many studies of slowly or non-eroding landscapes ignore the muogenic contribution (Bierman and Steig, 1996; Bierman and Nichols, 2004). In rapidly eroding landscapes on the other hand, deep material is rapidly brought to the surface. The rapid exhumation means that little of the deep muogenic produced ^{10}Be has decayed by the time it reaches the surface, whereas in the slow erosion case, enough time has elapsed that the deep muogenic ^{10}Be is mostly decayed. Assuming infinitely fast erosion the contribution (integrated over the time the rock takes to reach the surface) by muogenic reactions to the surface nuclide concentration will be 37.2% (i.e. the ratio of neutron spallation to muon production at the surface). Even at the low erosion rates found in Middle Europe, (20 mm ky^{-1}), muogenic produced ^{10}Be makes up 30.6% of the surface nuclide inventory. Clearly muons
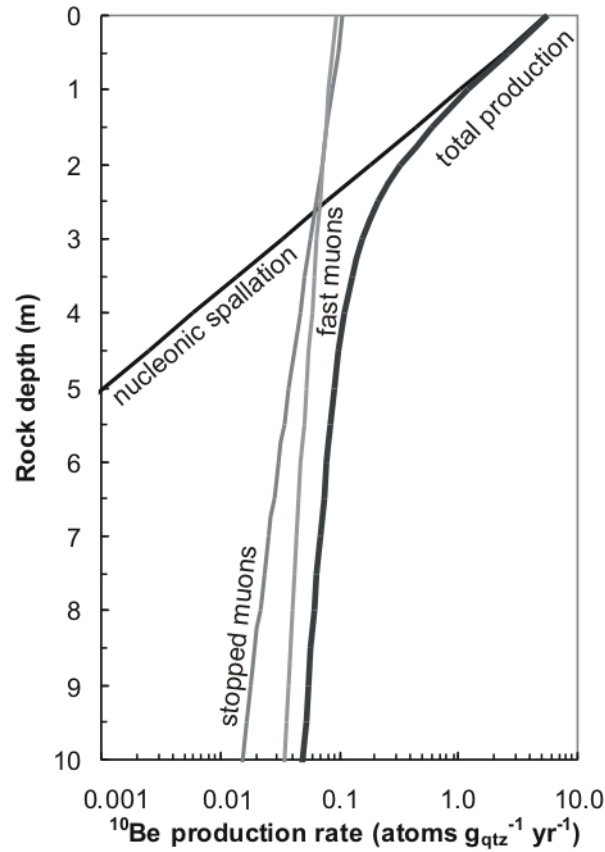
Figure A4. Individual production rates for nucleons and stopped and fast muons calculated using equations A1-A4.

can not be discounted, and the production rates for muons must also be calculated (Granger and Smith, 2000; Schaller et al., 2002). Negative muon capture is the main production mode for stopped muons, (Heisinger et al., 2002a, 2002b). As for spallation, there is no simple exponential for fitting these reactions. The best fits for depth profiles as determined by Schaller et al. (2002) based on the calculations of Heisinger (2002a, 2002b) are of the form;

$$P_{\mu stopped}(z) = P_{\mu stopped}(0) \times \sum_{j=1}^{3} a_j \times e^{\frac{-z \times \rho}{b_j}} \qquad \text{A2}$$

Finally, fast muon processes are modeled by the equation;

$$P_{\mu fast}(z) = P_{\mu fast}(0) \times \sum_{k=1}^{3} a_k \times e^{\frac{-z \times \rho}{b_k}} \qquad \text{A3}$$

The final form of the production rate equation for ^{10}Be is then equation A4;

$$N(z) = \left[\left(P_{nuc}(0) \times \sum_{i=1}^{2} a_i \times e^{\frac{-z \times \rho}{b_i}}\right) + \left(P_{\mu stopped}(0) \times \sum_{j=1}^{3} a_j \times e^{\frac{-z \times \rho}{b_j}}\right) + \left(P_{\mu fast}(0) \times \sum_{k=1}^{3} a_k \times e^{\frac{-z \times \rho}{b_k}}\right)\right] \times \frac{\left(1 - e^{-\lambda \times t}\right)}{\lambda} \quad \text{A4}$$

These equations allow the production rates for surface exposure (z=0) and depth profiles (z>0) to be calculated.

Table A1.   Production coefficients determined by Schaller et al. (2002) for depth dependant neutron spallation, fast muon, and stopped muon production of ^{10}Be in quartz.

			Constants	a (g cm^{-2})	b (g cm^{-2})
			i=1	1.0747	157
			i=2	-0.0747	5.887
$P_{nuc}(0)$	= 5.33	atoms g_{qtz}^{-1} yr^{-1}	j=1	-0.05	160
$P_{\mu stopped}(0)$	= 0.106	atoms g_{qtz}^{-1} yr^{-1}	j=2	0.845	1030
$P_{\mu fast}(0)$	= 0.093	atoms g_{qtz}^{-1} yr^{-1}	j=3	0.205	3000
			k=1	0.01	100
			k=2	0.615	1520
			k=3	0.375	7600

A1.2. CALCULATION OF DENUDATION RATES

The basic form of the equation given by Lal (1991) governing the accumulation and loss of cosmogenic nuclides in a mineral grain through time is

$$\frac{dN(z,t)}{dt} = -N(z,t)\lambda + P(z,t) \qquad \text{A5}$$

where P is the production rate at depth z, N is the nuclide concentration, and λ is the half-life. So the change in nuclide concentration with time (i.e. the concentration determined from AMS isotope ratio measurements) is dependant on two main variables, the production rate and the rate of decay. Equation A4 above calculates the nuclide concentration at any single depth through time (or all depths at a single time). The simplest case for cosmogenic

accumulation is for no erosion and no radioactive decay. In this case, nuclide concentration will be a function of the production rate of that nuclide and the length of time that the surface has been exposed. Considering the same non-eroding surface, i.e. $z = 0$, with 0 initial beryllium concentration, then the buildup of radioactive cosmogenic nuclides with time, $N(t)$, will be proportional to the exposure time and production rate at zero depth, $P(0)$, less loss through radioactive decay (Lal, 1991), where ^{10}Be decays with a half-life of 1.5Ma;

$$N(t) = \frac{P(0)}{\lambda}\left(1 - e^{-\lambda t}\right)$$
  A6

In cases in which previous nuclide concentrations exist, an inheritance term must be added, so that;

$$N(t) = N_0(t)e^{-\lambda t} + \frac{P(0)}{\lambda}\left(1 - e^{-\lambda t}\right)$$
  A7

giving the full equation of the nuclide concentration of a non-eroding surface, where $N(t)$ is the nuclide concentration at the surface, $N_0(t)$ is the inherited nuclide concentration, $P(0)$ is the surface production rate, λ is the half-life of the measured nuclide, and t is the time of exposure (i.e. age).

If erosion is introduced, any particle at a depth, z, will move towards the surface with a rate proportional to the denudation rate, so that the production rate at time t, $P(t)$, increases as a function of time. By assuming steady state erosion and constant production rate over the time period of interest, Lal (1991) obtained the following solution to equation A5, describing the concentration of a nuclide at depth.

$$N(z,t) = N(z,0)e^{-\lambda t} + \frac{P(0)}{\lambda + \frac{\rho\varepsilon}{\Lambda}}e^{\frac{-z\times\rho}{\Lambda}} \times \left(1 - e^{-\left(\lambda + \frac{\rho\varepsilon}{\Lambda}\right)t}\right)$$
  A8

The first term, $N(z,0)e^{-\lambda t}$ is the term for inheritance. If the inherited nuclide concentration is 0, the inheritance term can be removed. Furthermore, because material is eroded from Earth's surface, we are interested in the special case of $z = 0$ so that;

$$N(t) = \frac{P(0)}{\lambda + \frac{\rho\varepsilon}{\Lambda}} \times \left(1 - e^{-\left(\lambda + \frac{\rho\varepsilon}{\Lambda}\right)t} \right) \qquad \text{A9}$$

Cosmogenic steady state can be said to exist when the surface nuclide concentration reaches secular equilibrium in which case inputs in the form of in situ production is balanced by loss, i.e. erosion and decay. Attainment of steady state requires that the time over which constant erosion has occurred is sufficiently long, such that $t \gg \frac{\rho\varepsilon}{\Lambda}$. Solving equation A9 for this case yields;

$$N(t) = \frac{P(0)}{\lambda + \frac{\rho\varepsilon}{\Lambda}} \qquad \text{A10}$$

where P(0) represents each production term as described in the depth production rate equations A1-A3, yielding;

$$N(t) = \left[P_{nuc}(0) \times \sum_{i=1}^{2} \left(\frac{a_i}{\lambda + \frac{\rho\varepsilon}{b_i}} \right) + P_{\mu stopped}(0) \times \sum_{i=1}^{3} \left(\frac{a_j}{\lambda + \frac{\rho\varepsilon}{b_j}} \right) + P_{\mu fast}(0) \times \sum_{i=1}^{3} \left(\frac{a_k}{\lambda + \frac{\rho\varepsilon}{b_k}} \right) \right] \times \frac{\left(1 - e^{-\lambda t} \right)}{\lambda} \quad \text{A11}$$

Equation 11, gives the concentration of a nuclide, N(t), at the surface of rock or sediment eroding at rate, ε. The 'apparent exposure age', t, is the time required to erode a thickness of the rock or sediment equal to the adsorption depth, ~ 70 cm. The apparent exposure age is inversely related to the erosion rate (equations A10 and A11) such that faster erosion rates are averaged over shorter time scales (Figure A5).
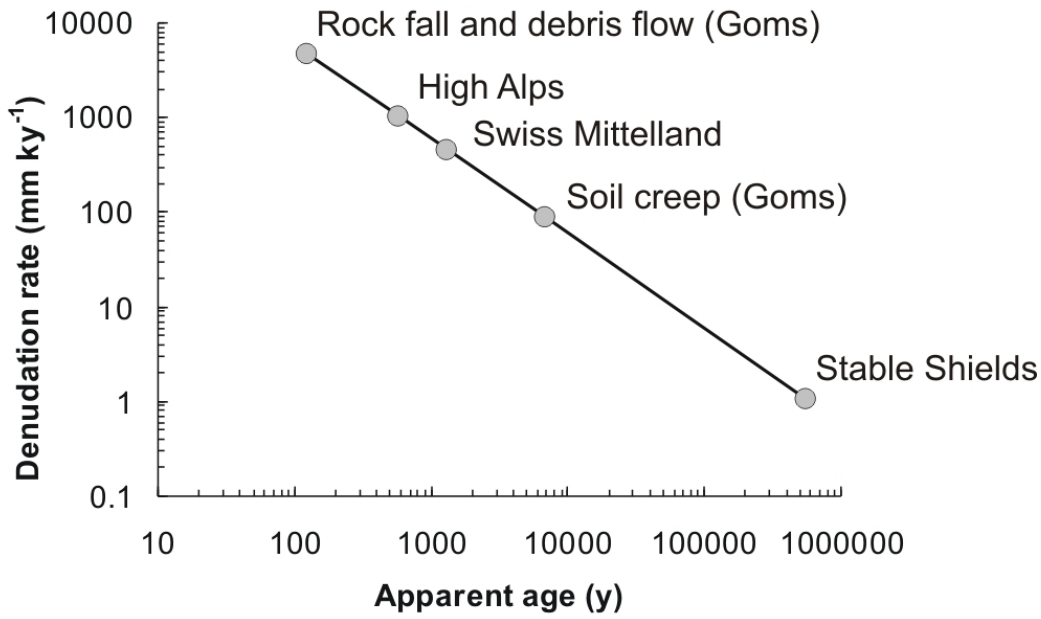
Figure A5. In situ ^{10}Be-derived denudation rates plotted against apparent age. Landscapes and processes discussed in the text are plotted for reference.

A1.3 BASIN-AVERAGED DENUDATION RATES

In the above discussion, it has been shown that the denudation rate for a given point can be calculated from the surface concentration of an in situ-produced cosmogenic nuclide. While the erosion rate of single bedrock outcrops, for instance, are useful, estimations of denudation rates over larger spatial areas are advantageous for climate and orogenic studies. Granger et al. (1996) verified that this is possible using a basin-averaged approach.

Stream sediment is composed of regolith that has been eroded from throughout a drainage basin, delivered to the steam by hillslope processes, and mixed by fluvial action. Areas of the drainage basin which are eroding rapidly will deliver more material than those that are eroding slowly, such that the stream sediment is a rate-weighted sample of denudation within the catchment. With respect to in situ-produced cosmogenic nuclides, this has been expressed as;

$$\bar{N} = \frac{\sum N_i E_i A_i}{\sum E_i A_i} = \frac{\sum P_0 \Lambda A_i}{\sum E_i A_i} = \frac{P_0 \Lambda}{\bar{E}} \qquad \text{A12}$$

by Granger et al. (1996), where $\bar{N} \, and \, \bar{E}$ are the mixed sediment nuclide concentration and mean erosion rate respectively, N_i the concentration of each component with local erosion rate E_i and contributing area A_i. If perturbations occur which cause some parts of the catchment to deliver sediment out of proportion to its long-term erosion rate, then the resulting denudation rate will be skewed (in favor of the disturbance if extra material is delivered, i.e. accelerated soil erosion by land stripping, and against it if less material is delivered, i.e. dams). The same holds true for manually mixed soil samples. This is possible because the nuclide concentration in a well mixed regolith column is equal to the surface concentration in the case of no vertical mixing (equivalent to bedrock erosion, i.e. equation A7) Granger et al. (1996).

There are, however, important caveats to the basin-averaging method (von Blanckenburg, 2005). These assumptions are:

-Erosion rate is constant through time such that cosmogenic steady state can be achieved.

-All subcatchments contribute sediment to the stream in proportion to their denudation rates.

-No grain size differences occur due to either bedrock distribution or preferential release by denudational processes.

-Quartz is not enriched in soils though time.

-Storage time, i.e. time spent on the hillslopes after initial erosion, is less than transport time.

-The erosional timescale (apparent age) is less than the decay timescale for the nuclide in question. This corresponds to ~0.5 mm ky^{-1} for ^{10}Be, where $\lambda \approx 6.6 \times 10^{-7}$ yr^{-1} and the absorption depth scale is 700 mm.

-Finally, as mentioned by Bierman and Steig (1996), quartz should be equally abundant in the contributing lithologies.

Many of these assumptions can be accounted for if enough information is available, i.e. correcting for quartz abundances (Bierman and Steig, 1996) or quartz enrichment (Riebe et al., 2001c).

A1.4. DETERMINING BURIAL AGES WITH ^{10}BE

A major goal of climate and paleo-climate studies is the dating of terrace deposits for the purpose of understanding the interaction between climate and surface processes. In addition to modern basin-averaged denudation rates, ^{10}Be can also be used to calculate the time since deposition and paleo-denudation rates of terrace material (Hancock et al., 1999; Granger and Smith, 2000; Perg et al., 2001; Schaller et al., 2004). In the case of a steadily eroding landscape, sediment and with it cosmogenic nuclides, will be delivered to a stream in proportion to the local erosion rate. The stream sediment, which nuclide activity records the denudation rate of the basin from which it originated, may be deposited in the form of channel fill, point bars, over-bank deposits, etc. The sediment is continually exposed to cosmic rays and builds up cosmogenic nuclides in accordance with the previously described depth production equations (equation A11, Schaller et al., 2002). At some later stage, the stream may incise back into these sediments leaving behind fluvial terraces. By collecting samples at various depths in the terrace sediments, a nuclide concentration model can be fitted from which the age of the deposit can be determined. Furthermore, at sufficient depths, there is minimal nuclide build-up; therefore any nuclides in these deep sediments are inherited, i.e. deposited with the sediment, and represent the prevalent denudation signal of the basin at the time the sediment was deposited, i.e. a paleo-denudation rate. For further information, refer to the discussion of the Trub terraces in section 3 (Chapter 2).

A1.5. TOPOGRAPHIC SHIELDING OF COSMIC RAYS

The above equations are valid only for horizontal, non-obstructed surfaces. In most natural settings, the surface slope is not 0. Furthermore, in mountainous settings in which many cosmogenic nuclide studies are carried out, there are substantial obstructions on the
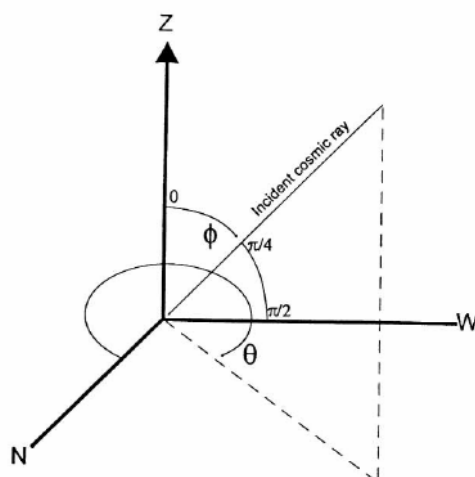
Figure A6. Coordinate system for calculating topographic skyline shielding where φ is the angle of incidence, and θ is the subtended angle (after Gosse and Phillips, 2001).

skyline (i.e. there is not a clear 180°, 360° view). The obstructions block a portion of the cosmic ray flux which must be accounted for when calculating nuclide production rates (Lal, 1991; Dunne et al., 1999). In the case of an even energy dispersion, the blocked and unblocked rays would have the same properties, the topographic shielding correction would simply be the ratio of exposed to obstructed skyline. However, as mentioned above, cosmic rays with vertical trajectories have higher energy and longer penetration lengths than those with acute angles of incidence. This means that the energy distribution must be integrated over 90° inclination and 360° (Figure A6, A7) azimuth in order to calculate the full, unobstructed rate. The shielded portion is then integrated and corrected for. The common method of calculating skyline shielding using digital elevation models, DEMs, introduces further complications (Norton and Vanacker, 2008). A complete discussion of topographic shielding and the methods of calculating shielding factors for single samples and entire drainage basins is given in Section 2.
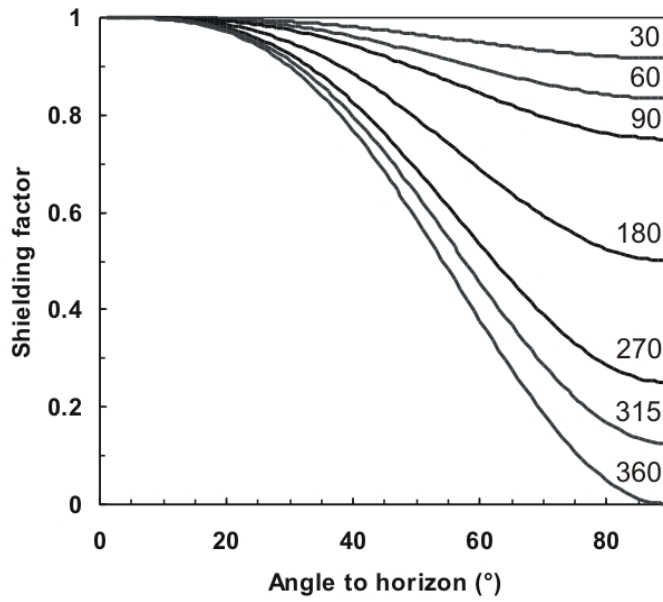
Figure A7. Impact of topographic shielding on production rates of cosmogenic nuclides (recalculated after Dunne et al, 1999). Shielding increases (values closer to 0) as the angle of incidence (φ) and subtended angle (θ) increase.

A1.6. COSMIC RAY SHIELDING BY SNOW

Cosmic rays are attenuated with depth in any medium in proportion to its density,

$$P(x) = P(0)e^{-\left(\frac{\rho x}{\Lambda}\right)} \qquad \text{A13}$$

(Lal, 1991), where P(x) is the production rate at depth x, P(0) is the production rate at the surface, ρ is density, x is depth, and Λ is the absorption mean free path. For regions that experience snow cover for any portion of the year, there will be shielding of the incoming radiation in proportion to the density of the snow and the duration of snow cover:

$$S_{snow} = \frac{1}{12}\sum_{n}^{12} e^{-\left(\frac{z_{snow} \times \rho_{snow}}{\Lambda}\right)} \qquad \text{A14}$$
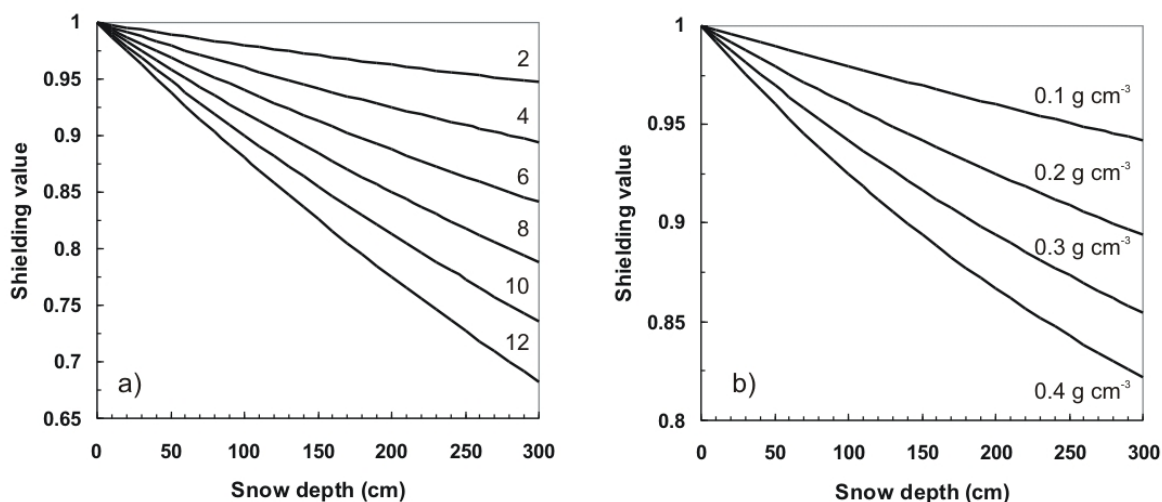
Figure A8. a) Effect of snow cover of 0.2 g cm^{-3} snow for 2, 4, 6, 8, 10, and 12 months duration and b) 4 months duration of snow of 0.1, 0.2, 0.3 and 0.4 g cm^{-3}. b) Effect of 4 months duration of snow of 0.1, 0.2, 0.3 and 0.4 g cm^{-3} density.

where S_{snow} is the shielding factor (equal to $P(x)/P(0)$) derived for snow cover, z_{snow} is the monthly snow depth, ρ_{snow} is the snow density and Λ is the nucleonic spallation adsorption mean free path, 157 g cm^{-3}. Equation A14 ignores the muogenic contribution. This simplification can be justified based on the extremely long penetration lengths of muons. Even 3 meters of continual snow cover (i.e. 12 months) would lead to less than 10% shielding for stopped muons, and even less for fast muons. When the low muogenic production rates are taken into consideration, the total effect on ^{10}Be production would be less than 0.2% at shallow depths. Average snow density for Eurasia is 0.16 to 0.48 g cm^{-3}, with an average of 0.16 to 0.33 g cm^{-3} (Onuchin and Burenina, 1996).

Snow shielding factors for Switzerland were calculated in ArcGIS using monthly average snow depths as reported by Auer (2003), using an average snow density of 0.2 g cm^{-3}. Maximum reported snow cover in the Alps varies in depth from less than 40 cm in parts of the Mittelland to more than 250 cm in the Central Alps. Duration exhibits a similar pattern, with 0-4 months of 0 snow cover at lower elevations and up to 12 months in glaciated regions. In the case of the Goms such an approach is unacceptable, as the range of elevations, ~1200-3500 meters, is quite large over a small spatial area, ~160 km^2. An alternative approach was designed for determining snow shielding factors in the Goms. The average annual snow depth in Switzerland, as calculated from Auer (2003), was determined for each elevation (Figure A8a). A strong correlation exists between snow depth and elevation. A snow shielding factor for the elevation range of the Goms was then determined using a 2nd order polynomial equation (Figure A8b).
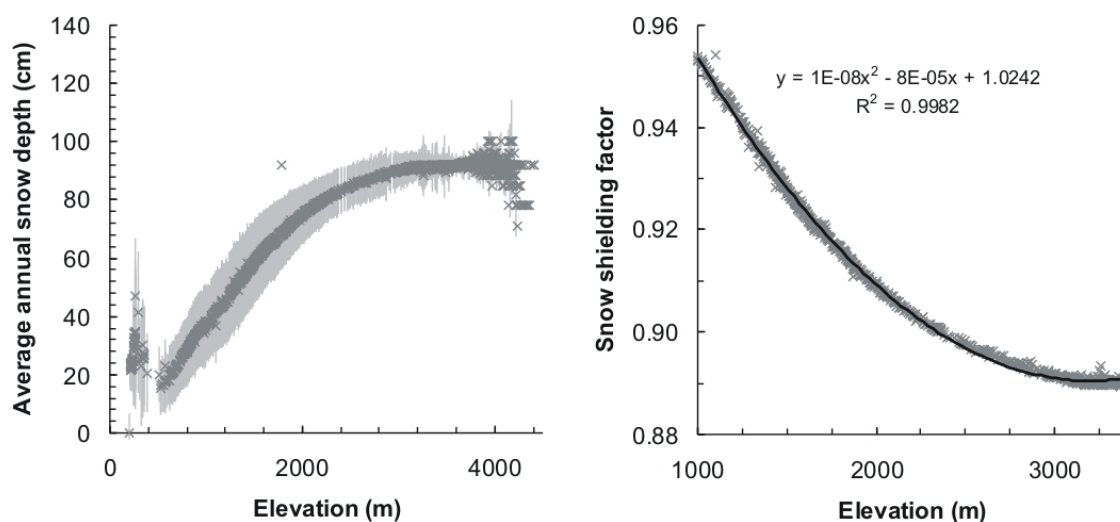
Figure A9. a) Average annual snow depth in Switzerland (Auer, 2003) plotted against elevation. The dark grey crosses are the mean snow depth for each elevation and the light grey bars are 1-sigma variability. b) Snow shielding factors for the elevation range of the Goms. A 2nd order polynomial fit (black line), R2 = 0.9982, was used to calculate individual snow shielding factors.

Based on the average snow density for the region, snow shielding factors are not likely to exceed 0.7, and are typically around 0.9 (Figures A8 and A9b). This corresponds to production rates that are 10-30% lower than in the non-shielded cases. By comparing this to typical topographic shielding values (no more than 10 to 15%), it can be seen that snow shielding, even in steep terrains, often has as great or greater impact on nuclide production rates than topographic shielding. It is also worth noting that the Swiss records, while impressive, can not provide a sense of snow cover throughout the entire late Pleistocene and Holocene. Modeling by Schildgen et al. (2005) suggest that modern snow thickness and duration might be as much as 20% lower than the immediate post-LGM. However, the snowline has fluctuated substantially throughout the Holocene. [14]C ages on wood melting out of Swiss glaciers show that these glaciers have been smaller than their modern extent throughout much of the Holocene (Hormes, et al., 1997; Joerin, et al., 2006). So, while our ability to estimate paleo-snow cover is in most cases woefully inadequate, using modern snow data provides a good initial estimate of the shielding values.

A1.7. FIELD AND LABORATORY METHODS

Three main types of samples were collected and processed for this work. 1) ^{10}Be concentrations in quartz in stream sediments yielded basin-averaged denudation rates. 2) Quartz from amalgamated soils provided ^{10}Be-derived total denudation rates for individual landforms. 3) Individual soil samples were also used in concert with bedrock samples to calculate chemical weathering rates in the Upper Rhone Valley.

Basin-averaged denudation rates are determined from ^{10}Be concentrations in quartz in stream sediments. The sediment was taken from channel bars, pools, or the active stream channel. Preference was given to samples that were in active river transport. While it is possible that sand resides on streams banks and floodplains for considerable amounts of time, it is unlikely that the sediment composing the active channel forms remains immobile for long periods. By sampling the material from the active portion of the channel, the length of time spent in transport is reduced as compared to the hillslopes.

Samples consisted of 3-5 kgs of sand through small pebbles sized sediments. In cases where stream velocities were high (a.k.a. Goms), finer sand was taken from pools. Where coarser deposits were found, samples were sieved in the field to <2cm. There is likely little bias introduced by this method. Pools concentrate finer grained particles in mountainous streams compared to coarser channel bars. However, all samples were later sieved and an equivalent grain size fraction was taken in each case. So, despite varying grain size distribution in the sampling locations, denudation rates were measured on equivalent sizes which likely have similar denudational histories. After collection, samples were dried for 24 hours at 100°C. Upon cooling, the sand was sieved to <0.125mm, 0.125-0.25 mm, 0.25-0.5mm, 0.5-1mm, 1-2mm, and >2mm size fractions. For studies in the Swiss Foreland, the 0.5-1mm fraction was used for analysis, while in the upper Rhone valley; the 0.25-0.5mm grain size fraction was preferentially measured. This was due to numerous inclusions of micas in the larger quartz grains. In all cases, grain size dependencies were tested by analyzing smaller and larger fractions in several samples. The selected grain size was then passed through an isodynamic magnetic separator to remove magnetic grains, primarily biotite micas and iron oxides in this case. The Swiss Mittelland samples were at this point immediately placed in 10% HCl, which will be discussed later. All other samples underwent an additional quartz concentration step. This was necessary because of the low quartz contents in the river sand, <10-30%, for the Goms samples. Approximately 100g of each

sample was placed in a 1L PE bottle to which ~100ml 12M (24%) HF was added. The bottle was then shaken for 30 seconds and the samples were washed 5x with deionized water. After drying, ~0.5 g of powdered, 50 microns, magnetite was mixed with the sample and then passed once more through the isodynamic magnetic separator (at 25 ohm, 10° angle) 2x. This method was initially developed for the separation of quartz from feldspars (Iacumin and Quercioli, 1993). The strong solution of HF attacks the feldspar surfaces creating numerous pits. Quartz remains relatively untouched during this process due to the short contact time. When magnetite powder is added to the sample, it becomes insinuated into the nooks and crannies of the feldspar grains but will not coat the quartz grains as they remain smooth. Upon passing the sample through the magnetic separator, the feldspars now act as magnetic grains and are easily separated from the quartz. The end yield is often >90% quartz. One potential hazard of this method is also a potential benefit. If quartz grains have considerably irregular surfaces (i.e. sedimentary aggregates, or metamorphosed grains for instance) then they will also become coated with magnetite powder and be included in the magnetic fraction. While this presents a potential sampling bias, the impact for these areas should be small because there was only one predominant quartz species. From the opposite perspective, however, this presents a possible method for separating quartz species in the same watershed (i.e. smooth igneous grains, granular sedimentary masses, or irregular metamorphic grains). It might be possible then to use an HF etching-magnetite powder technique in order to determine the denudation rates of different rock types in the same catchment independently. The magnetite method is not capable, however, of removing significant amounts of white mica micas from the samples. White mica is not easily etched by HF and the added magnetite finds little purchase on the grains. For samples in which white mica was a significant component, an additional heavy liquid separation was performed. 20g aliquots of the sample were added to a separation funnel which was filled with Bromoform, density = 2.87 g cm^{-3}, diluted with acetone to a density of ~2.70 g cm^{-3}. The white mica, with an average density of 2.83 g cm^{-3} sinks to the bottom and are drained through the stop-cock, while quartz, density = 2.65 g cm^{-3}, remains suspended. After heavy liquid separation, the samples were repeatedly washed in H$_2$O and then left to dry before being introduced into the HCl. Heavy liquid separation was not used to remove the feldspars in these samples because of the density range of feldspars. Feldspars can have densities ranging from 2.55 to 2.76 g cm^{-3} depending on their composition. Since the density of quartz lies in the middle of this range, it is not possible to separate the two species.

Once a reasonably clean quartz and feldspar sand was obtained, 70 g of sand was added to a 1L PE bottle to which ~30ml of 10% HCl was added. The HCl breaks down carbonates and metal oxide species. The samples were shaken at room temperature for 24 hours. The process was repeated until the HCl no longer reacted with the sample. This was determined as the point when the solution after 1 day remained colorless. Carbonates reacted extremely rapidly, while oxides typically required 1 to 2 days to be completely removed. Following the initial cleaning, and between each of the HCl steps, the samples were washed 5x with deionized water.

After treatment with HCl, ~300 ml of 5% HF was added and the samples were shaken at 60° C for 24 hours at which time the samples were rinsed 5x with deionized water and the process was repeated once for a total of 2 days in HF. Following this, samples were shaken at 60° C for 5 days intervals with 5% HF until pure quartz remained. The weak HF dissolves the feldspars, but rapidly becomes saturated with silicon, protecting the quartz from attack. If given enough time and fresh HF, quartz will eventually also dissolve, so it is important at this point to regularly check the sample mass to ensure that significant quantities of quartz are not lost. Typical quartz cleaning times are from 1 to 4 weeks total. This step has a secondary function. In situ-produced ^{10}Be has a sea-level high latitude production rate of about 5.3 atoms g_{qtz}^{-1} y^{-1}. ^{10}Be may also be produced in the atmosphere and be delivered to the surface by dry deposition (dust) and precipitation at which point it can adsorb onto the surface of quartz grains. The flux of meteoric ^{10}Be varies through time, but is normally 4 orders of magnitude higher than that of in-situ production. By bathing the quartz in weak HF for extended intervals, the outermost layers of the quartz are dissolved, and the meteoric ^{10}Be component is leached away (Brown et al., 1991; Kohl and Nishiizumi, 1992). Once obtained, the purity of the quartz was checked optically, using a petrographic microscope and using ICP-OES. Due to the small sample sizes (<200mg) of the ICP-OES samples, the results were not always representative of the entire sample. Preference was therefore given to the optical method. Beryllium extraction methodology was based on that of von Blanckenburg et al. (1996, 2004). The complete procedure may be found in A1.8.

Some modifications were made to the original von Blanckenburg et al. (1996, 2004) method. The first major difference from the von Blanckenburg et al. (1996, 2004) method is a fluoride conversion step. Upon dissolution with hydrofluoric acid, the cations are in

Relative element yield
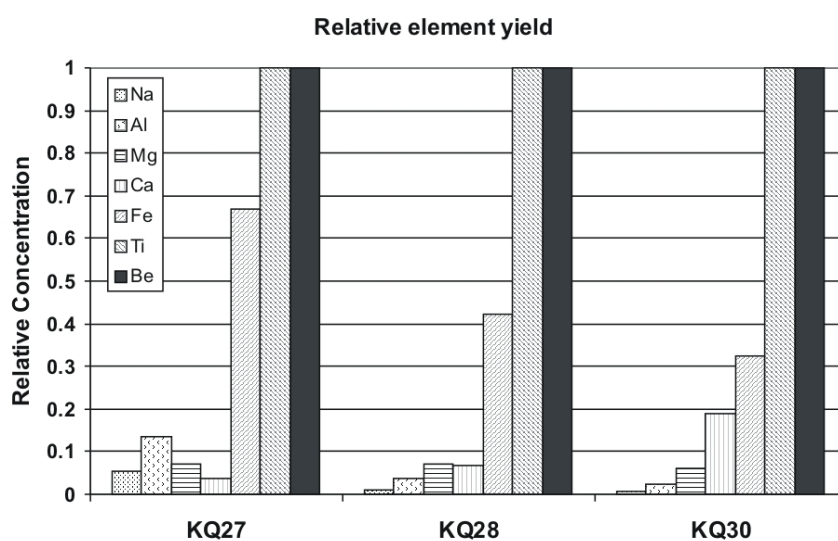
Figure A10. Results of water leaching of fluoride extraction. Note 100% recovery of Be phases.

fluoride phases. Of these, BeF_3 is completely soluble in water, while many other fluorides; AlF_3, MgF_2, NaF, etc., are only partially soluble. By adding 10 ml of Millipore water to the dissolved samples and leaving it at 60°C for 30 minutes, the beryllium fluorides are quantitatively leached out of the cake leaving behind many impurities (Stone, 1998; Figure A10). This step forgoes the need for digestion and conversion using Aqua Regia. An important point to note is that aluminum fluorides are not completely soluble in water, and that if aluminum is to be measured, this technique can not be used.

Second, cation exchange chromatography of beryllium was re-calibrated for nitric acid instead of hydrochloric acid. The main advantage of using HNO_3 is that the chromatographic separation may be immediately followed by hydroxide precipitation with ammonia and addition of silver nitrate, thus skipping the need for an additional evaporation step which was necessary to HCl before addition of the $AgNO_3$, which would result in precipitation of AgCl, which is not desirable. Elution of Be in nitric acid is quite similar to the case of HCl, with clear separation of Na from Be with 0.5 and 1M HNO_3 respectively (Figure A11), while some Mg does elute with the Be tail. This however is readily removed with precipitation.

1 ml cation column elution with nitric acid
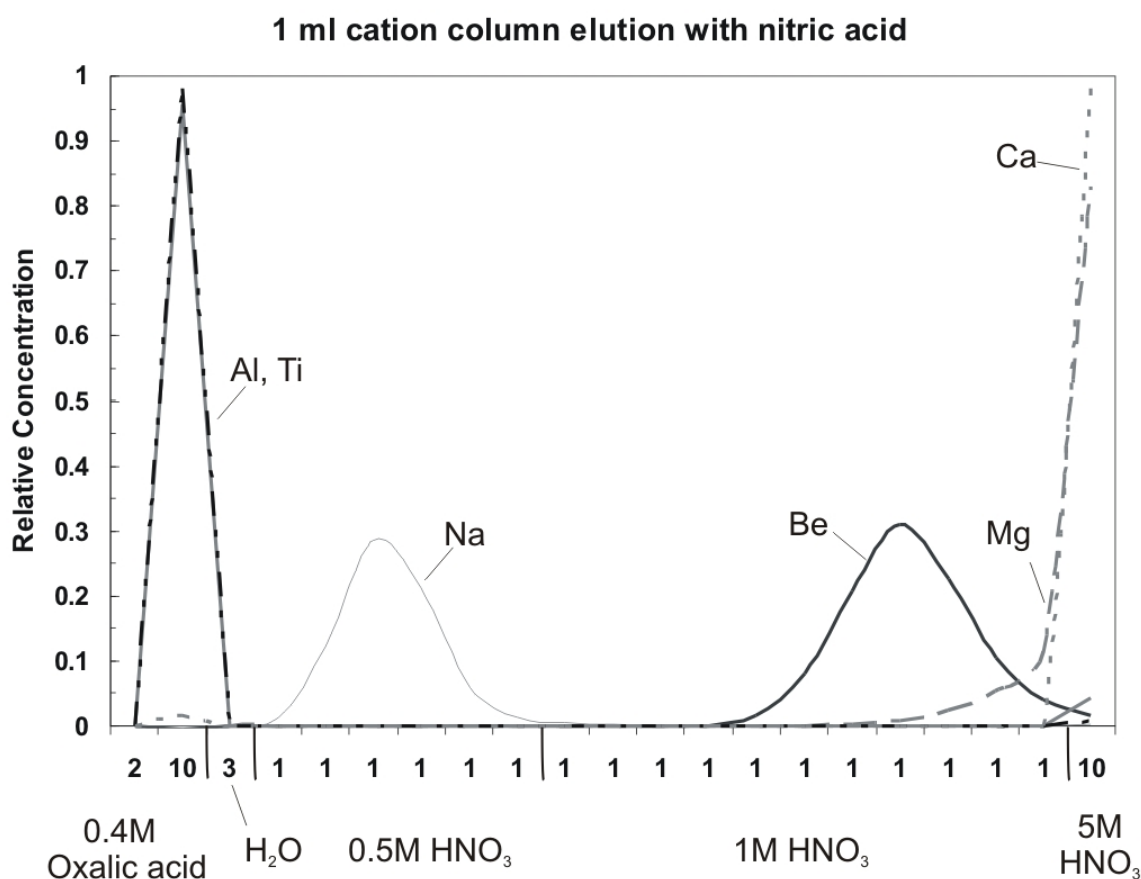
Figure A11. Elution calibration for nitric acid with 1 ml cation exchange resin.

All [10]Be-derived denudation rates in this work were calculated from [10]Be/[9]Be ratios measured by Peter Kubik at the Intitut für Teilchenphysik, ETH Zürich (Synal et al., 1997). The measured isotopic ratios were first corrected for contribution of [10]Be from the blank (Table A2). Between 0.150 and 0.300 mg of [9]Be was added to each sample using a 405.4 ppm solution of [9]Be carrier diluted from phenakites by Friedhelm von Blanckenburg and Jérôme Chmeleff. Process blanks were included in each chemistry run using the same amount of carrier solution. The mean number of [10]Be atoms in the blank and their standard deviations were used to correct sample [10]Be concentrations and propagated into count statistical AMS errors. Erosion rates were then calculated from the [10]Be concentrations using an Excel macro based on equation A11 including shielding due to topography and snow cover. Where glaciers were present, glacial cover was removed from the basin area to approximate the effect of thick ice on nucleonic spallation production. Sample denudation

rates, including the production parameters used, can be found in Tables 3 and 4 (Chapters 2 and 3, respectively).

Table A2. Process blanks used for 10Be concentration corrections. Note that stared, *, samples in Tables 3 and 4 were corrected using only the stared blanks.

Sample Label	Comment	BE9 [nA]	Be10/Be9	ERROR (%)	"Bor" Count	CARRIER Weight mg	9Be added g
ZB5879	Blank KQ115*	683	1.44E-14	29.2	6	0.17435	1.74E-04
ZB5889	Blank KQ127*	589	1.05E-14	34.3	6	0.17435	1.74E-04
ZB5908	BlankGQ-6*	758	1.82E-14	38.2	4	0.176	1.76E-04
ZB5912	BlankGQ-8*	634	9.5E-15	32.6	3	0.217	2.17E-04
ZB6129	KQ151	581	1.29E-14	23.1	10	0.171113	1.71E-04
ZB6075	BlankGQ-9	613	1.76E-14	23.1	10	0.219686	2.20E-04
ZB5356	GQ1	497	2.7E-14	22.6	19	0.175053	1.84E-04
ZB5333	GQ2	412	1.9E-14	35.4	14	0.163796	1.72E-04
ZB5464	GQ-3	1032	1.44E-14	31	4	0.175538	1.85E-04
ZB5473	KQ92 Blank	994	1.65E-14	25.3	2	0.17484	1.84E-04
ZB5490	GQ-4	1317	2.16E-14	22.2	3	0.176025	1.85E-04
ZB5491	KQ104-Blank	564	3.1E-14	32.7	5	0.163539	1.72E-04

A1.8. STEP-BY-STEP LABORATORY PROCEDURE

1. Final Quartz Leach
−   Take the weight of the 90ml or 240ml Savillex screw top beaker and lid
    (max 50g Quartz in 90ml beaker, max ca. 150g in 240ml beaker)
−   Add 7M HF p.a. quality so that sample is just covered with HF plus 5 mm excess liquid height and heat 1h
    maximum 120°C with lid
        (48% ΔHF (28M): Millipore H_2O=1:3)
−   Cool down
−   Wash with Millipore H_2O

−   Add ΔAq reg so that sample is just covered with acid plus 5 mm excess liquid height
        (ΔHNO$_3$conc (15M) : ΔHClconc (6M) =1:3)
−   Cool without lid until gas is gone (ca. 30min)
−   Minimum 1h heating (120°C) with lid
−   Wash, rinse, shake thoroughly (4-5x) with Millipore H_2O
−   Dry on hotplate in Savillex Beaker
−   Take precise weight

2. Sample dissolution
Stochiometric reaction: SiO_2 + 4HF → SiF_4 + $2H_2O$
Need 116 ml 28M ΔHF for 50g Quartz
a) Multiple addition method
−   Add 28M ΔHF p.a. quality so that sample is fully covered with acid plus 5mm excess liquid height.
    first and second additions: strong exothermic reaction; do not heat; add HF in increments.
−   Heat (120°C) without lid, evaporate to dryness
−   Third addition: add HF 2x Quartz volume, put open beaker on hot plate and evaporate
−   Repeat if all the quartz is not dissolved
−   Dry down. Don't loose any loose sample flakes!

b) Alternative: Single Step dissolution method
−   Take 240 ml Savillex beaker
−   Weigh Qtz as in 1
−   Add 2x stochiometric amount of HF. CAREFUL! Monitor temperature!
−   Close beaker and heat until all Qtz is dissolved
−   Evaporate

3a. Sample conversion, Carrier, Al-Aliquot
−   Add 0.15mg (~0.4 ml for 405 ppm carrier) Be carrier, take precise weight
−   Add 20ml Aq Reg (6ml HNO$_3$conc + 12ml 6M HCl), heat until all residue is dissolved and evaporate gently
−   Add 10ml 6M ΔHCl
−   Transfer into cleaned 10ml centrifuge tubes centrifuge 5 Min, 3000 rpm,
−   Check purity by ICP-OES

Al-chemistry : (Be only: Go to "Column Fe")

− Label 50ml Nalgene tubes, Place empty tube on balance, zero balance
− Label cleaned 100ml Bottle, place on large topload balance, zero balance
− Transfer sample solution into Nalgene tube, leaving the undissolved residue behind
− Take TSS (Total Sample Solution) weight
− Take 100μl aliquot, transfer into 100ml bottle
− Weigh 25ml Nalgene tube, take weight of aliquot
− Add 100ml 0.35M ΔHNO$_3$ to Al aliquot
    (Millipore H$_2$O: Δ 14M HNO$_3$ = 975 : 25ml)
− Take weight of Al solution

3b. Optional BeF$_2$ - Leaching (No Al)

− Carrier must have been added before sample decomposition
− Add 10 ml H$_2$O to fluoride cake
− Heat gently for one hour
− Pipette off 10ml supernate (containing water-soluble BeF$_2$, TiF$_4$, Fe(II)F$_2$ but no AlF$_3$)
− Evaporate solution
− Add 10ml 6M ΔHCl
− Transfer into cleaned 10ml centrifuge tubes, centrifuge 5 Min, 3000 rpm,
− Check purity by ICP-OES

4. Column Fe

2ml Biorad 1x8 100-200 mesh in 7.5ml RKBN104704 Column stored in H$_2$O

− Open column and let water drop out
− 5ml + 5ml 0.3M ΔHCl: clean resin
− 2ml + 2ml + 2ml: 6M ΔHCl: condition resin
− Load sample (4 or 10ml 6M HCl)   Collect Be (+Al) (in cleaned Savillex beaker
− Exactly 2ml + 2ml + 2ml: 6M ΔHCl   Collect Be (+Al)   or Oak Ridge Tube)
− 5ml + 5ml 0.3M ΔHCl: clean resin
− seal and store column in Millipore H$_2$O
− Evaporate sample
− Add 4ml (20ml for dirty quartz) 0.4M Oxalic Acid on sample, warm to 60° with lid for ca. 2h
− Cool down, wait for 30 minutes, transfer to 10 ml centrifuge tube
− Centrifuge 5 Min, 3000 rpm, load supernate only to column

5a. 1ml Column Be (Clean Samples : Al < 5mg)

1ml Biorad AG50-X8 (200-400 mesh) in 7.5ml RKBN104704 Column stored in H$_2$O

− Open column and let water drop out
− 2ml + 3ml ~5M ΔHNO$_3$: clean resin
− 2ml + 3ml Millipore H$_2$O: Remove HNO$_3$ from resin
− 2ml + 3ml: 0.4M Oxalic Acid: condition resin
− Load sample   Collect Al in 90 ml Savillex beaker
− 1ml 0.4M Oxalic Acid: wash sample down   Collect Al in 90 ml Savillex beaker

– 1ml 0.4M Oxalic Acid: wash sample down	Collect Al in 90 ml Savillex beaker
– 10ml 0.4M Oxalic Acid: elute Fe, Al, Ti etc.	Collect Al in 90 ml Savillex beaker

(clean Savillex beakers prior to this with 3M HCl and Millipore H_2O)

– 1ml + 2ml Millipore H_2O: remove Oxalic Acid from column

– 2ml + 2ml + 4ml 0.5M Δ HNO_3: elute Na

– 3ml + 3ml +5ml 1M Δ HNO_3	Collect Be in new cleaned 15ml centrifuge tube

– 10ml 5M Δ HNO_3 clean resin

– 5ml H_2O to remove 5M HNO_3

– Seal and store column in H_2O

5b. 2ml Column Be (Clean Samples : Al < 5mg)

1ml Biorad AG50-X8 (200-400 mesh) in 7.5ml RKBN104704 Column stored in H_2O

– Open column and let water drop out

– 5ml + 5ml ~5M ΔHNO_3: clean resin

– 5ml + 5ml Millipore H_2O: remove HNO_3 from resin

– 5ml + 5ml: 0.4M Oxalic Acid: condition resin

– Load sample	Collect Al in 90 ml Savillex beaker
– 2ml 0.4M Oxalic Acid: wash sample down	Collect Al in 90 ml Savillex beaker
– 2ml 0.4M Oxalic Acid: wash sample down	Collect Al in 90 ml Savillex beaker
– 20ml 0.4M Oxalic Acid: elute Fe, Al, Ti etc.	Collect Al in 90 ml Savillex beaker

(clean Savillex beakers prior to this with 3M HCl and Millipore H_2O)

– 2ml + 4ml Millipore H_2O: remove Oxalic Acid from column

– 6ml + 10ml 0.5M Δ HNO_3: elute Na

– 5ml + 5ml +10ml 1M Δ HNO_3	Collect Be in new cleaned 50ml centrifuge tube

– 20ml 5M Δ HNO_3 clean resin

– 10ml H_2O to remove 5M HNO_3

– Seal and store column in H_2O

5c. 5ml Column Be (Dirty Samples : Al > 5mg)

5ml Biorad AG50-X8 (200-400 mesh) in 15 ml Eichrom Column stored in H_2O

– Open column and let water drop out

– 10ml + 15ml ~5M Δ HNO_3: clean resin

– 10ml + 15ml Millipore H_2O: remove HCl from resin

– 10ml + 15ml: 0.4M Oxalic Acid: condition resin

– Load sample in 20ml 0.4M Oxalic Acid	Collect Al in 90 ml Savillex beaker
– 5ml 0.4M Oxalic Acid: wash sample down	Collect Al in 90 ml Savillex beaker
– 5ml 0.4M Oxalic Acid: wash sample down	Collect Al in 90 ml Savillex beaker
– 50ml 0.4M Oxalic Acid: elute Fe, Al, Ti etc.	Collect Al in 90 ml Savillex beaker

(clean Savillex beakers prior to this with 3M HCl and Millipore H_2O)

– 5ml + 10ml Millipore H_2O: Remove Oxalic Acid from column

– 15ml + 25ml 0.5M Δ HNO_3: elute Na

– 20ml 1M ΔHNO_3 wash

– 20 + 20 ml 1M Δ HNO_3	Collect Be in new clean 50ml centrifuge tube

– 50ml 5M Δ HNO_3 clean resin

– 25ml H_2O to remove 5M HNO_3

– Seal and store column in H_2O

(Column Al)
– 1ml Biorad AG1-X8 (100-200 mesh) in 7.5ml RKBN104704 Column stored in H_2O
– Open column and let H_2O drop out
– 2 ml Millipore H_2O
– 5+5ml 0.3M ΔHCl clean resin
– 2+2ml H_2O remove HCl
– 2+2+2 ml Oxalic Acid
– Al Eluate from Be-Column load sample
– 4+2ml 0.05M Oxalic Acid/0.5M HCl wash *   Save effluent in case Al elutes early
– 5+5ml 0.05M Oxalic Acid/0.5M HCl   Collect Al in 17ml Savillex beaker
– 5ml + 5ml 0.3ml HCl   elute Ti
– seal and store column in H_2O

5. Be-Oxide + Silver
Be Precipitation

Dilute suprapure NH_4OH_{conc} : H2O = 1:1
– Add diluted NH4OH to centrifuge tubes, ca. 0.3ml Ammonia to 1ml 1M HNO3 until pH ≈ 9
– Shake is NH4OH is added.
– Centrifuge
– Decant supernate
– Redissolve in 10ml 1M HNO3
– Repeat precipitation
– Centrifuge
– Decant supernate
– Wash precipitate in water
– Centrifuge
– Decant supernate

Silver solution: 38g AgNO3 into 1l ultrapure H2O
Or 157 mg AgNO3 into 10ml 5M HNO_3
– Add 0.3ml Ag solution
   (Aim: Ag:Be=20:1 => 4.7mg AgNO3 for 0.15mg Carrier)
– Transfer to quartz crucible
– Dry samples beneath red light or on hotplate in ceramic holder ca. 150°C
– Oxidize in oven or Bunsen burner (15sec drying sample outside of flame; 1 minute in blue part of flame to oxidize). Oxidize each sample separately. Use Pt-coated tongs.
– Use metal spatulum to scratch loose sample

(Al-Oxide)
– Dry down sample in Savillex beaker

- Add 2ml aq. regia and evaporate to dryness
  (ΔHNO_3: $\Delta HCl = 1$:1)
- Repeat once
- Add 1ml 14M ΔHNO_3 and 1ml H_2O_2 and evaporate to dryness
- repeat 2 times
- Add Silver Nitrate addition and Oxidize as with Be

6. Target

Work with dust mask or in fume hood!

- Clean targets 1min in 1M ΔHCl, rinse with H_2O, dry under red lamp
- Clean all instruments with ethanol
- Scratch out sample with spatula
- Load sample from rear in cleaned target with spatula, use cleaned steel plate coated with Al foil
- Hammer often but slightly (press down target)
- Add sample or copper Cu: p.a., 2703, 63um to fill hole from rear
- Label target on the front face with sample number

The original separation scheme was developed by von Blanckenburg et al. (1996) and modified by von Blanckenburg et al. (2004), with additional help from: Mirjam Schaller, Veerle Vanacker, Hella Wittmann, Kevin Norton, Jérôme Chmeleff; and suggestions by Darryl Granger.

A2. Chemical weathering rates: theory and methods

While cosmogenic nuclides provide us with an estimate of basin-averaged denudation rates, they do not provide any insight into the means by which the material is removed. It is possible that in a given setting, denudation is dominated by either chemical or physical weathering processes. Chemical weathering includes all processes by which individual species in a parent material are removed by dissolution, hydration, or cation exchange processes. In the granitic rocks of the Aar Massif, this will primarily take the form of biotite hydration and cation exchange in feldspars (White et al., 2001). Physical weathering then becomes the removal of solid particles, i.e. erosion. Using these definitions, total denudation can be written as

$$D = W + E \qquad\qquad\qquad A15$$

where D is denudation, W is chemical weathering and E is erosion. In order to separate the cosmogenic nuclide-derived denudation rate into its chemical and physical components, one of the two variables, W or E, needs to be solved for. This is possible using a mass-balance approach to determining chemical weathering rates (Riebe et al., 2001; Chadwick et al., 1990).

When deciding on a method for determining chemical weathering rates, the question of scale becomes important. The main tool of this study is cosmogenic [10]Be in stream and hillslope sediments. In landscapes that are eroding at typical Alpine rates (100 to 2000 mm ky[-1], (Wittmann et al., 2007; Norton et al., 2008, this work), the averaging timescale is on the order of 100's to 1000's of years. This means that any meaningful measure of chemical weathering must integrate over similar timescales. The simplest method for estimating chemical weathering rates is to measure the chemical composition of water, in the form of stream or groundwater samples, from the basin of interest. These methods by definition integrate over the residence time of water in the weathering system, typically less than a decade (White, 2003). Solute chemistry approaches have been shown to correlate well with long-term weathering rates in some cases (Pavich, 1986; White et al., 1998), but certainly not all: (Kirkwood and Nesbitt, 1991; Cleaves, 1993). Another possibility for determining chemical weathering rates is to measure the solid state reactants and products of weathering. In this case, the modern weathering rate can not be independently determined because the

current concentrations of reactants and products in the parent and soil material are the result of the integrated effect of weathering over the lifetime of the soil. In the glaciated terrains of the Central Alps, it can be assumed that much of the landscape below the equilibrium line altitude of the glaciers was sufficiently scoured to remove loose weathered debris. Solid state measurements of chemical weathering in these settings will average over the soil residence time, in the Goms, between ~ 6 and 12 ky, the approximate time of glacial retreat from the high Alpine valleys. Therefore, only these mass loss techniques will be discussed in the following sections.

A2.1. CHEMICAL WEATHERING PROXIES

The most commonly used solid state weathering proxies are chemical weathering indices, I_w. The indices considered here take the form;

$$I_w = \frac{\sum_0^n C_{i,w}}{\sum_0^n C_{j,w}}$$
A16

in which the sum of immobile elements, $C_{i,w}$, verses the sum of mobile elements, $C_{j,w}$, provide an estimate of the total degree of weathering in a system. Mobile elements are usually the alkali and alkali-earth cations; Na, K, Ca, Mg, Si, Fe(II), while the most common immobile element is Al. Of the numerous indices which have been proposed, few are well-suited to characterizing weathering in granitic rocks (White, 2003). Among the most reliable for granites and associated rocks (White, 2003; Burke et al., 2007) are the chemical index of alteration, CIA (Nesbitt and Young, 1982),

$$CIA = \frac{Al_2O_3}{Al_2O_3 + CaO + Na_2O + K_2O} \times 100$$
A17

and the chemical index of weathering, CIW (Harrois and Moore, 1988),

$$CIW = \frac{Al_2O_3}{Al_2O_3 + CaO + Na_2O} \times 100$$
A18

In both cases, values less than 50 represent fresh material, and values approaching 100 represent weathered material. These two indices are quite similar, with the exception that the CIA includes potassium as an immobile element. In the case of illite formation, $KAlSi_3O_{10}(OH)_2$, potassium is held in the soil, and the CIA will underestimate the degree of weathering. Elemental oxide concentrations are easily measured using X-ray fluorescence. Among the drawbacks of this method is that only relative weathering degrees can be estimated. In order to acquire an absolute sense of weathering, a full mass-balance study of the soil must be made. Mass-balance equations have been used to determine rates of chemical weathering (Brimhall and Dietrich, 1987; Chadwick et al., 1990; Riebe et al., 2001). All approaches are based on the same principle. The mass of a soil is the result of the addition of mass from a parent material less the loss of mass due to weathering, or

$$M_w = M_p - M_{weathering} \qquad \text{A19}$$

where M_w is soil mass per unit volume, M_p is rock mass per unit volume, and $M_{weathering}$ is mass loss to chemical weathering per unit volume. This equation can be solved for chemical weathering of any element, x;

$$C_{x,w}M_w = C_{x,p}M_p - M_{x,weathering} \qquad \text{A20}$$

where C is the concentration of the element, x, in weathered regolith, w, and parent material, p, respectively. It is important to note that these equations require that no erosion or deposition of soil is taking place. If an immobile element, i, one which is not subject to chemical weathering such as zirconium, is considered, then the final term becomes 0, so that;

$$C_{i,w}M_{i,w} = C_{i,p}M_{i,p} \quad (where \ M_{i,weathering} = 0) \qquad \text{A21}$$

and

$$M_{i,p} = \left(\frac{C_{i,w}}{C_{i,p}} \right) M_{i,w} \qquad \text{A22}$$

where $C_{i,w}$ is the concentration of the immobile element (e.g. Zr) in the soil and $C_{i,p}$ is the concentration of the immobile element in the parent rock. If this is substituted into the equation A18, then;

$$M_{i,w} = \left(\frac{C_{i,w}}{C_{i,p}} \right) M_{i,w} - M_{x,weathering}$$

A23

or,

$$M_{weathering} = M_{i,w} \left(\frac{C_{i,w}}{C_{i,p}} - 1 \right)$$

A24

This approach calculates the chemical weathering loss in a non-eroding landscape.

A2.2. CHEMICAL DEPLETION FRACTION

The above analysis is valid only for non-eroding landscapes. There are however few such landscapes in a mountainous region. Even landforms that are typically defined as non-eroding, moraines and terraces, usually have some component of erosion. Luckily, the same type of approach may be used in eroding landscapes by using equation A15 as a starting point, the amount of chemical weathering for any given element, x is;

$$W_x = C_{x,p} D - C_{x,w} E_w$$

A25

Where the chemical weathering rate for an element, W_x, is equal to the total loss of x to denudation, $C_{x,p}D$ minus the amount lost through soil erosion, $C_{x,w}E_w$. Again, if X is an immobile element such as Zr then;

$$E_{i,w} = \left(\frac{C_{i,p}}{C_{i,w}} \right) D \quad \left(where\ W_i = 0 \right)$$

A26

This can be substituted back into the original equation A24 so that:

$$W = D\left(1 - \frac{C_{i,p}}{C_{i,w}}\right) \qquad\qquad \text{A27}$$

Now the chemical weathering rate can be defined based on the denudation rate and the ratio of immobile element concentrations in the parent material and soil. Denudation rates are readily calculated using cosmogenic nuclides, and furthermore, the timescales over which cosmogenic rates averages is similar to that of soil formation and hillslopes erosion, 100's to 10,000's of years. Zirconium concentrations can be measured in soil and bedrock samples using XRF or ICP-MS techniques. The last term in Equation A27 has been defined as the Chemical Depletion Fraction, CDF, by (Riebe et al., 2003) so that

$$CDF = 1 - \frac{C_{i,p}}{C_{i,w}} \qquad\qquad \text{A28}$$

The CDF is the proportion of the total denudation rate that is due to chemical weathering.

A few important caveats exist for this method. The method relies on the measurement of Zr in bedrock and in soil. These are not reliable in every environment. If bedrock is inhomogeneous, large variations in the Zr concentration of the parent material may mask the weathering signal. This will be especially sensitive where soils move down-slope (Yoo et al., 2007) and mix (where a given soil mass may be derived from multiple parents. It is however, theoretically possible to create a mixing law for multiple sources if the contribution of each could be quantified using a different proxy, such as other trace elements.

Also important is the assumption of immobility. In some situations (i.e. extreme weathering) Zr can become mobile. This could lead to an underestimation in the chemical weathering rate. It is unlikely that chemical weathering has been strong enough in the relatively young landscape of the Central Alps in order to chemically weather zircon. A possible check on this is to use other immobile elements to calculate CDFs and compare the results. An assortment of immobile elements has been proposed for use in soil mass-balance calculations. The most widely used of these are Ti, Y, Nb, and Ce (Granger and Riebe, 2007). Titanium however has been repeatedly shown to be mobile under many conditions, and Zr proves to be the most conservative element in these settings. A third possible

perturbation to Zirconium concentrations is through Aeolian input. Again, this can be either an addition or dilution of [Zr] depending on the Zr concentration in the dust. It has been suggested that in all but the most long-lived soils, Aeolian input is negligible (Granger and Riebe, 2007).

A2.3. FIELD AND LABORATORY METHODS

Chemical weathering rates were determined from major and trace element concentrations in soils and bedrock samples. Soils were collected using a semi-random sampling strategy. This method was chosen because of the many potential biases related to soil sampling. Heimsath et al. (1999, 2005) have shown that soil thicknesses and hillslopes gradient play a major role in determining soil production rates, and (Green et al., 2006; Burke et al., 2007) have shown that similar relationships exist for soil chemical proxies. In order to reduce this potential bias, sample locations were chosen on a variety of hillslope types (convex noses, linear hillslopes, concave hollows, etc.) with varying soil thicknesses, 5 to >40 cm. Based on soil core data, soil thickness on some linear slopes in the Goms exceeds 1m.

Samples of 0.2-0.5kg were taken from the main soil body. Effort was taken to avoid the uppermost organic rich layer as well as saprolites. The soil was chosen because saprolites can have different chemical weathering rates than the overlying soils (Green et al., 2006), and the surface organic layer is more prone to downslope transport. Samples were therefore taken from depths ranging from 5 to 40 cm depending on soil thickness and structure. All soils in the Goms showed at most weak zonation, suggesting that soils were well mixed. This is important for two reasons. Green et al. (2006) showed that CDFs can vary with depth in situations where well stratified soils exist. In a subsequent study by Burke et al, well-mixed soils were shown to have little to no depth dependence on CDFs. Furthermore, ^{10}Be concentrations in the absence of a mixed layer decrease rapidly with depth, where as they remain constant, and represent the surface concentration, within a mixed layer. By sampling well-mixed soils, the CDFs and denudation rates should be representative of the soil column as a whole.

Soils were dried for 24 hours at 100ºC and then sieved to <1cm. The coarsest fraction of soil samples is often removed (April et al.,1986; Bain et al.,1993). We chose a more

conservative approach, 1 cm vs. 0.2 to 0.5 cm in other studies. This was done because of the large number of weathered bedrock fragments found throughout the entire soil column. This suggests that rock weathering continues in the soil column (Granger and Riebe, 2007) and the removal of the 0.2 to 1 cm size fraction could introduce a bias in the CDFs to lower rates than exist. A representative 50g sample was obtained using a Jones splitter. This 50g sub-sample was then powdered in a swing mill for XRF analysis.

The remaining soils were then pooled by geomorphic region (ridge tops, glacial valleys, fluvial hillslopes, and interfluvial surfaces) by mass. These pooled soil samples were then treated as stream sediments samples to purify quartz.

We collected loose bedrock samples when possible, from corestones in the soil or from rockfall deposits. In this way, we obtained fresh random unweathered bedrock samples. A further possible complication is the deep weathering of plagioclase in granitic rocks. (White et al., 2001) noted that in Georgia, plagioclase could be altered in as deep as 6 m in apparently unweathered bedrock. This could pose a problem for the Zr method, if such a sample is used as the parent rock. While this weathering is isovolumetric, it is not iso-mass, meaning that zirconium concentrations of bedrock could be incorrect. An indicator for weathered bedrock is the chemical index of alteration, CIA. In the case of the granites and gneisses of the Aar Massif, CIA values of the granites and gneisses average 65. This value, while higher than one would expect for unweathered bedrock, is not unreasonable for unweathered material (Burke et al., 2007). Furthermore, thin sections of the granites and gneisses show no evidence of plagioclase alteration, further supporting the notion that the bedrock samples do represent unweathered parent material.

Samples were cleaned in the field to remove any surface weathering rinds or moss, and to reduce the size to 0.2-0.5kg. In the lab, the samples were sequentially crushed to smaller sizes in jaw crushers and then a representative sample, acquired by Jones splitter, was powdered in a swing mill for XRF analysis.

Sample powders were prepared for XRF analysis at the Budesanstalt für Geowissenschaften und Rohstoffe, BGR Geochemistry section. 1 gram of the powdered, < 40 μm, material was heated to 1030°C for 10 minutes to drive off volatile compounds such as water and carbon dioxide. The remaining material was mixed with 5 g of lithium metaborate and 25 mg of lithium bromide and melted into a pellet in platinum crucibles at 1200°C for 20 minutes. Quantitative analysis of 10 primary and 31 trace elements was made using an Itrax EDXRF-microscope with precision ranging from <0.1%.

Table A3. Major and select trace element analysis of Goms soils.

Sample	SiO2	TiO2	Al2O3	Fe2O3	MnO	MgO	CaO	Na2O	K2O	P2O5	(SO3)	(Cl)	(F)	LOI	Sum_RF
	%	%	%	%	%	%	%	%	%	%	%	%	%	%	%
O-R 1	59.39	0.606	14.25	5.01	0.032	0.77	1.555	2.82	2.508	0.19	0.07	0.004	<0.05	12.29	99.53
O-R 2	61.16	0.564	15.68	4.95	0.049	1.27	1.669	3.58	2.622	0.195	0.02	0.003	0.09	7.62	99.48
O-R 3	62.91	0.631	15.07	4.63	0.109	0.9	1.691	2.85	2.977	0.133	<0.01	<0.002	<0.05	7.53	99.48
O-R 4	63.55	0.471	14.66	3.58	0.023	0.73	1.275	3.22	3.094	0.124	0.01	0.003	0.08	8.7	99.53
O-R 5	63.83	0.512	14.51	3.72	0.036	1.17	1.192	3.01	3.224	0.117	0.05	0.007	<0.05	8.17	99.53
O-R 6	60.5	0.418	14.13	4.52	0.032	0.94	1.319	3.21	2.597	0.191	0.05	<0.002	0.06	11.62	99.58
O-R 7	64.98	0.404	14.6	3.21	0.036	0.86	1.084	3.55	3.069	0.122	0.05	0.003	0.09	7.55	99.6
O-R 8	64.75	0.315	14.72	2.13	0.022	0.66	1.466	3.95	2.561	0.143	0.05	0.003	<0.05	8.75	99.57
O-Rg 1	72.8	0.147	12.12	1.62	0.027	0.53	0.193	3.91	3.512	0.05	0.06	0.005	<0.05	4.75	99.73
O-Rg 2	70.08	0.155	12.12	1.6	0.023	0.42	0.23	3.49	3.727	0.096	0.05	0.009	<0.05	7.7	99.71
O-Rg 3	72.99	0.17	11.49	1.46	0.025	0.32	0.263	3.07	3.714	0.079	0.05	0.003	<0.05	6.07	99.75
O-Rg 4	71.44	0.216	12.72	1.63	0.03	0.3	0.412	3.27	3.99	0.06	0.05	0.003	<0.05	5.56	99.68
O-Vg 1	62.03	0.291	12.07	1.25	0.022	0.49	0.459	2.5	3.271	0.203	0.06	<0.002	<0.05	16.99	99.66
O-Vg 2	70.92	0.184	12.29	1.96	0.035	0.24	0.424	3.32	3.676	0.07	0.05	0.002	<0.05	6.48	99.66
O-Vg 3	71.61	0.2	12.31	1.49	0.104	0.28	0.411	3.2	3.973	0.056	0.05	<0.002	<0.05	6.01	99.7
O-Vg 4	64.55	0.228	11.08	0.77	0.02	0.27	0.358	2.83	3.213	0.088	0.06	0.006	<0.05	16.21	99.69
O-Vg 5	48.25	0.144	9.47	1.23	0.064	0.28	0.565	2.55	2.799	0.147	0.04	<0.002	<0.05	34.19	99.73
O-V 1	65.54	0.333	14.23	2.12	0.031	0.81	1.493	4.09	2.441	0.128	0.07	0.005	<0.05	8.22	99.55
O-V 2	64.68	0.457	15.27	2.99	0.047	0.92	1.625	3.9	3.163	0.192	0.07	0.005	<0.05	6.12	99.45
O-V 3	66.63	0.435	15.06	2.64	0.06	0.77	1.811	3.96	3.122	0.16	0.05	0.006	0.07	4.73	99.5
O-V 4	67.92	0.298	14.99	1.81	0.025	0.7	1.759	3.92	2.545	0.046	0.04	0.003	0.09	5.37	99.52
O-V 5	55.31	0.578	14.42	4.21	0.089	1.5	2.174	3.12	2.575	0.264	0.07	0.006	0.1	15.09	99.5
O-V 6	66.11	0.498	14.14	3.19	0.045	1.37	1.244	3.72	2.621	0.092	0.08	0.003	<0.05	6.49	99.66
O-I 1	63.63	0.446	14.25	3.46	0.034	0.86	1.299	3.26	2.658	0.202	0.08	0.005	<0.05	9.36	99.55
O-I 2	60.53	0.512	14.63	3.77	0.095	1.43	2.04	3.27	2.623	0.616	<0.01	0.014	<0.05	9.95	99.52
O-I 3	63.17	0.487	14.17	3.18	0.143	0.78	1.538	3.24	2.82	0.151	<0.01	0.036	<0.05	9.82	99.57
O-I 4	64.16	0.492	14.92	3.31	0.047	0.81	1.307	3.32	2.951	0.166	<0.01	0.035	<0.05	8.01	99.55
O-I 5	63.12	0.467	14.91	3.42	0.048	0.94	1.29	3.36	2.954	0.168	<0.01	0.034	<0.05	8.89	99.61
O-I 6	65.77	0.508	15.01	3.27	0.073	0.99	1.844	3.31	3.246	0.171	<0.01	0.022	0.15	5.24	99.61
O-I 7	66.12	0.451	15.15	2.93	0.058	1.32	1.761	3.66	3.211	0.227	<0.01	0.026	<0.05	4.64	99.59
O-I 8	67	0.354	14.43	2.4	0.044	0.71	1.112	3.69	3.181	0.114	<0.01	0.021	<0.05	6.59	99.64
O-I 9	65.52	0.406	14.74	2.87	0.076	0.87	1.026	3.4	3.329	0.092	<0.01	0.018	<0.05	7.22	99.6
O-I 10	62.39	0.461	15	3.26	0.074	1.21	1.462	3.73	2.679	0.145	<0.01	0.036	0.14	9.03	99.61
O-I 11	63.08	0.441	14.75	3.06	0.046	1.01	1.568	3.57	2.785	0.153	<0.01	0.038	0.05	9.03	99.58
O-I 12	67.95	0.37	14.61	2.26	0.05	0.66	1.323	3.91	2.754	0.08	<0.01	0.043	<0.05	5.57	99.58
N-Vg 1	72.24	0.17	12.72	1.67	0.045	0.26	0.459	3.2	4.368	0.058	<0.01	0.047	0.07	4.45	99.75
N-Vg 2	73.81	0.135	12.59	1.34	0.049	0.19	0.539	3.43	4.346	0.04	<0.01	0.039	0.07	3.17	99.73
N-Vg 3	71.24	0.204	12.5	1.84	0.058	0.29	0.484	3.06	4.01	0.073	<0.01	0.045	<0.05	5.91	99.7
N-Vg 4	73.45	0.141	11.28	1.08	0.054	0.17	0.404	2.86	4.033	0.047	<0.01	0.048	<0.05	6.13	99.7
N-Vg 5	73.45	0.146	12.05	1.35	0.021	0.28	0.288	3.31	3.856	0.048	<0.01	0.049	0.1	4.85	99.8
N-V 1	61.25	0.43	14.75	3.11	0.046	1.28	2.027	3.75	2.578	0.176	<0.01	0.037	<0.05	10.07	99.52
N-V 2	60.95	0.496	15.09	3.64	0.068	1.55	1.981	3.61	2.607	0.247	<0.01	0.043	<0.05	9.25	99.56
N-V 3	59.81	0.591	15.27	4.27	0.07	1.95	1.886	3.44	2.757	0.281	<0.01	0.042	0.06	9.09	99.51
N-V 5	65.67	0.389	14.14	2.5	0.033	0.75	1.582	3.77	2.671	0.126	<0.01	0.042	<0.05	7.92	99.58
H-V 1	62.07	0.456	15.56	3.52	0.06	1.59	2.367	4.04	2.722	0.285	<0.01	0.045	0.05	6.74	99.52
H-V 2	61.93	0.469	14.42	3.03	0.044	0.88	1.631	3.54	2.838	0.134	<0.01	0.02	<0.05	10.58	99.54
H-V 3	60.7	0.367	14.15	2.91	0.053	1.25	1.523	3.91	2.257	0.116	<0.01	0.02	0.1	12.24	99.6
H-V 4	65.06	0.339	15.78	2.99	0.042	1.17	1.493	4.44	2.863	0.115	<0.01	0.029	<0.05	5.19	99.52
H-V 5	60.11	0.712	15.47	5.9	0.084	1.8	1.595	2.84	2.906	0.141	<0.01	0.027	0.06	7.94	99.59
H-V 6	61.42	0.477	14.5	3.31	0.058	0.98	1.593	3.52	2.445	0.166	<0.01	0.05	0.07	11.03	99.61
H-R 1	63.38	0.351	14.95	2.43	0.03	0.78	1.698	4.16	2.27	0.132	<0.01	0.048	<0.05	9.32	99.57
H-R 2	62.15	0.418	14.71	3.66	0.028	1.16	1.115	3.29	3.204	0.152	<0.01	0.044	0.05	9.59	99.56
H-R 3	65.94	0.358	15.31	2.48	0.022	0.54	1.359	4.09	2.658	0.096	<0.01	0.045	0.05	6.59	99.53
H-R 4	60.09	0.461	14.41	2.92	0.024	0.58	1.605	3.38	2.217	0.187	<0.01	0.03	<0.05	13.62	99.55
H-R 5	59.49	0.574	14.59	3.62	0.071	1.17	1.592	2.65	2.654	0.138	<0.01	0.027	0.1	12.97	99.63
H-R 6	63.66	0.418	14.52	2.4	0.034	0.65	1.246	3.68	2.245	0.146	<0.01	0.028	<0.05	10.55	99.61
H-I 1	66.87	0.418	13.95	2.83	0.071	0.87	1.453	3.63	2.621	0.158	<0.01	0.031	<0.05	6.68	99.63

Sample	SiO2	TiO2	Al2O3	Fe2O3	MnO	MgO	CaO	Na2O	K2O	P2O5	(SO3)	(Cl)	(F)	LOI	Sum_RF
	%	%	%	%	%	%	%	%	%	%	%	%	%	%	%
H-I 2	67.24	0.345	14.74	2.57	0.081	0.72	1.347	4.06	3.008	0.1	<0.01	0.038	0.08	5.28	99.61
H-I 3	69.15	0.374	14.26	2.57	0.05	0.65	1.143	3.88	3.04	0.068	<0.01	0.05	0.07	4.33	99.64
H-I 4	59.48	0.563	13.94	3.91	0.107	1.17	1.394	2.62	2.566	0.111	<0.01	0.017	0.11	13.62	99.6
H-I 5	66.3	0.376	15.28	2.56	0.065	0.8	1.314	4.08	2.81	0.073	<0.01	0.037	<0.05	5.9	99.56
W-R 1	67.78	0.382	14.08	2.79	0.031	1.29	1.458	3.33	2.537	0.163	<0.01	0.038	<0.05	5.66	99.54
W-R 2	65.98	0.389	15.58	2.5	0.045	0.84	1.99	4.56	2.286	0.122	<0.01	0.038	0.05	5.16	99.53
W-R 3	64.01	0.418	16.33	2.97	0.063	1.12	1.823	4.86	2.089	0.143	<0.01	0.023	<0.05	5.7	99.5
W-R 4	66.39	0.283	14.81	2.16	0.027	0.81	1.347	4.38	2.616	0.089	<0.01	0.042	0.06	6.6	99.61
W-R 5	65.33	0.322	14.38	2.33	0.023	0.94	0.555	3.78	3.018	0.123	<0.01	0.045	0.06	8.71	99.62
W-R 6	62.64	0.444	13.84	3.24	0.089	0.9	1.634	3.91	2.574	0.13	<0.01	0.033	<0.05	10.13	99.57
W-V 1	63.03	0.581	16.48	4.24	0.069	1.96	0.995	3.65	3.706	0.252	<0.01	0.038	0.17	4.51	99.68
W-V 2	66.09	0.435	15.13	3.05	0.061	1.39	1.209	3.59	3.445	0.175	<0.01	0.038	0.09	4.88	99.58
W-V 3	62.78	0.468	13.73	1.9	0.024	0.88	0.651	2.95	3.223	0.248	<0.01	0.039	<0.05	12.74	99.64
W-V 4	67.16	0.4	14.35	3.39	0.042	1.51	0.722	3.33	3.369	0.087	<0.01	0.039	<0.05	5.2	99.56
W-V 5	67.48	0.487	14.91	2.64	0.037	0.7	1.308	3.49	3.234	0.08	<0.01	0.017	<0.05	5.14	99.56
W-V 6	68.43	0.281	15.07	2.09	0.039	0.86	1.705	4.31	3.197	0.13	<0.01	0.045	<0.05	3.41	99.57
W-V 7	64.31	0.346	14.48	2.6	0.042	1.1	1.809	3.96	2.598	0.131	<0.01	0.044	0.08	8.09	99.58
W-V 8	61.18	0.39	12.75	2.72	0.041	1.22	1.849	3.25	2.232	0.221	<0.01	0.047	<0.05	13.64	99.57
W-V 9	65.89	0.414	14.52	2.94	0.051	1.09	1.686	3.78	2.55	0.096	<0.01	0.045	<0.05	6.44	99.51
W-V 10	61.01	0.61	15.99	4.63	0.071	1.6	2.27	3.53	2.851	0.161	<0.01	0.045	<0.05	6.66	99.46
M-R1	62.51	0.336	14.2	2.23	0.039	1.11	1.378	3.54	2.576	0.289	<0.01	0.009	<0.05	11.44	99.67
M-R2	68.77	0.373	14.06	2.3	0.027	0.88	1.514	3.28	2.436	0.131	<0.01	0.006	<0.05	5.87	99.63
M-R3	60.35	0.65	14.48	4.04	0.055	1.93	2.71	2.68	2.624	0.172	<0.01	0.008	<0.05	9.91	99.64
M-R4	62.17	0.452	15.29	3.09	0.043	1.15	2.061	3.45	2.882	0.2	<0.01	0.005	<0.05	8.86	99.67
M-R5	61.67	0.454	14.26	4.2	0.043	1.49	1.63	3.04	2.354	0.238	<0.01	0.006	<0.05	10.26	99.66
M-R6	72.71	0.278	12.4	1.49	0.039	0.36	0.57	2.66	4.145	0.088	<0.01	0.009	<0.05	5	99.78
M-R7	73.55	0.211	12.07	1.25	0.025	0.27	0.459	2.84	4.096	0.07	<0.01	0.014	<0.05	4.93	99.84
M-R8	69.75	0.224	11.43	1.86	0.028	0.37	0.4	2.7	3.786	0.149	<0.01	0.014	<0.05	9.04	99.77
M-V1	59.97	0.403	13.52	2.41	0.04	0.79	1.348	2.95	2.613	0.191	<0.01	0.006	<0.05	15.42	99.7
M-V2	60.98	0.529	14.2	3.78	0.081	1.23	1.814	3.01	2.418	0.244	0.01	0.006	<0.05	11.32	99.62
M-V3	62.55	0.41	13.68	2.97	0.07	0.88	1.239	3.16	2.552	0.128	<0.01	0.005	<0.05	12.06	99.67
M-V4	70.18	0.296	15.03	2.3	0.041	0.83	1.135	4.07	3.599	0.103	0.01	0.007	<0.05	2.1	99.68
M-V5	61.89	0.354	13.03	2.57	0.035	0.73	1.128	2.94	2.806	0.149	<0.01	0.005	<0.05	14.07	99.7
M-V6	72.04	0.243	14.21	1.69	0.033	0.63	1.393	4.14	3.239	0.112	<0.01	0.007	<0.05	1.93	99.68
B-R1	62.11	0.408	16.15	2.68	0.054	0.73	2.478	3.88	2.266	0.127	<0.01	0.011	<0.05	8.7	99.63
B-R2	68.14	0.477	15.11	2.5	0.063	0.64	1.709	3.3	2.584	0.091	<0.01	0.018	<0.05	4.99	99.62
B-R3	63.43	0.429	14.92	3.12	0.05	0.77	1.869	3.71	2.068	0.147	0.01	0.019	<0.05	9.05	99.63
B-R4	61.96	0.44	15.32	3.44	0.045	1.02	2.117	3.79	1.911	0.178	0.01	0.005	0.07	9.36	99.66
B-R5	61.72	0.541	14.66	3.37	0.098	0.83	1.667	2.94	2.393	0.215	<0.01	0.007	<0.05	11.17	99.59
B-V1	67.55	0.334	15.37	2.4	0.046	0.77	1.628	4.04	2.771	0.128	<0.01	0.004	<0.05	4.61	99.66
B-V2	59.61	0.515	15.07	3.88	0.053	1.27	1.892	3.71	2.194	0.153	<0.01	0.004	<0.05	11.27	99.62
B-V3	60.6	0.518	14.94	3.5	0.088	1.58	1.875	3.09	3.029	0.222	<0.01	0.005	<0.05	10.12	99.62
B-V4	67.58	0.325	15.33	2.2	0.079	0.7	1.688	4.03	3.048	0.14	<0.01	0.006	0.05	4.5	99.68
B-F1	55.55	0.743	15.15	5	0.092	1.63	2.584	3.03	2.095	0.363	0.01	0.028	<0.05	13.27	99.56
B-F2	58.28	0.646	15.15	4.73	0.067	1.71	1.948	3.21	2.476	0.213	0.01	0.005	<0.05	11.14	99.6
B-F3	60.61	0.475	14.86	3.9	0.057	1.55	1.995	3.38	2.405	0.176	<0.01	0.005	<0.05	10.25	99.66
B-F4	54.08	0.919	16.08	6.38	0.123	2.5	3.118	2.8	2.23	0.375	0.02	0.004	<0.05	10.9	99.55
B-F5	54.09	0.929	16.19	6.3	0.123	2.49	3.111	2.86	2.241	0.368	0.02	0.006	<0.05	10.81	99.54
OG 1	75.49	0.126	13.05	1.24	0.027	0.25	0.154	3.86	4.831	0.035	0.01	0.021	0.05	0.64	99.72
OG 2	74.87	0.123	13.37	1.2	0.048	0.31	0.294	3.79	4.832	0.035	0.01	0.02	0.05	0.76	99.69
OG 3	73.82	0.161	13.66	1.53	0.062	0.21	1.08	4.05	4.451	0.046	0.01	0.047	0.13	0.53	99.76
MG1	78.06	0.121	11.69	1.24	0.04	0.31	0.533	3.21	4.021	0.031	<0.01	0.006	<0.05	0.54	99.81
NG 1	74.32	0.137	13.58	1.3	0.054	0.17	1.014	3.95	4.406	0.037	0.01	0.043	0.06	0.62	99.68
OK 1	69.31	0.278	16.12	1.7	0.032	0.81	2.5	4.87	2.848	0.139	0.01	0.046	0.07	0.8	99.51
OK 2	68.73	0.287	16.15	1.94	0.035	0.87	2.468	4.9	2.788	0.146	0.01	0.044	0.09	1.04	99.48
NK 1	68.84	0.301	16.07	1.96	0.041	1.4	1.161	5.4	2.974	0.124	0.01	0.041	0.09	1.18	99.57
WK 1	68.95	0.298	16.58	1.98	0.032	0.78	2.896	5.18	2.463	0.14	0.01	0.024	0.11	0.1	99.52
MK1	69.54	0.28	16.22	1.67	0.033	1	1.9	4.43	3.166	0.124	<0.01	0.007	<0.05	1.12	99.51

Sample	Ba mg/kg	Ce mg/kg	Cr mg/kg	Ga mg/kg	La mg/kg	Nb mg/kg	Pb mg/kg	Rb mg/kg	Sc mg/kg	Sr mg/kg	Th mg/kg	U mg/kg	V mg/kg	Y mg/kg	Zn mg/kg	Zr mg/kg
O-R 1	985	73	30	26	49	15	38	93	8	538	29	<3	76	6	34	195
O-R 2	1133	87	21	22	67	14	37	99	9	594	36	7	69	10	70	214
O-R 3	1331	94	34	26	63	16	32	112	10	641	25	3	73	17	43	231
O-R 4	1154	81	18	24	55	13	29	95	6	485	25	4	55	6	32	187
O-R 5	941	72	29	24	39	15	32	112	8	421	30	7	39	11	47	176
O-R 6	914	79	18	21	55	13	27	90	7	480	33	6	40	7	33	179
O-R 7	1114	84	13	23	43	13	31	108	7	443	25	5	46	10	27	184
O-R 8	1059	56	14	20	21	10	19	84	3	525	25	<3	29	9	20	128
O-Rg 1	449	43	10	16	34	15	11	124	3	55	18	4	8	17	22	92
O-Rg 2	382	56	10	16	39	15	19	148	3	71	26	4	11	18	24	107
O-Rg 3	413	22	<3	16	38	13	18	155	3	74	24	<3	16	15	22	105
O-Rg 4	490	48	12	19	31	15	22	148	4	92	24	4	15	18	19	167
O-Vg 1	448	76	17	18	35	19	36	146	5	95	27	10	25	20	25	133
O-Vg 2	462	86	10	19	31	17	30	140	4	88	29	5	12	21	16	132
O-Vg 3	511	62	13	17	<20	13	24	163	4	100	15	3	17	20	24	147
O-Vg 4	434	<20	16	16	22	14	30	127	4	88	14	<3	26	5	28	135
O-Vg 5	375	41	4	13	<20	13	41	119	3	89	18	19	21	20	30	81
O-V 1	1066	61	11	20	<20	7	26	85	5	566	24	<3	42	<3	35	138
O-V 2	1376	107	14	22	63	17	36	109	5	605	34	6	52	9	47	235
O-V 3	1285	121	18	22	79	15	28	101	6	608	36	21	41	7	44	231
O-V 4	1123	45	12	22	38	7	18	84	3	791	22	3	42	<3	29	153
O-V 5	1057	120	44	24	74	20	57	130	10	644	36	5	69	12	79	210
O-V 6	486	47	34	22	29	10	23	128	10	296	26	7	59	13	45	148
O-I 1	813	86	25	24	55	13	30	109	7	445	26	5	54	10	42	214
O-I 2	947	92	23	21	42	14	30	114	8	567	29	5	54	12	92	215
O-I 3	904	89	26	23	61	13	41	136	8	488	31	<3	62	15	48	215
O-I 4	841	57	31	25	38	13	35	144	8	429	23	<3	55	8	48	196
O-I 5	883	77	21	22	21	12	37	132	7	431	31	3	46	12	52	188
O-I 6	922	101	29	22	50	16	36	146	10	523	28	4	61	16	54	213
O-I 7	973	59	34	24	33	12	45	143	8	546	26	6	39	11	73	181
O-I 8	822	98	44	20	40	9	37	136	5	377	28	3	31	11	48	152
O-I 9	855	72	28	22	41	10	40	156	7	356	25	<3	51	16	62	157
O-I 10	1094	51	23	25	35	8	33	123	7	541	25	<3	61	9	78	164
O-I 11	998	89	18	21	32	12	30	116	7	520	24	5	43	10	53	177
O-I 12	958	76	18	20	34	10	28	112	7	487	25	<3	38	7	45	184
N-Vg 1	466	72	5	16	30	17	53	162	4	77	31	8	12	22	23	148
N-Vg 2	462	24	8	16	52	15	21	165	4	79	35	11	<5	24	19	159
N-Vg 3	468	63	14	16	43	13	31	157	6	88	22	4	22	18	20	138
N-Vg 4	426	54	13	16	32	8	20	152	3	69	20	<3	15	13	21	118
N-Vg 5	399	65	<3	14	39	13	15	135	3	66	29	6	7	22	14	122
N-V 1	1102	55	17	22	27	11	29	100	7	601	27	4	46	9	52	149
N-V 2	1052	63	22	22	54	12	34	101	8	584	25	4	56	11	63	154
N-V 3	1282	96	25	21	54	15	32	104	10	651	27	3	69	14	63	218
N-V 5	941	84	17	19	60	11	22	111	5	536	25	6	37	9	35	170
H-V 1	1274	85	17	20	<20	11	32	91	9	743	24	<3	57	12	52	160
H-V 2	1093	83	15	19	48	12	32	101	8	588	27	<3	51	4	39	205
H-V 3	900	48	27	19	<20	8	29	88	7	543	18	5	46	6	54	118
H-V 4	1177	33	26	22	<20	6	37	97	5	592	20	4	48	8	62	118
H-V 5	1022	61	67	22	35	13	39	136	12	457	27	8	105	13	80	184
H-V 6	959	55	29	24	33	10	31	129	8	518	28	<3	67	13	47	183
H-R 1	1093	28	16	22	21	6	23	88	5	693	13	5	38	4	37	134
H-R 2	1346	45	44	22	20	10	22	133	7	576	18	5	44	9	31	152
H-R 3	1335	35	21	21	32	6	24	100	5	672	21	8	41	4	24	156
H-R 4	1093	49	26	23	32	11	29	80	7	549	24	<3	64	6	23	170
H-R 5	883	45	79	24	<20	10	34	126	12	429	23	5	82	12	40	198
H-R 6	906	47	23	22	<20	8	30	84	5	490	17	3	50	5	29	158
H-I 1	787	77	27	18	49	12	24	118	8	449	25	3	58	13	58	196

Sample	Ba mg/kg	Ce mg/kg	Cr mg/kg	Ga mg/kg	La mg/kg	Nb mg/kg	Pb mg/kg	Rb mg/kg	Sc mg/kg	Sr mg/kg	Th mg/kg	U mg/kg	V mg/kg	Y mg/kg	Zn mg/kg	Zr mg/kg
H-I 2	842	92	24	19	43	8	32	112	7	453	25	3	44	15	45	161
H-I 3	718	90	27	18	40	10	44	119	7	344	18	3	39	16	58	182
H-I 4	695	79	53	19	38	14	53	129	10	346	24	<3	72	17	97	210
H-I 5	1055	71	23	22	46	6	33	119	7	463	24	3	50	9	49	159
W-R 1	1094	46	33	20	20	8	18	97	7	506	25	5	38	7	36	142
W-R 2	1158	54	20	19	28	7	32	85	6	698	25	5	41	3	39	155
W-R 3	919	60	24	23	43	6	24	94	5	688	23	<3	46	7	46	150
W-R 4	988	51	12	20	<20	6	21	93	5	589	18	<3	19	<3	24	123
W-R 5	1201	40	12	19	25	8	19	95	4	315	20	<3	41	<3	30	134
W-R 6	856	107	23	19	67	13	35	123	7	417	25	8	44	16	63	227
W-V 1	1136	63	13	21	22	8	24	144	8	313	25	<3	71	13	63	158
W-V 2	1031	42	45	20	32	8	33	135	7	456	29	3	38	14	51	165
W-V 3	818	55	27	21	36	14	40	132	7	256	23	5	52	9	30	177
W-V 4	972	72	57	22	34	15	38	112	7	331	25	<3	39	9	40	188
W-V 5	984	77	14	22	64	10	43	123	7	564	27	3	59	9	27	241
W-V 6	1070	64	9	21	27	8	32	116	4	592	28	3	19	6	46	130
W-V 7	987	27	42	19	28	6	33	99	8	546	23	23	41	6	42	124
W-V 8	754	105	49	19	42	10	37	88	8	494	28	110	45	16	122	178
W-V 9	889	93	40	19	29	13	39	97	8	499	28	31	50	8	56	172
W-V 10	1315	91	31	22	70	16	34	122	11	744	30	5	94	12	79	201
M-R1	1001	73	15	20	32	10	33	165	5	528	21	<3	36	9	67	138
M-R2	951	59	14	21	27	8	33	117	5	555	18	3	40	10	35	172
M-R3	888	64	69	23	26	15	33	97	13	483	20	4	89	17	50	178
M-R4	1002	85	12	21	37	15	27	103	7	548	30	6	45	20	43	197
M-R5	894	108	20	19	47	15	40	81	8	450	27	5	46	20	58	177
M-R6	520	55	13	18	20	15	27	219	5	123	18	4	30	21	28	151
M-R7	472	41	5	16	<14	17	24	202	5	105	17	3	29	18	22	141
M-R8	812	67	8	17	30	22	24	191	5	103	24	4	20	18	25	144
M-V1	1019	42	16	22	30	13	35	126	7	446	16	<3	46	10	37	172
M-V2	930	75	36	19	43	15	41	113	9	542	26	5	64	23	60	216
M-V3	911	57	21	21	35	15	39	113	7	440	21	5	48	17	51	184
M-V4	981	64	13	17	32	10	55	117	5	336	18	4	37	18	65	135
M-V5	915	59	18	19	42	9	29	121	7	386	22	5	40	14	43	178
M-V6	840	87	6	16	36	10	24	111	5	393	25	3	24	19	29	174
B-R1	1085	97	16	23	43	7	32	85	7	784	27	<3	48	7	33	209
B-R2	1314	53	25	22	38	10	32	112	7	594	17	3	59	13	30	206
B-R3	1163	67	12	22	50	8	26	71	7	769	20	<3	46	8	35	160
B-R4	1067	57	21	23	35	10	26	62	6	753	16	<3	49	10	49	148
B-R5	1213	59	29	22	39	12	42	106	8	611	16	<3	69	10	48	185
B-V1	1055	62	12	20	36	10	29	99	5	566	18	<3	37	17	43	163
B-V2	979	69	31	22	38	10	31	94	10	581	18	<3	71	18	51	195
B-V3	1249	70	45	22	26	12	40	125	8	553	20	<3	58	15	61	192
B-V4	1119	72	14	19	45	10	29	120	7	518	21	3	39	15	38	166
B-F1	976	114	34	22	45	18	38	108	13	715	26	4	98	22	81	245
B-F2	1011	72	38	21	37	15	42	122	12	543	25	5	94	17	72	218
B-F3	870	56	38	21	35	14	32	105	10	479	22	<3	63	19	61	161
B-F4	961	94	39	25	60	19	46	132	16	793	24	<3	124	26	108	267
B-F5	969	105	42	25	66	20	46	131	15	788	25	4	127	25	105	255
OG 1	422	61	5	16	20	16	42	184	3	49	40	4	16	24	24	100
OG 2	485	37	4	18	29	14	19	188	3	74	32	4	7	28	26	93
OG 3	539	45	6	16	27	17	26	205	4	92	35	8	5	30	35	107
MG1	332	70	<4	14	42	20	23	187	3	79	33	6	<6	31	20	107
NG 1	516	46	3	16	35	17	32	184	3	92	35	8	5	29	27	96
OK 1	1214	36	7	23	36	10	32	98	3	797	24	3	17	7	25	109
OK 2	1194	20	4	22	21	9	33	117	5	933	11	3	29	4	47	112
NK 1	1373	29	8	19	56	5	29	118	4	554	24	3	21	7	62	107
WK 1	1049	27	10	23	20	8	29	92	5	864	19	3	28	5	37	124
MK1	1730	58	5	20	27	12	27	90	3	757	14	<3	25	5	45	107

Appendix 3. GIS methods

GIS has become an indispensable tool for geomorphic researchers. Many of the analyses that are now commonplace; slope, aspect, basin analysis, were time prohibitive as recently as two decades ago. The proliferation of computer cartographic programs and data sources has lead directly to many great improvements in our understanding of surface processes. All GIS analyses in this work were performed with ArcMap version 9.1 using a combination of standard tools and self-designed equations. The following two sections describe the data sources and analyses used.

A3.1. DATA SOURCES

Along with [10]Be derived denudation rates, this work relied heavily on GIS analysis for data visualization, storage, and morphometrics. The dataset used for large spatial areas (Rhone, Alps) was the Shuttle Radar Topography Mission (SRTM) 30m elevation dataset, void filled by Jonathan de Ferranti (Fife, UK). For the Napf study, Cantons Bern and Luzern provided a LiDAR dataset which was processed and interpolated to 2 meter resolution by Marco Schwab (Universität Berne). Additional topographic datasets include the 1:25K SwissTopo maps, scanned and georeferenced in house. These maps provide much more accurate stream gradient measurements than most digital elevation models, and avoid the problem of artificial steps in the stream profile that are common when using SRTM data. National boundaries, cities, and major waterways were obtained from the Digital Chart of the World. The monthly snow depth data were digitized from Auer's original data (2003), creating digital monthly snow depth rasters. Swiss rock uplift data were provided as XYZ files by Dr. Andreas Schlatter, Schweizer Bundesamt für Landestopographie (Schlatter et al., 2005) and interpolated to produce uplift surfaces. Additional datasets, specific to individual studies are described in those sections.

A.3.2. MORPHOMETRIC PARAMETERS

Basic geomorphic parameters were calculated for all sampled catchments. In particular, slope was calculated in degrees with ArcMap's Slope command (Burrough and McDonnell, 1988)
where;

$$rise/run = \sqrt{\left(\frac{dz}{dx}\right)^2 + \left(\frac{dz}{dy}\right)^2} \quad and,$$

$$Slope° = \arctan(rise/run) \times 57.29578$$

A29

Hillslope relief can be defined as the difference between the maximum and minimum elevations within a given area. Unless otherwise noted, relief was calculated using a 250x250 meter sliding window. This size was chosen as it is large enough to capture entire hillsides, but small enough to be able to recognize differences between basins. Watersheds, the total contributing area for a stream, were delineated using ArcMap Hydrology tools with the Flowdirection and Watershed commands. Flow direction calculates the direction which water will flow on a given hillslope by determining the direction of steepest decent using the equation;

$$drop = \frac{dz}{distance} \times 100$$

A30

where distance is the distance between the center of the cells in question (Greenlee,1987; Jenson and Domingue, 1988). Watershed then determines all the cells that flow into the pour point (sampling location for cosmogenic nuclides in this case). So, all watersheds are specifically defined as the contributing areas for the basin-averaged denudation rates. The hypsometric integrals for these basins were calculated as;

$$HI = \frac{(z_{mean} - z_{min})}{(z_{max} - z_{min})}$$

A31

and hypsometric curves generated by plotting the normalized distribution of elevations against the normalized area. In most cases, slope-area diagrams were created in order to calculate stream curvatures and steepness indices. These were generated by plotting the stream gradient, dx/dy, as measured from either the DEM or topographic maps against the upstream basin area for each point. In all cases, the data were smoothed using running averages of 40 to 200 meters depending on data density. Methodology for specific morphometrics parameters, such as the stream proximal slope and curvature measurements are described in the individual sections.

Ciriculum Vitae

Kevin Patrick Norton
Hirtenstraße 9a
D-30952 Hannover
k.norton@mineralogie.uni-hannover.de

13 March, 1974 – Born in Springfield, Ohio, USA

1980 – 1983 – New Morefield Elementary School, Springfield, OH
1983 – 1986 – Rolling Hills Elementary School, Springfield, OH
1986 – 1988 – Northridge Middle School, Springfield, OH
1988 – 1992 – Kenton Ridge High School, Springfield, OH

1992-1994 – Luther College, Decorah, Iowa

1994-1997 – The Ohio State University, Columbus, Ohio
1997 – Bachelor of Science Degree, Chemistry
1997 – Bachelor of Science Degree, Geology

1998 - 2000 – University of Minnesota-Duluth, Duluth, Minnesota
2000 – Master of Science Degree, Geology

2001 – 2004 – Lecturer in Geoscience, Penn State University-Erie, The Behrend College,
              Erie, PA
2003 – 2004 – Adjunct Faculty in Geology, Geology Department, Mercyhurst College,
              Erie, PA

2005 – Doctoral Studies, Institute for Mineralogy, University of Hannover

List of Publications

Norton, K.P., and Vanacker, V., in press. Effects of terrain smoothing on topographic shielding correction factors for cosmogenic nuclide-derived estimates of basin-averaged denudation, *Earth Surface Processes and Landforms*. doi: 10.1002/esp.1700.

Norton, K.P., von Blanckenburg, F., Schlunegger, F., Schwab, M., and Kubik, P.W., 2008. Cosmogenic nuclide-based investigation of spatial erosion and hillslope channel coupling in the transient foreland of the Swiss Alps, *Geomorphology*. **95**, 474-486. doi:10.1016/j.geomorph.2007.07.013

Norton, K.P. and Lanier, A.J., 2007. Subglacial landforms of the Erie uplands, Northwest Pennsylvania – Implications for early Wisconsinan glacial chronology of the Erie Lobe of the Laurentide ice sheet, *Journal of the Pennsylvania Academy of Science* **81,** 81-85.

Norton, K.P., in press. The effects of isostatic rebound and lake level on Lake Superior revealed through GIS: visualizing landscape evolution, in "*State of Lake Superior*", M. Muniwar and R. Heath Eds., *Ecovision World Monograph Series*, in press.

Wittmann, H. ,von Blanckenburg, F., Kruesmann, T., Norton, K.P. and Kubik. P.K. 2007. The relation between rock uplift and denudation from cosmogenic nuclides in river sediment in the Central Alps of Switzerland. *Journal of Geophysical Research A: Earth Surface* **112**, F04010.

Foyle, A. M. and Norton, K. P., 2007. Geo-feasibility of in-situ capping in a Great Lakes urban estuary: a sediment budget assessment, *Environmental Geology* **53**, 271-282.

Foyle, A. M. and Norton, K. P., 2006. Sediment loading during the 20th century in Presque Isle Bay, Lake Erie, Pennsylvania, *Journal of Great Lakes Research* **32**, 697-711.

Foyle, A. M. and Norton, K. P., 2006. Late Holocene nearshore change at a nontidal transgressive systems tract strandplain complex, Presque Isle, Pennsylvania, USA, *Journal of Coastal Research,* **22**, 406-423.